FACULTAD DE FÍSICA
Departamento de Física Atómica, Molecular y Nuclear

DEVELOPMENT OF A LOW P_T MUON LVL2 TRIGGER ALGORITHM WITH THE ATLAS TILECAL DETECTOR

Research Report
Trabajo de Investigación

ARÁNZAZU RUIZ MARTÍNEZ
Arantxa.Ruiz@ific.uv.es

CERN-THESIS-2009-130
15/09/2006

Directores:
Emilio Higón Rodríguez
Juan Antonio Valls Ferrer

September 15th 2006

D. EMILIO HIGÓN RODRÍGUEZ, Catedrático de la Universitat de València y miembro del Departamento de Física Atómica, Molecular y Nuclear de la Facultad de Física de la Universitat de València y del Instituto de Física Corpuscular (IFIC) de Valencia

CERTIFICA:

Que la presente memoria **Development of a Low p_{T} Muon LVL2 Trigger Algorithm with the ATLAS TileCal Detector** ha sido realizada bajo mi dirección y la del Dr. JUAN ANTONIO VALLS FERRER en el Instituto de Física Corpuscular (Centro mixto CSIC-UV) por Dña. ARÁNZAZU RUIZ MARTÍNEZ y constituye su trabajo de investigación para optar al Diploma de Estudios Avanzados (DEA).

Y para que conste, en cumplimiento de la legislación vigente, firmamos el presente Certificado en Burjassot a 15 de Septiembre de 2006.

Dr. Emilio Higón Rodríguez

Dr. Juan Antonio Valls Ferrer

Contents

List of Figures

List of Tables

Introduction

In November 2007, one of the largest and most complex sets of scientific instruments ever constructed - the Large Hadron Collider (LHC) and its four companion experiments (ATLAS, CMS, Alice and LHCb) - is scheduled to begin its odyssey into the uncharted waters beyond the Standard Model of particle physics. The discoveries that are likely to be made there could fundamentally change our ideas about the basic constituents of matter, and therefore our concepts of the universe itself. It is this hope that has led the 20 member states of CERN, and a number of non-member state partners as well, to promote, develop, fund and build the LHC project. In addition, several thousand physicists have bet a substantial part of their careers on the success of the LHC.

As a part of this global effort, the TileCal-Valencia group has collaborated in the Hadronic Tile Calorimeter of the ATLAS experiment, being responsible of the following tasks:

- Construction, assembly and quality control of half extended barrel modules as a contribution to the mechanics.
- Characterization of 1750 photomultipliers as a contribution to the optics.
- Design and assembly of the Read Out Drivers (RODs) and Transition Modules as a contribution to the back-end electronics.

The first two tasks have been completed successfully in the past few years. This research report is framed in the final part of the project before ATLAS operation starts in 2007. It is devoted to the study and implementation of a low p_{T} muon tagging algorithm which makes use of the energy deposition in the hadronic calorimeter. As the ATLAS muon spectrometer can only trigger muons with $p_{\mathrm{T}} > 6$ GeV, TileCal can help triggering lower p_{T} muons with this algorithm. For instance, the ATLAS di-muon trigger efficiency in B-physics channels will be enhanced with the TileCal information provided by this algorithm. Furthermore, its implementation in the TileCal ROD will not introduce extra dead time at LVL2 as all the processing has been done previously at the ROD level.

This report has been structured in six chapters:

Chapter 1 gives a short review of the Standard Model and the most promising theories for the physics beyond. An overview of the Standard Model physics programme at ATLAS is also given in this chapter, with special interest in Higgs boson searches and B-physics.

Chapter 2 makes a brief overview of the CERN laboratory at Geneva, its history and its next major project: the LHC accelerator and its experiments. Details are given for one of those experiments: ATLAS, with special interest in its Hadronic Tile Calorimeter (TileCal). As a part of the TileCal electronics the Read-Out Driver (ROD) and its DSPs are described. In a few words, this chapter contains a small description the framework where this work has been developed and the detector in which is being used.

Chapter 3 describes the different methods used in TileCal to reconstruct the energy deposition in the calorimeter from the electronic readout signals and discusses the fundaments of the low p_{T} muon tagging algorithm (MTag) based on the energy obtained in the calorimeter cells. The implementation of this algorithm in the ROD DSP core and its output in the general ROD data format is also described in this chapter.

Chapter 4 is dedicated to the results from the analysis of the MTag algorithm offline performance using different samples of Monte Carlo data for single muons and B-physics processes: the inclusive process $\mathrm{b\overline{b}} \rightarrow \mu(6)\mathrm{X}$ with one muon of $p_{\mathrm{T}} > 6$ GeV in the final state and the decay $\mathrm{B_s^0} \rightarrow \mathrm{J}/\psi(\mu\mu)\phi$ with one muon with p_{T} of at least 6 GeV and one muon with p_{T} of at least 3 GeV in the final state. For instance, the last channel studied is used to make Standard Model precision tests and *CP* violation studies. Results are obtained in terms of efficiency and fake rates.

Chapter 5 is devoted to the results from the analysis of the MTag algorithm online performance using the first real data (cosmic muons) taken with TileCal during the commissioning period. Results on the DSP processing time measurements are also presented in this chapter.

Chapter 6 presents the software developments done in the Athena framework (used for ATLAS offline computing) to decode and use the information provided by the MTag algorithm. In addition, a brief review on the LVL2 muon trigger and the algorithms used there is given and the future implementation of the MTag algorithm at LVL2 is discussed.

Chapter 1

Physics Motivations

1.1 High Energy Physics Overview

1.1.1 Standard Model Review

The Standard Model (SM) [1] is a very successful description of the interactions of the components of matter at the smallest scales ($<10^{-18}$ m) and highest energies ($\sim$200 GeV) available. It is a quantum field theory which describes the interaction of spin-1/2, point-like fermions, whose interactions are mediated by spin-1 gauge bosons. The bosons arise when local gauge invariance is applied to the fermion fields, and are a manifestation of the symmetry group of the theory, which for the Standard Model is SU(3)$\times$SU(2)$\times$U(1). The fundamental fermions are leptons and quarks. There are three generations of fermions, each identical except for mass. The origin of this generational structure, and the breaking of generational symmetry (i.e. the different masses of each generation) remains a mystery. Corresponding to the three generations, there are three leptons with electric charge -1, the electron (e), the muon (μ) and the tau (τ), and three electrically neutral leptons (the neutrinos $\nu_{\rm e}$, ν_μ and ν_τ). Similarly there are three quarks with electric charge +2/3, up (u), charm (c) and top (t), and three with electric charge -1/3, down (d), strange (s) and bottom (b). There is mixing between the three generations of quarks, which in the SM is parametrized (but not explained) by the Cabibbo-Kobayashi-Maskawa (CKM) matrix.

The quarks are triplets of the SU(3) gauge group and so they carry an additional "charge", referred to as color, which is responsible for their participating in the strong interaction (quantum chromodynamics or QCD). Eight vector gluons mediate this interaction; they carry color charges themselves, and are thus self-interacting. This implies that the QCD coupling $\alpha_{\rm s}$ is small for large momentum transfers but large for soft processes, and leads to the confinement of quarks inside color-neutral hadrons (like protons and neutrons). Attempting to free a quark produces a jet of hadrons through quark-antiquark pair production and gluon bremsstrahlung.

In the SM, the SU(2)$\times$U(1) symmetry group, which describes the so-called Electroweak Interaction, is spontaneously broken through the existence of a (postulated) Higgs field with non-zero expectation value. This leads to the emergence of massive vector bosons, the $W^{\pm}$ and the Z, which mediate the weak interaction, while the photon of electromagnetism remains massless. One physical degree of freedom remains in the Higgs sector, which could be manifest most simply as a neutral scalar boson H^0, which is presently unobserved. Figure 1.1 shows graphically all the particles in the SM.

The basics of the SM were proposed in the 1960's and 1970's. Increasing experimental evidence of the

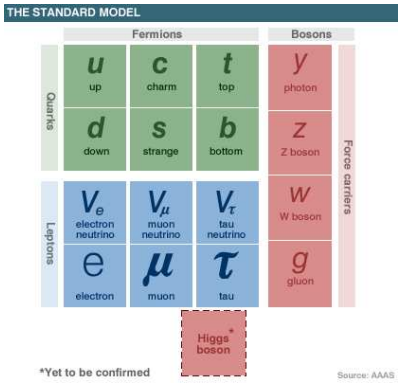

Figure 1.1: Standard Model elementary particles.

correctness of the model accumulated through the 1970's and 1980's. Deep inelastic scattering experiments at SLAC showed the existence of point-like scattering centers inside nucleons, later identified with quarks. The c and b quarks were observed and neutral weak currents (Z exchange) were identified. Three-jet final states (from gluon bremsstrahlung) were observed in e^+e^- and hadron-hadron collisions, and the W and Z were directly observed at the CERN SPS collider. Following these discoveries, the 1990's decade was largely an era of consolidation. Even more precise experiments were carried out at LEP and SLC which provided verification of the couplings of quarks and leptons at the level of 1-loop radiative corrections - $O(10^{-3})$. The top quark was discovered at FNAL in 1995, and it was found to have an unexpectedly large mass (175 GeV). After the discovery in 2000 of the ν_τ in the DONUT experiment also at FNAL, only one particle of the SM has yet to be observed: the Higgs boson. The last, but the most important as it holds the key to the generation of W, Z, quark and lepton masses.

1.1.2 Beyond the Standard Model

The successes of the Standard Model have drawn increased attention to its limitations. In its simplest version, the SM has 19 parameters - three coupling constants, nine quark and lepton masses, the mass of the Z boson which sets the scale of the weak interaction, four CKM mixing parameters, and one (small) parameter describing the scale of *CP* violation in the strong interaction. The remaining parameter is associated with the mechanism responsible for the breakdown of the electroweak $SU(2)\times U(1)$ symmetry to U(1) of electromagnetism ("electroweak symmetry breaking" or EWSB). This can be taken as the mass of the Higgs boson the couplings of the Higgs are determined once its mass is given. Within the model we have no guidance on the expected mass of the Higgs boson. The current experimental lower bound from LEP2 is about 115 GeV, and the upper limit from global fits to electroweak parameters is about 470 GeV. As its mass increases, the self-couplings of the W and Z grow, and so the mass must be less than about 800 GeV, or the strong dynamics of WW and ZZ interactions will reveal new structure. It is this simple argument that sets the energy scale that must be reached to guarantee that an experiment will be able to provide information on the nature of electroweak symmetry breaking, which is the central goal of the Large Hadron Collider.

The presence of a single elementary scalar boson is distasteful to many theorists. If the theory is part of some more fundamental theory with a larger mass scale (such as the scale of grand unification, or the Planck scale) then radiative corrections will result in the Higgs mass being driven up to this large scale unless some delicate cancellations are engineered. There are two ways out of this problem which both result in new physics on the scale of 1 TeV. New strong dynamics could enter that provide the scale of the W mass or new particles could appear which would cancel the divergences in the Higgs boson mass. In any of these eventualities - Standard

Model, new dynamics or new particles - something must be discovered at the TeV scale, i.e. at the LHC.

Supersymmetry is an appealing concept for which there is at present no experimental evidence. It offers the only presently known mechanism for incorporating gravity into the quantum theory of particle interactions and provides an elegant cancellation mechanism for the divergences affecting the Higgs mass, while retaining all the successful predictions of the Standard Model and allowing a unification of the three couplings of the gauge interactions at a high scale. Supersymmetric models postulate the existence of superpartners for all the presently observed particles. There are bosonic superpartners of fermions (squarks and sleptons), and fermionic superpartners of bosons (gluinos and gauginos χ_i^0, $\chi_i^{\pm}$). There are also multiple Higgs bosons: h, H, A and $H^{\pm}$. There is thus a large spectrum of presently unobserved particles, whose exact masses, couplings and decay chains are calculable in the theory given certain parameters. Unfortunately these parameters are unknown; but if supersymmetry has anything to do with EWSB, the masses should be in the region 100 GeV - 1 TeV.

An example of the strong coupling scenario is "technicolor" models based on dynamical symmetry breaking. An elegant implementation of these ideas is lacking. Nonetheless, if the dynamics has anything to do with EWSB, we would expect new states in the region 100 GeV - 1 TeV. Most models predict a large spectrum. At the very least, there must be structure in the WW scattering amplitude at around 1 TeV center-of-mass energy.

There are also other possibilities for new physics that are not necessarily related to the scale of EWSB. There could be neutral or charged gauge bosons with masses larger than the Z or W. There could be new quarks, charged leptons or massive neutrinos or quarks and leptons might turn out not to be elementary objects. While we have no definite expectations for the masses of such particles, the LHC must be able to search for them over its entire available energy range.

1.2 Standard Model Physics at LHC

1.2.1 Higgs Hunting

The Standard Model Higgs boson is searched for at the LHC[1] in a wide variety of decay channels, the choice of which is given by the signal rates and the signal-to-background ratios in the various mass regions. However, most of them suffer from their very small production rate and from very large QCD backgrounds. Excellent detector performance in terms of energy/momentum resolution and unprecedented particle-identification capabilities are required. The most promising channels for Higgs discovery at LHC are the following:

- $H \to \gamma\gamma$ either in direct production or from the associated production WH, ZH and ttH.
- $H \to b\overline{b}$ from the associated production WH, ZH and ttH.
- $H \to 4l$ (mediated by 2 virtual Z bosons)
- $H \to 2l2\nu$ (mediated by 2 virtual W bosons)
- $H \to ZZ \to 2l2\nu$
- $H \to WW \to l\nu 2j$

Figure 1.2 shows the estimated discovery potential for these channels in the ATLAS experiment for a Higgs mass range from 100 GeV to 1 TeV for an integrated luminosity of 100 pb^{-1}.

[1]The LHC accelerator and the ATLAS experiment are detaily described in Chapter 2.

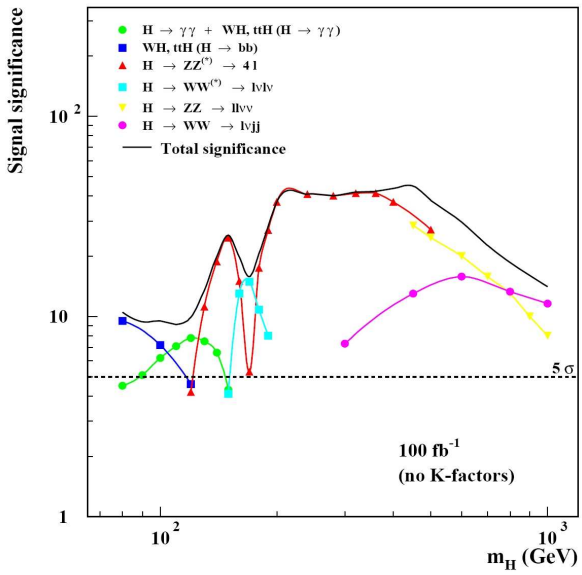

Figure 1.2: ATLAS sensitivity to the discovery of the SM Higgs boson for a 100 fb^{-1} integrated luminosity as a function of the Higgs mass for several decay channels.

1.2.2 Physics of Electroweak Gauge Bosons

Gauge bosons and gauge-boson pairs will be abundantly produced at the LHC. The large statistics and the high center-of-mass energy will allow several precision measurements to be performed, which should improve significantly the precision achieved at present machines, such as:

- **Measurement of the W mass:**

  The W mass, which is one of the fundamental parameters of the Standard Model, is related to other parameters of the theory and precise measurements of both the W mass and the top mass allow constraining the mass of the SM Higgs boson or of the h boson of the Minimal Supersymmetric Standard Model (MSSM).

- **Gauge-boson pair production:**

  The principle of gauge invariance is used as the basis for the SM. The non-Abelian gauge-group structure of the theory of Electroweak Interactions predicts very specific couplings between the Electroweak gauge bosons. Any theory predicting physics beyond the Standard Model, while maintaining the SM as a low-energy limit, may introduce deviations in the couplings. Measurements of these Triple Gauge-boson Couplings (TGC) and Quadruple Gauge-boson Couplings (QGC) of the W, Z and γ gauge-bosons will not only be a stringent test of the Standard Model and the electroweak symmetry breaking, but also probe for new physics in the bosonic sector.

1.2.3 B-physics

The rate of B-hadron production at the LHC is enormous thanks to the large hadronic cross-section for b-quark production and the high luminosity of the machine: about one collision in every hundred will produce a b-quark pair. In ATLAS, an inclusive-muon trigger with a p_{T} threshold of 6 GeV will make an initial selection of B-events. Using this inclusive selection, about 25% of the muon-trigger events will contain b-quarks. The B-event rate will be higher than in any accelerator in operation before the start-up of the LHC.

Although the main focus of the ATLAS physics programme is the search for and study of physics beyond the Standard Model, through the production and decay of new types of particles, an important range of B-physics studies is planned. In fact, an important aim of the B-physics work is to test the SM through precision measurements of B-hadron decays that together will over-constrain the CKM matrix, possibly giving indirect evidence for new physics.

- ***CP*-violation in B-meson decays:**

  Within the Standard Model, *CP* violation in weak decays is introduced by the phase of the CKM quark-mixing matrix. The unitarity of this matrix is used to derive triangle relation between the matrix elements, defining the so-called unitary triangle which has 3 angles denoted as α, β and γ. Figure 1.3 shows the updated constraints for the angles and sides of the CKM triangle with the currently available data (see [2] for details).

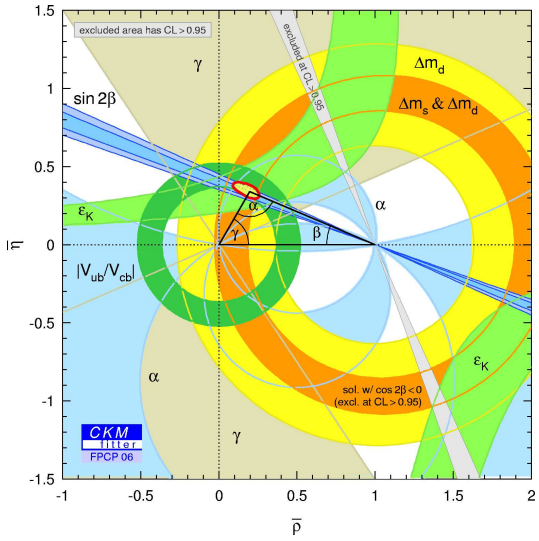

Figure 1.3: Current boundaries on the CKM unitary triangle. The red blob represents the constraints obtained with the world average data.

The most important channels to study *CP* violation in ATLAS are the following:

- $\mathrm{B_d^0} \to \mathrm{J}/\psi\,\mathrm{K_s^0}$, with $\mathrm{J}/\psi \to \mu\mu$ or $\mathrm{J}/\psi \to \mathrm{ee}$ and $\mathrm{K_s^0} \to \pi^+\pi^-$:

  This channel can provide a clean measurement of the angle β of the unitary matrix. The asymmetry in this channel depends only on the mass difference in the $\mathrm{B_d^0}$ - $\overline{\mathrm{B_d^0}}$ system (Δm_{d}) and the angle β, without any contribution from penguin diagrams. Furthermore, it is experimentally a very clean

channel with relatively low backgrounds.

– $B_s^0 \to J/\psi\,\phi$, with $J/\psi \to \mu\mu$ and $\phi \to KK$:

Only a very small asymmetry is predicted for this channel in the SM, but an observation of a sizeable effect would be a clear sign of new physics. In addition, some SM parameters can be measured in this channel, such as the width difference in the B_s^0 - $\overline{B_s^0}$ system.

– $B_d^0 \to D^0 K^{*0}$:

The study of the decay amplitude in this channel would be used to determine the angle γ of the unitary matrix.

Summing up, high-statistics studies of *CP* violation in these channels will give measurements of the unitary triangle angles and will search for deviations from the Standard Model.

- **Measurements of B_s^0 oscillations:**

The observed B_s^0 and $\overline{B_s^0}$ states are linear combinations of two mass eigenstates, denoted here as H and L. Due to the non-conservation of flavour in charged weak-current interactions, transitions between B_s^0 and $\overline{B_s^0}$ states occur with a frequency proportional to $\Delta m_s = m_H - m_L$. Experimentally, these oscillations have not yet been observed directly. In the B_d^0 - $\overline{B_d^0}$ system, the oscillations have been directly observed and precisely measured (the current value of this mass difference is Δm_d=(0.507 $\pm$ 0.004) ps^{-1}). Simulations show that it will be possible to measure Δm_s at LHC with a good sensitivity.

- **Rare B-decays:**

Certain decays, such as $B_{s,d} \to \mu\mu(X)$, involve Flavour-Changing Neutral Currents (FCNC) and are strongly suppressed in the Standard Model, with predicted branching ratios typically in the range 10^{-5} to 10^{-10}.

These decay modes are forbidden at the tree level in the SM, so the decays involve loop diagrams. In non-standard models of electroweak interactions, FCNC processes can be allowed at the tree level and thus, the branching ratios of these rare decays would not be so suppressed. In addition, in the presence of new physics, additional particles may be present in the loops again enhancing the decay probability. Due to the very low SM predictions for the branching fractions for purely muonic decays, a significant enhancement in measured branching fractions would clearly demonstrate the effects of new physics.

Chapter 2

The Experimental Apparatus

2.1 CERN

In 1949, to redress the balance and restore a strong European scientific community after the Second World War, the French physicist and Nobel prize-winner Louis de Broglie proposes the creation of a European science laboratory. Founded in 1954, the laboratory was one of Europe's first joint ventures by 12 states. It was provisionally named *Conseil Européen pour la Recherche Nucléaire* (European Council for the Nuclear Research, CERN) and sited astride the Franco-Swiss border near Geneva. The name has changed in two more occations to European Organization for Nuclear Research and the current European Laboratory for Particle Physics, but the acronym lasts until today. Nowadays CERN is the world's largest particle physics center.

Figure 2.1: CERN aerial view.

Currently, CERN includes 20 European Member States: Austria, Belgium, Bulgaria, the Czech Republic, Denmark, Finland, France, Germany, Greece, Hungary, Italy, The Netherlands, Norway, Poland, Portugal, the Slovak Republic, Spain, Sweden, Switzerland and the United Kingdom. However, many non-European countries are also involved in different ways. More than 6500 scientists (about half the world's particle physics community) collaborate in experiments conducted at CERN for their research. In particular, Spain joined CERN in November 1983 and more than 350 people are involved.

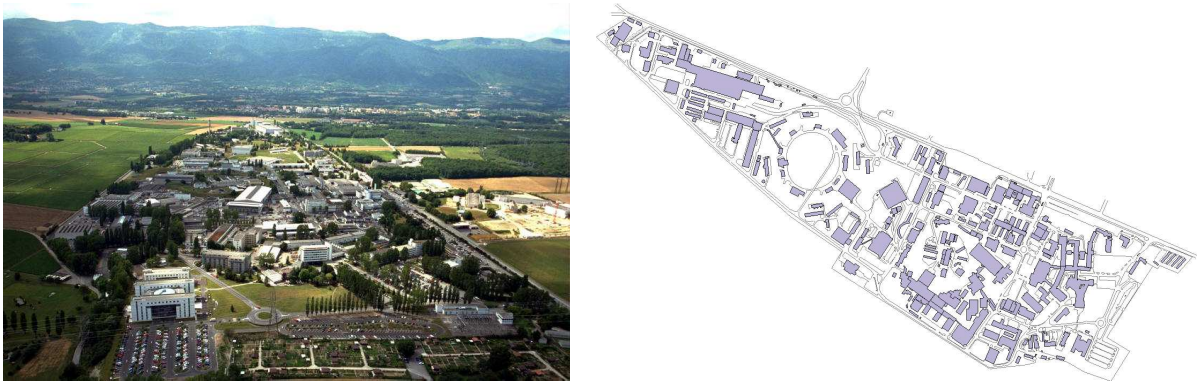

(a) Aerial picture of the CERN Meyrin site.

(b) Map of the CERN Meyrin site.

Figure 2.2: CERN Meyrin site.

Since its foundation, great discoveries have been possible at CERN. In 1968 the invention of multiwire proportional chambers and drift chambers revolutionized the domain of electronic particle detectors. In 1992, Georges Charpak of CERN was awarded the Nobel Prize for Physics for this work.

In 1976 the operation of the Super Proton Synchrotron (SPS) started. On 25 January 1983, a historic press conference announced the observation of W particles in the UA1 experiment at CERN, and was followed by another in May when Z particles were found. The proton-antiproton collisions in the SPS led confirmed the unification of weak and electromagnetic forces as predicted by theory in 1968. In recognition of these efforts, Carlo Rubbia, head of the UA1 project, and Simon van der Meer, inventor of the stochastic cooling technique, were awarded the Nobel Prize for Physics, 1984. It was the first Nobel Prize awarded for research conducted at CERN.

At the beginning of the 1980's, CERN embarked on the enormous Large Electron-Positron Collider (LEP) construction project. The excavation of the 27-kilometer LEP tunnel was a huge technical challenge. LEP had 5176 magnets, 128 accelerating cavities (to re-accelerate the energy lost in the bends of the ring) and 4 enormous detectors: ALEPH, DELPHI, L3 and OPAL. The first collisions took place in August 1989 and only two months after, extremely accurate measurements of the Z particle showed that the fundamental building blocks of matter consist of three, and only three, families of particles. LEP operated at 100 GeV for seven years and produced Z particles. In 1995, LEP was upgraded for a second phase of operation known as LEP2, and spent the rest of its career operating at almost twice its original energy (over 200 GeV). This led to the production of W^+ and W^- pairs, the other two vectors of the weak force. After 11 years of successful research, the LEP was closed down on 2 November 2000 to make way for the construction of the LHC (see Section 2.2), which will continue to challenge the Standard Model.

In addition, the LHC injectors have their own experimental hall, where their beams are used for experiments at lower energies. A scheme of the CERN accelerators is shown in Figure 2.3. Some of these experimental facilities are truly unique:

- **ISOLDE:** On-Line Isotope Mass Separator, produces radioactive nuclei for a number of aplications covering nuclear, atomic, molecular and solid state physics, but also biology and astrophysics.
- **NTOF:** Neutron Time-Of-Flight, produces neutrons in an energy range covering more than eight orders of magnitude (between 1 eV and ∼250 MeV) for experiments in nuclear physics. The time of arrival of

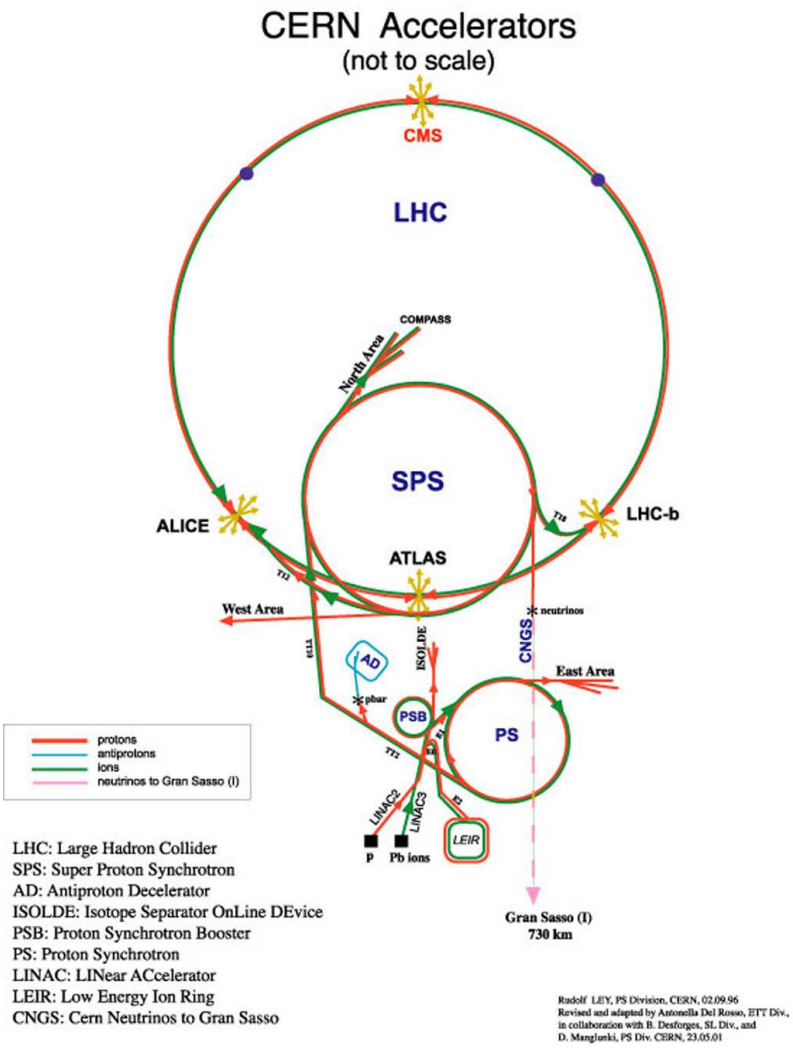

Figure 2.3: CERN accelerator complex.

the particle at the experiment is a measure of the energy.

- **AD:** the Antiproton Decelerator, is an antimatter factory. Its aim is to produce antihydrogen atoms for the particle physicists to study their spectroscopy and test fundamental symmetries.
- **CNGS:** CERN Neutrino beam to Gran Sasso, sends a high intensity neutrino beam to a detector located near Rome, 800 km away from CERN.

Apart from pure scientific discoveries, great technological developments have been done at CERN. For instance, the World Wide Web (WWW) was proposed by CERN as a distributed information system based on 'hypertext'. Nowadays, the GRID project is developing an architecture for large scale computing based on the use of many computers connected by a network.

As CERN is a pioneer institution, innovative technologies developed at CERN find many applications in different fields. Cancer therapy, medical and industrial imaging, radiation processing, electronics, measuring instruments are some examples.

2.2 The Large Hadron Collider (LHC)

The next research instrument in Europe's particle physics armoury is the Large Hadron Collider (LHC) [3], currently under construction. In keeping CERN's cost-effective strategy of building on previous investments, it is designed to share the 100-meter underground and 27-kilometer LEP tunnel, and be fed by existing particle sources and pre-accelerators. For instance the SPS accelerator was first upgraded into a proton-antiproton collider, then a heavy ion accelerator, later a lepton injector for LEP and now a high density proton injector for LHC.

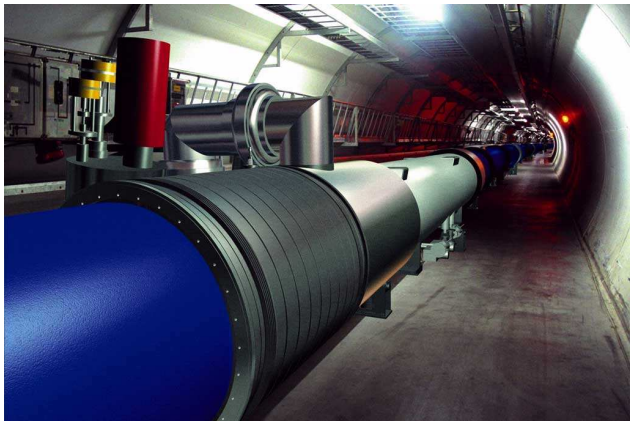

Figure 2.4: Simulation of the LHC in the tunnel.

The two proton beams will collide with a center-of-mass energy of 14 TeV and beams of heavy ions such as lead with a total collision energy in excess of 1250 TeV. The resulting large beam current (I_b = 0.53 A) is a particular challenge in a machine made of delicate superconducting magnets operating at cryogenic temperatures. To bend 7 TeV protons around the ring, the LHC dipoles must be able to produce fields of 8.36 T, almost 10^5 times the earth's magnetic field. LHC magnet coils are made of copper-clad niobium-titanium cables and will be operated at 1.9 K. Figures 2.4 and 2.5 show the LHC magnets in the tunnel and their different parts respectively.

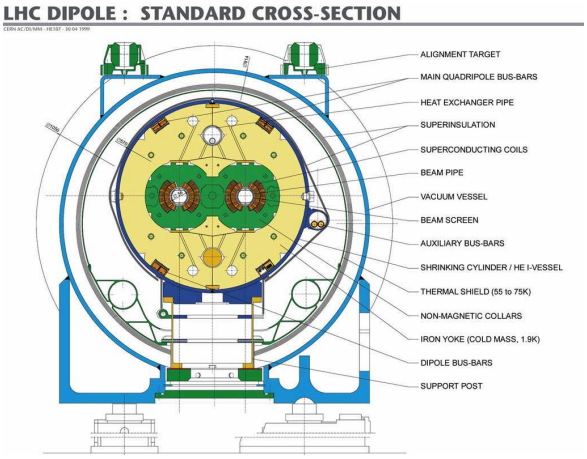

Figure 2.5: LHC dipole magnet diagram.

The proton beams will contain 2835 bunches separated 7.5 millimeters of 10^{11} particles each, achieving a luminosity of 10^{34} cm^{-2}s^{-1}. It will work at 40 MHz rate, that is, bunch crossings will be produced each 25 ns. Table 2.1 summarizes the LHC main parameters and Figure 2.6 shows the placement of the LHC underground structures.

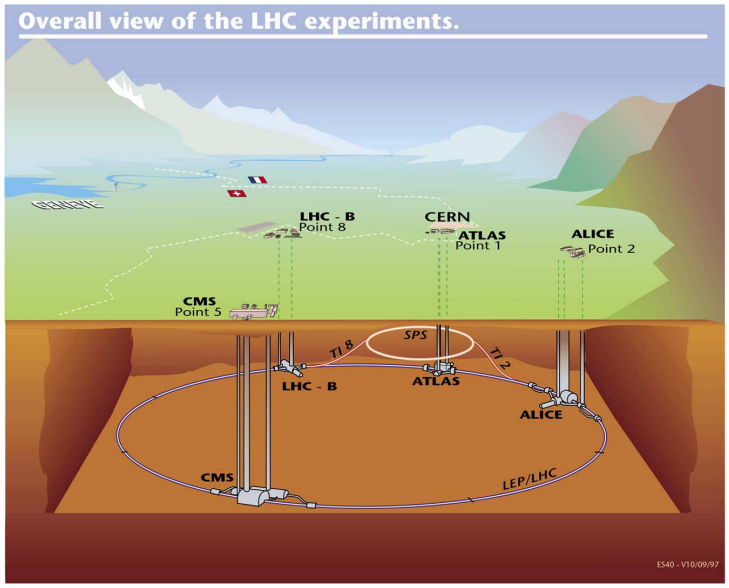

Figure 2.6: LHC schematic layout.

Table 2.1: LHC beam parameters for proton and lead ion collisions.

	p $\longleftrightarrow$ p	**Pb $\longleftrightarrow$ Pb**
Energy at injection	450 GeV	1.774 TeV/u
Energy at collision	7 TeV	2.76 TeV/u
Center-of-mass energy	14 TeV	1250 TeV
Luminosity	10^{34} cm^{-2}s^{-1}	10^{31} cm^{-2}s^{-1}
Number of particles per bunch	1.15×10^{11}	7×10^{7}
Number of bunches	2808	592
Bunch separation	25 ns	100 ns
Number of collision points	4	
Number of insertions	8	
Ring Circumference	26658.883 m	
Number of main belds	1232	
Length of main belds	14.3 m	
Field of main belds at injection	0.535 T	
Field of main belds at collision	8.33 T	

2.3 The LHC experiments

The LHC experiments have been designed to look for theoretically predicted phenomena. However, they must also be prepared, as far as is possible, for surprises. Four experiments, with huge detectors are involved in the LHC (see Figure 2.7):

ATLAS (A Toroidal LHC ApparatuS) is one of the two LHC general-purpose experiments. The detector is 44 meters long, 22 meters diameter and weight about 7000 tons. It is described in detailed in Section 2.4.

CMS (Compact Muon Solenoid) is designed as a general-purpose experiment. The completed detector will be cylindrical, 21 meters long and 16 meters diameter and weight approximately 12 500 tons. The main highlight features of the detector are: its relatively small size, the powerful solenoid which will produce a 4-tesla magnetic field and its optimization for tracking muons. The detector layout is shown in Figure 2.7 (b).

ALICE (A Large Ion Collider Experiment), shown in Figure 2.7 (c), is a dedicated heavy-ion detector to study the physics of strongly interacting matter at extreme energy densities, where the formation of a new phase of matter, the quark-gluon plasma, is expected.

LHCb (the Large Hadron Collider beauty experiment), shown in Figure 2.7 (d), is an experiment to study specifically B-physics and *CP* violation.

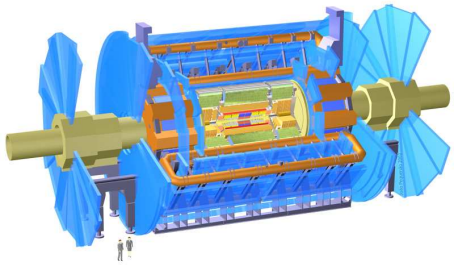

(a) ATLAS experiment.

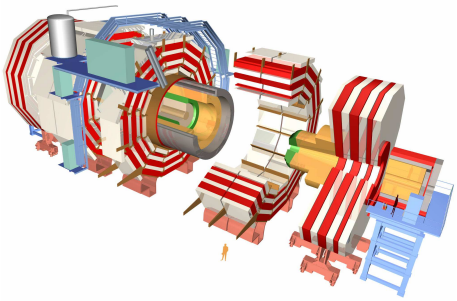

(b) CMS experiment.

(c) ALICE experiment.

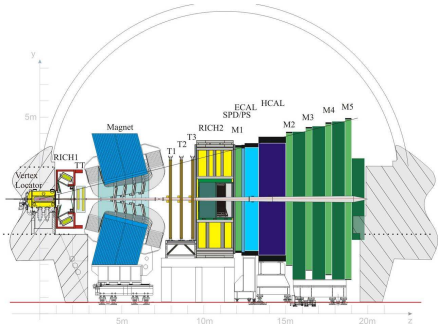

(d) LHCb experiment.

Figure 2.7: LHC experiments.

2.4 A Toroidal LHC ApparatuS (ATLAS)

ATLAS (A Toroidal LHC ApparatuS) is a general-purpose pp detector which is designed to exploit the full discovery potential of the LHC. The LHC offers a large range of physics opportunities, among which the origin of the mass at the electroweak scale is a major focus of interest for ATLAS. The detector optimization is therefore guided by physics issues such as sensitivity to the largest possible Higgs mass range. Other important goals are the searches for supersymmetric particles, for compositeness of the fundamental fermions, as well as the investigation of *CP* violation in B-decays, and detailed studies of the top quark. The ability to cope well with a broad variety of possible physics processes is expected to maximize the detector's potential or the discovery of new, unexpected physics.

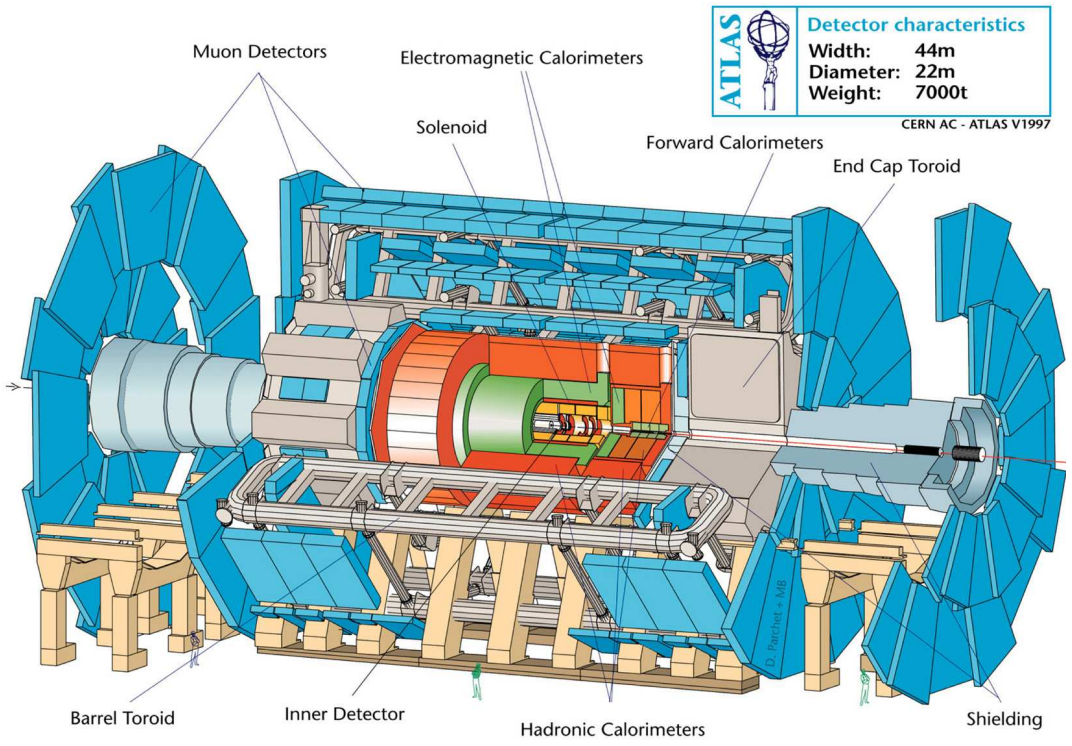

Figure 2.8: Drawing of the ATLAS experiment.

The ATLAS detector, shown in Figure 2.8, consists of four major components:

- Inner detector, which is composed of three subdetectors (the Pixel Detector, the Semiconductor Tracker and the Transition Radiation Tracker) and measures the momentum of each charged particle.
- Calorimeter, which is divided in a electromagnetic and a hadronic part and measures the energies carried by the particles.
- Muon spectrometer, which identifies and measures muons.
- Magnet system, which bends charged particles for momentum measurements.

The interactions of the particles created in the LHC proton collisions going through the ATLAS detectors will create an enormous data flow. To digest these data we need:

- the trigger system.
- the data acquisition system.
- the computing system.

Figure 2.9 shows the typical behaviour of several particles in the different parts of ATLAS, which are described in the following subsections.

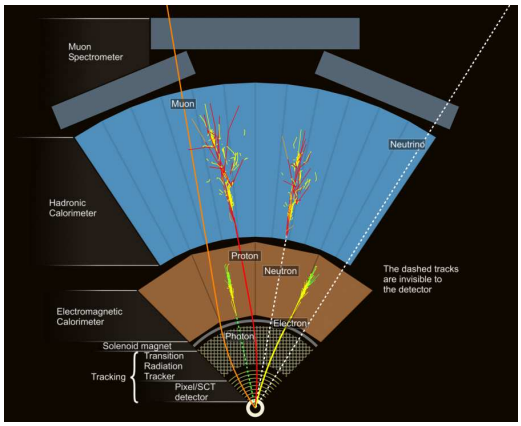

Figure 2.9: A slice of the ATLAS detector. Note the typical tracks left by the different particles going through the detector.

2.4.1 Inner Detector

The task of the Inner Detector (ID) [4] is to reconstruct the tracks and vertices in the event from the LHC beampipe to the electromagnetic calorimeter system with high efficiency. Their main parameters are summarized in Table 2.2. The ID is shown in Figure 2.10 and its parts are described below.

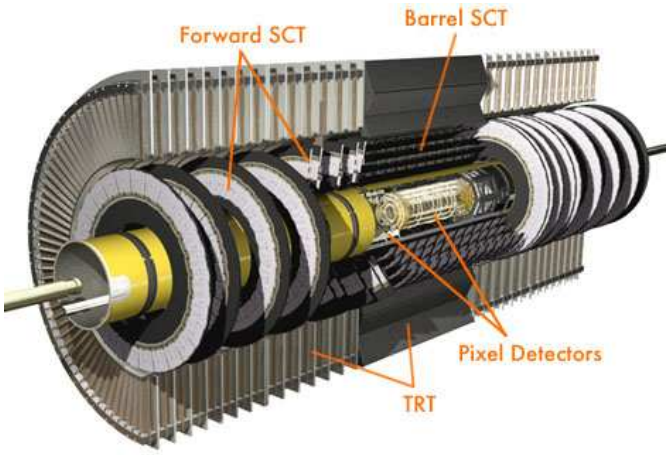

Figure 2.10: Three-dimensional view of the Inner detector.

2.4.1.1 Pixel Detector

The Pixel Detector is designed to provide a very high granularity, high precision set of measurements as close to the interaction point as possible. The system consists of three barrels at average radii of ∼4 cm, 11 cm, and 14 cm, and four disks on each side, between radii of 11 and 20 cm, which complete the angular coverage. The system is designed to be highly modular, containing approximately 1500 identical barrel modules and 1000 identical disk modules.

2.4.1.2 SemiConductor Tracker (SCT)

The Semiconductor Tracker (SCT) is designed to provide four precision measurements per track in the intermediate radial range, contributing to the measurement of momentum, impact parameter and vertex position, as well as providing good pattern recognition by the use of high granularity. The SCT is based upon silicon microstrip detector technology. The detector contains 61 m^2 of silicon detectors, with 6.2 million readout channels. The spatial resolution is 16 μm in $R\phi$ and 580 μm in z.

2.4.1.3 Transition Radiation Tracker (TRT)

The Transition Radiation Tracker (TRT) is based on the use of straw detectors. The barrel contains about 50 000 straws and the end-caps contain 320 000 radial straws. The total number of electronic channels is 420 000.

Table 2.2: Parameters of the Inner Detector.

System	**Position**	**Area (m^2)**	**Resolution σ (μm)**	**Channels (10^6)**	**$\lvert\eta\rvert$ coverage**
Pixels	1 removable barrel layer	0.2	$(R\phi, z) = (12, 66)$	16	2.5
	2 barrel layers	1.4	$(R\phi, z) = (12, 66)$	81	1.7
	4 end-cap disks on each side	0.7	$(R\phi, z) = (12, 77)$	43	1.7 - 2.5
SCT	4 barrel layers	34.4	$(R\phi, z) = (16, 580)$	3.2	1.4
	9 end-cap wheels on each side	26.7	$(R\phi, z) = (16, 580)$	3.0	1.4 - 2.5
TRT	Axial barrel straws		170 (per straw)	0.1	2.5
	Radial end-cap straws		170 (per straw)	0.32	0.7 - 2.5

2.4.2 Calorimetry

The tasks of the calorimeters [5] at hadron colliders are: accurate measurement of the energy and position of electrons and photons; measurement of the energy and direction of jets, and of the missing transverse momentum of the event; particle identification (for instance, separation of electrons and photons from hadrons and jets, and τ hadronic decays from jets) and event selection at the trigger level.

In ATLAS, the central cryostat contains the barrel electromagnetic calorimeter and the 2-tesla superconducting solenoid. Each end-cap cryostat houses an electromagnetic and two hadronic wheels, and one forward calorimeter. The barrel and end-cap cryostats are built out of aluminium, and are vacuum insulated. The total weight of the calorimeter system is about 4000 tons. The ATLAS calorimeters are shown in Figure 2.11 and their main parameters summarized in Table 2.3.

Table 2.3: Coverage, longitudinal segmentation and granularity of the ATLAS calorimeters.

EM CALORIMETER	**Barrel**	**End-Cap**	
Coverage	$\|\eta\|<1.475$	$1.375<\|\eta\|<3.2$	
Longitudinal segmentation	3 samplings	3 samplings	$1.5<\|\eta\|<2.5$
		2 samplings	$1.375<\|\eta\|<1.5$
			$2.5<\|\eta\|<3.2$
Granularity ($\Delta\eta \times \Delta\phi$)			
Sampling 1	0.003×0.1	0.025×0.1	$1.375<\|\eta\|<1.5$
		0.003×0.1	$1.5<\|\eta\|<1.8$
		0.004×0.1	$1.8<\|\eta\|<2.0$
		0.006×0.1	$2.0<\|\eta\|<2.5$
		0.1×0.1	$2.5<\|\eta\|<3.2$
Sampling 2	0.025×0.025	0.025×0.025	$1.375<\|\eta\|<2.5$
		0.1×0.1	$2.5<\|\eta\|<3.2$
Sampling 3	0.05×0.025	0.05×0.025	$1.5<\|\eta\|<2.5$
PRESAMPLER	**Barrel**	**End-Cap**	
Coverage	$\|\eta\|<1.52$	$1.5<\|\eta\|<1.8$	
Longitudinal segmentation	1 sampling	1 sampling	
Granularity ($\Delta\eta \times \Delta\phi$)	0.025×0.1	0.025×0.1	
HADRONIC TILE	**Barrel**	**Extended Barrel**	
Coverage	$\|\eta\|<1.0$	$0.8<\|\eta\|<1.7$	
Longitudinal segmentation	3 samplings	3 samplings	
Granularity ($\Delta\eta \times \Delta\phi$)			
Samplings 1 and 2	0.1×0.1	0.1×0.1	
Sampling 3	0.2×0.1	0.2×0.1	
HADRONIC LAr		**End-Cap**	
Coverage		$1.5<\|\eta\|<3.2$	
Longitudinal segmentation		3 samplings	
Granularity ($\Delta\eta \times \Delta\phi$)		0.1×0.1	$1.5<\|\eta\|<2.5$
		0.2×0.2	$2.5<\|\eta\|<3.2$
FORWARD CALORIMETER		**End-Cap**	
Coverage		$3.1<\|\eta\|<4.9$	
Longitudinal segmentation		3 samplings	
Granularity ($\Delta\eta \times \Delta\phi$)		$\sim 0.2 \times 0.2$	

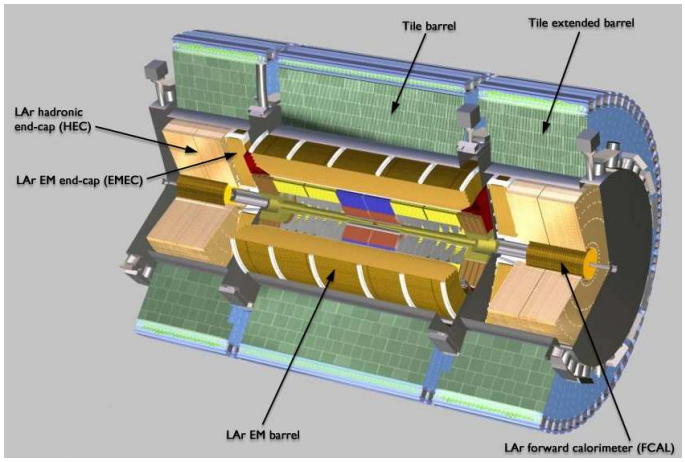

Figure 2.11: Three-dimensional view of the ATLAS calorimeters.

2.4.2.1 Liquid Argon Calorimeter (LAr)

The Liquid Argon [6] sampling calorimeter technique with "accordion-shaped" electrodes is used for all electromagnetic calorimetry covering the pseudorapidity interval $|\eta| < 3.2$. The layout of this system can be seen in Figure 2.12.

Each hadronic end-cap calorimeter (HEC) uses copper as passive medium and liquid argon as active medium. It consists of two independent wheels: HEC1 and HEC2.

The forward calorimeter (FCAL) is composed of three modules; the electromagnetic (FCAL1) and two hadronic modules (FCAL2 and FCAL3). The passive medium in the FCAL1 modules is copper composition and in the hadronic modules is tungsten and sintered tungsten alloy.

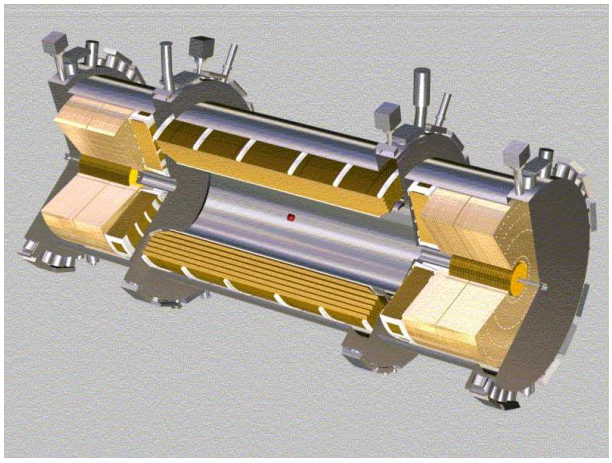

Figure 2.12: Three-dimensional view of the LAr calorimeters inside the cryostat.

2.4.2.2 Tile Calorimeter (TileCal)

The Tile Calorimeter [7], shown in Figure 2.13, is a large hadronic sampling calorimeter which makes use of iron as the absorber material and scintillating plates read out by wavelength shifting (WLS) fibers as the active medium. The new feature of its design is the orientation of the scintillating tiles which are placed in planes perpendicular to the colliding beams and are staggered in depth as Figure 2.14 shows.

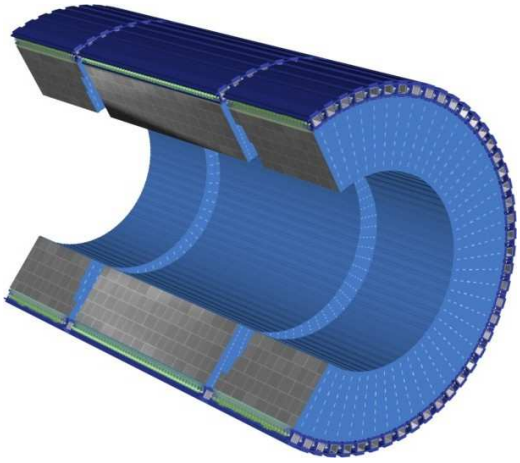

Figure 2.13: Three-dimensional view of the Tile Calorimeter. Note the long barrel and the two extended barrels as well as the 64 modules in the azimuthal direction.

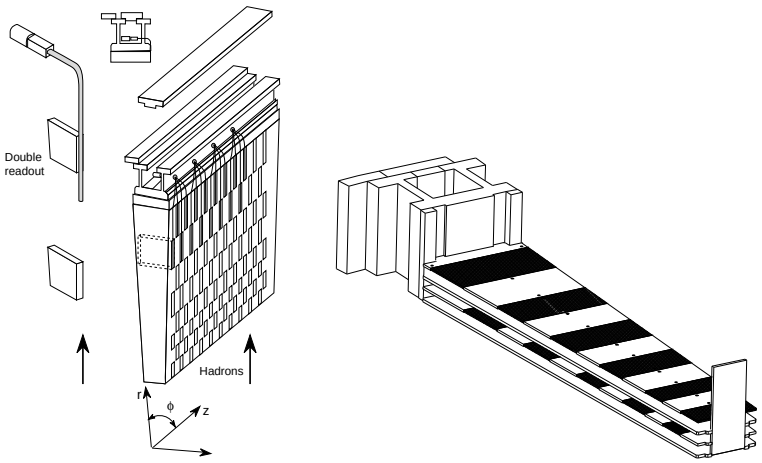

(a) The principle of the Tile Calorimeter design.

(b) Scheme of a TileCal period. The scintillating tiles are shown in black and the iron parts in white.

Figure 2.14: TileCal design.

The Tile Calorimeter is designed as one Long Barrel (LB) and two Extended Barrel (EB) hadron parts, covering the $|\eta| < 1.7$ region. The calorimeter consists of a cylindrical structure with inner and outer radius of 2280 and 4230 mm respectively. The barrel part is 5640 mm in length along the beam axis, while each

of the extended barrel cylinders is 2910 mm long. Each detector cylinder is built of 64 independent wedges along the azimuthal direction. Between the barrel and the extended barrels there is a gap of about 600 mm, which is needed for the Inner Detector and the Liquid Argon cables, electronics and services.

Part of this gap contains an extension of the extended barrel: the Intermediate Tile Calorimeter (ITC), which is a structure stepped in order to maximize the volume of active material in this region, while still leaving room for the services and cables.

All TileCal readout electronics (front-end and back-end) are described in detail in Sections 2.5, 2.6 and 2.7.

2.4.3 Muon Spectrometer

The layout of the ATLAS Muon Spectrometer [8] is shown in Figure 2.15. For the precision measurement of muon tracks in the principal bending direction of the magnetic fields, Monitored Drift Tube (MDT) chambers are used except in the innermost ring of the inner station of the end-caps, where particle fluxes are highest. In this region, covering the pseudorapidity range $2 < |\eta| < 2.7$, Cathode Strip Chambers (CSCs) are employed.

The trigger function in the barrel is provided by three stations of Resistive Plate Chambers (RPCs). They are located on both sides of the middle MDT station, and either directly above or directly below the outer MDT station. In the end-caps, the trigger is provided by three stations of Thin Gap Chambers (TGCs) located near the middle MDT station. See Table 2.4 for detailed information about the Muon Spectrometer chambers.

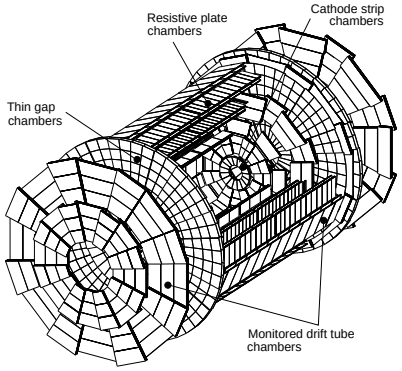

(a) Three-dimensional view of the muon spectrometer instrumentation indicating the areas covered by the four different chamber technologies.

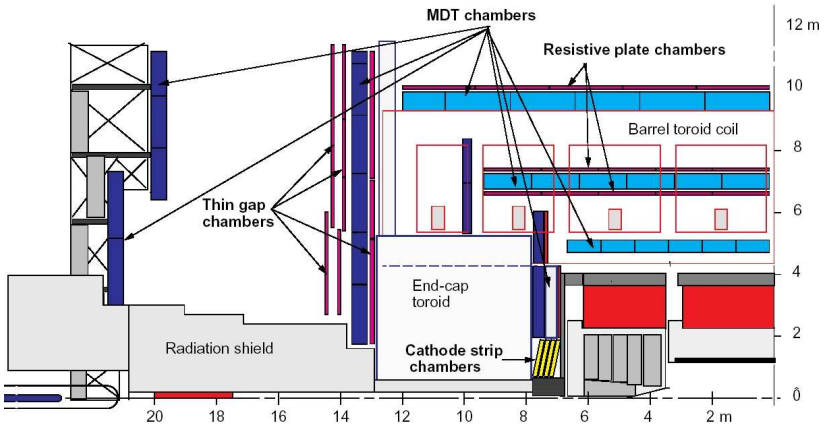

(b) Two-dimensional xy view of the muon spectrometer with the 4 types of chambers in use labeled.

Figure 2.15: Muon spectrometer layout.

Table 2.4: Overview of the muon spectrometer.

	Precision chambers		Trigger chambers	
	CSC	**MDT**	**RPC**	**TGC**
Number of chambers	32	1194	596	192
Number of readout channels	67 000	370 000	355 000	440 000
Area covered (m^2)	27	5500	3650	2900

2.4.4 Magnet System

An essential part of the ATLAS detector setup is the magnet system [9] which provides the bending power required for the momentum measurement of charged particle tracks. It consists of an arrangement of a Central Solenoid (CS) servicing the inner detector trackers with an axial magnetic field, surrounded by a system of three large scale air-core toroids generating a tangential magnetic field for the muon spectrometer: one Barrel Toroid (BT) and two End-Cap Toroids (ECT). Each of the three toroids consists of eight coils.

The magnet system assembly has an overall dimension of 25 meters length by 20 meters in diameter. It has a total weight of 1300 tons, is cooled by liquid helium at 4.8 K and stores a magnetic energy of 1600 MJ. Figure 2.16 shows a scheme of the magnet system, Figure 2.17 shows pictures of its different parts and Table 2.5 summarizes its main parameters.

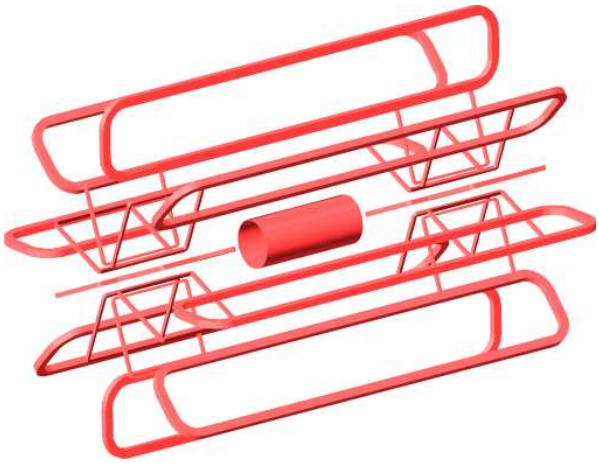

Figure 2.16: Scheme of the magnet system. Note the central solenoid and the three toroids.

The Central Solenoid is designed to provide a 2-tesla strong magnetic field in the central tracking volume. It is a conduction-cooled superconducting solenoid based on a thin-walled construction for minimum thickness to decrease particle scattering effects. In order to reduce material build-up and enhance particle transparency, the solenoid shares its cryostat with the Liquid Argon calorimeter. The solenoid is made as a single layer coil.

The Barrel Toroid consists of eight flat race-track coils each of them consisting of two double pancake windings housed in a common aluminium casing 25 meters long and 5 meters wide. It generates the magnetic field for the central region of the muon detector. The coils are grouped in a torus shape maintained by a system of 16 supporting rings.

Two End-Cap Toroids are positioned inside the Barrel Toroid, one at each end of the Central Solenoid. They provide the magnetic field in the forward regions of the ATLAS detector across a radial span of 1.7 to 5 meters. The eight coils of each End-Cap Toroid are assembled as a single unit inside one large cryostat.

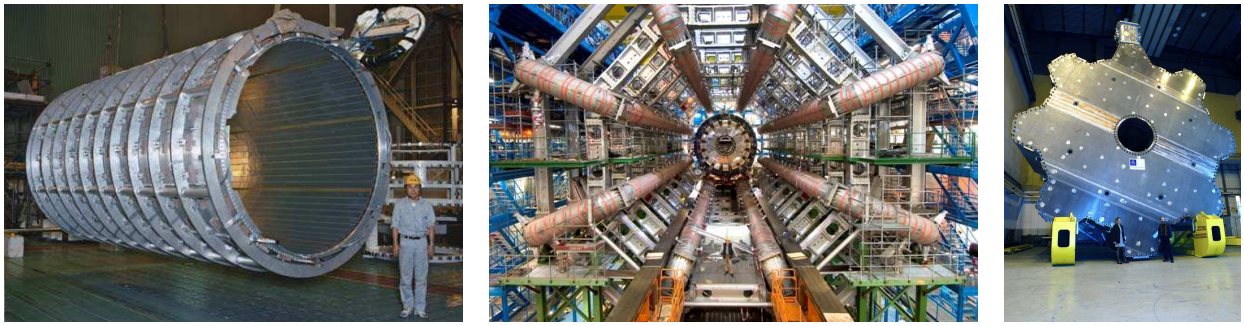

(a) Central Solenoid. (b) Barrel Toroid. (c) End-Cap Toroid.

Figure 2.17: Parts of the ATLAS magnet system.

Table 2.5: Overview of the magnet system parameters.

	Barrel Toroid	End-Cap Toroid	Central Solenoid
Overall Dimensions			
inner diameter	9.4 m	1.65 m	2.46 m
outer diameter	20.1 m	10.7 m	2.63 m
axial length	25.3 m	5.0 m	5.30 m
number of coils	8	2 × 8	1
Mass			
conductor	118 tons	2 × 20.5 tons	3.8 tons
cold mass	370 tons	2 × 160 tons	5.4 tons
total assembly	830 tons	2 × 239 tons	5.7 tons
Coil			
central field			2.0 T
field integral	2 - 6 T m	4 - 8 T m	

2.4.5 Trigger System

The ATLAS trigger and data acquisition system [10] is based on three levels of online event selection, as shown in Figure 2.18. Each trigger level refines the decisions made at the previous level and, where necessary, applies additional selection criteria. Starting from an initial bunch-crossing rate of 40 MHz (interaction rate $\sim 10^9$ Hz at a luminosity of 10^{34} cm^{-2}s^{-1}) the final rate of selected events must be reduced to $\sim$100 Hz for permanent storage.

The level-1 (LVL1) trigger is hardware-based and makes an initial selection based on reduced-granularity

information from a subset of detectors. For instance, high transverse momentum (high p_{T}) muons are identified using only the so-called trigger chambers (RPCs in the barrel and TGCs in the end-caps). The calorimeter selections are based on reduced-granularity information from all the ATLAS calorimeters. Objects searched for by the calorimeter trigger are high p_{T} electrons and photons, jets, and taus decaying into hadrons, as well as large missing and total transverse energy. In the case of the electron/photon and hadron/tau triggers, isolation can be required.

When the LVL1 selection criteria are fulfilled potentially interesting objects may be present. Then, we say we have a Level-1 Accept (L1A) and information about the Region of Interest (RoI) is sent to the next level using a dedicated data path. This information includes the position (η and ϕ) and p_{T} range of candidate objects (high p_{T} muons, electrons/photons, hadrons/taus, jets) and energy sums (missing E_{T} vector and scalar E_{T} value, where E_{T} is transverse energy).

The LVL1 trigger makes available RoI information for all of the objects that contributed to the event being selected; these are called primary RoIs. Furthermore, in order to allow additional requirements to be made at level-2 (LVL2), the LVL1 trigger can provide RoI information for objects that did not contribute to the selection of the event. Such RoIs, typically for objects of relatively low p_{T}, are called secondary RoIs.

The LVL1 maximum rate is 75 kHz (upgradable to 100 kHz) with a 2.5 μs LVL1 detector latency, that is, the time required for each subdetector to provide a trigger decision. It is defined as the time measured from the pp collision until the trigger decision is available to the detector front-end for data transmission.

The LVL2 trigger is software-based and makes use of RoI information provided by the LVL1 trigger. It selectively accesses data from the Read Out Buffers (ROBs), moving on the data that are required in order to make the LVL2 decision. The LVL2 trigger has access to all of the event data, if necessary with the full precision and granularity.

After LVL2, a last stage of selection is performed in the Event Filter (EF). Here the algorithms will be based on offline code. The EF must reduce the rate to a level suitable for permanent storage, currently assumed to be $\sim$100 Hz for full events of size $\sim$1 Mbyte.

The software-based trigger levels (LVL2 and EF) are commonly known as High Level Trigger (HLT), see Section 6.2.

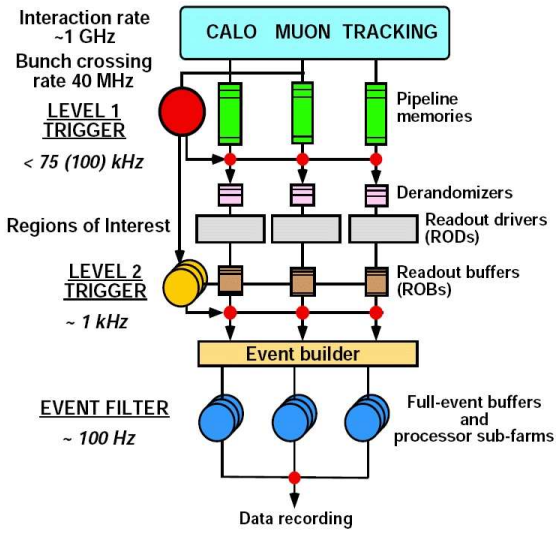

Figure 2.18: Block diagram of the Trigger/DAQ system.

2.5 TileCal Front-End Electronics

The light produced by the particles going through the scintillating tiles is collected by the WLS fiber bundles, which route it to the photomultiplier tubes (PMTs), first stage of the front-end electronics. Figure 2.19 shows the different elements mentioned above.

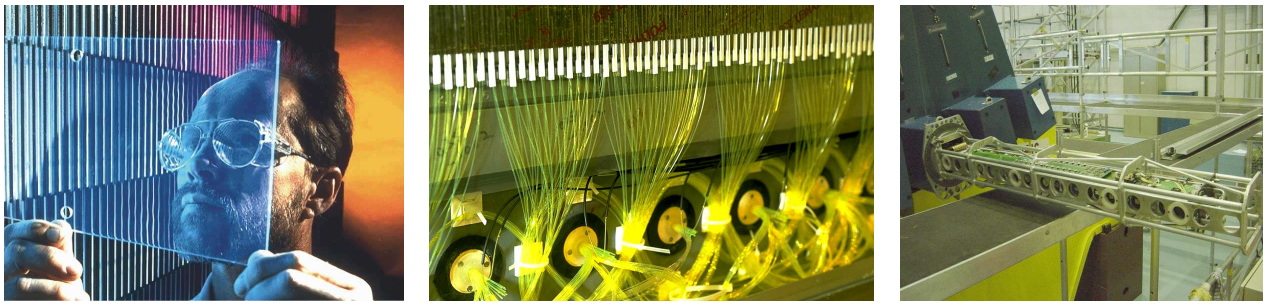

(a) A scintillating tile. (b) WLS fiber bundles. (c) View of a drawer.

Figure 2.19: Different parts of a TileCal module.

All front-end electronics in TileCal are placed in a compact structure called drawer. Two physical drawers are coupled from the electronics point of view forming a new structure called super-drawer. The super-drawers are located inside the back-beam region of the Tile Calorimeter modules and contain the PMT blocks, the pipelines and the HV distributors. There are 256 super-drawers in TileCal. There is a super-drawer per each half barrel module and per each extended barrel module.

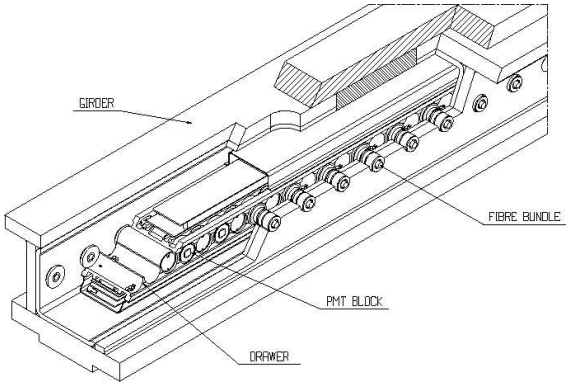

Figure 2.20: Scheme of the drawer inside the girder with all the parts labeled.

2.5.1 PMT Block

The function of a PMT block is to convert light signals from the calorimeter cells into electronic signals. Each PMT block contains a photomultiplier tube, a light mixer, a high voltage divider and a 3-in-1 card, as Figure 2.21 shows.

There is one PMT block assigned to each of the 10 010 fiber bundles in the Tile Calorimeter and each PMT corresponds to one channel for readout. The output of the PMT block is a shaped electronic signal which is subsequently digitized by the electronics inside the super-drawer.

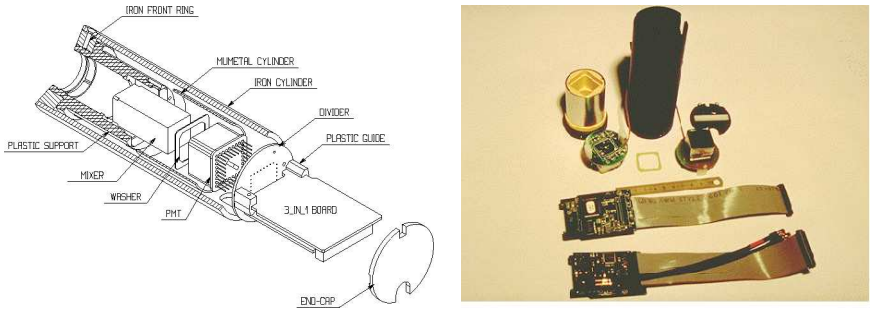

(a) Arrangement of a PMT block.

(b) The components of a PMT block before assembly.

Figure 2.21: PMT block.

2.5.1.1 Photomultiplier Tube

The conversion of the light signals from the fiber bundles to electrical charge is done by the photomultipliers in the PMT blocks. After several studies, the Hamamatsu R5900 PMT was the chosen model to equip the TileCal PMTs.

From 2000 to 2003, the TileCal-Valencia group characterized and tested at IFIC about 1750 photomultipliers which are being employed in TileCal.

2.5.1.2 Light Mixer

The role of this light guide is to mix the light coming from the fibers so that there is no correlation between the position of a fiber and the area of the photocathode which receives its light.

2.5.1.3 HV Divider

The primary purpose of the HV divider is to partition the high voltage between the dynodes of the PMT. The Tile Calorimeter divider also serves as a socket allowing connection of the PMT to the front-end electronics without any interconnecting wires. This design minimizes the capacitance between the PMT and the electronics, and is important to reduce noise and unreliable connections.

2.5.1.4 3-in-1 Board

This board provides three basic functions: pulse shaping and accommodation of the large dynamic range, charge injection calibration and slow integration of the PMT signals for monitoring and calibration.

2.5.2 Analog Trigger Tower Adders

Analog summation is used to build the trigger signals from the TileCal, which are to be used in the LVL1 trigger system of ATLAS. Specific cards for such purpose are placed in the drawers, just below the digitizers. The trigger signals are built taking as input the shaped signals provided by the 3-in-1 cards from the PMT blocks in each trigger tower.

2.5.3 Digitizer System

Figure 2.22 shows a block diagram of this device, in which fast pulse signals from the 3-in-1 cards are digitized in the digitizers boards and sent down a digital pipeline. On receipt of a L1A, the digitizer boards capture an event frame consisting of a string of digitizations. The events (data frames) are stored locally and queued for transmission to the interface link.

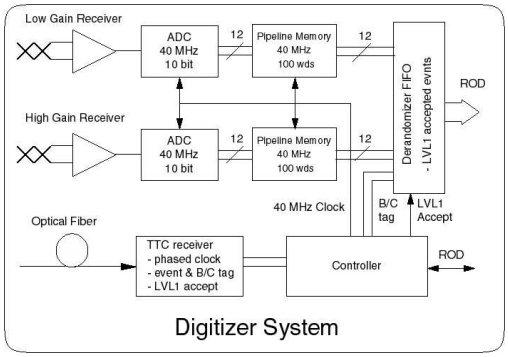

Figure 2.22: Digitizer system for a single channel. Note the high and low gain inputs.

The data presented to the digitizer boards by the 3-in-1 system are delivered with two versions of each signal, a high and a low gain version (being 64 the gain ratio). The data are converted to discrete time format in digitizers formed mainly by commercial ADCs, TTCrx for Trigger and Timing Control (TTC) information receipt and custom Application Specific Integrated Circuit (ASIC) chip TileDMU (Data Management Unit). The criteria used to decide which set of data (high or low gain) remains is the saturation of the samples.

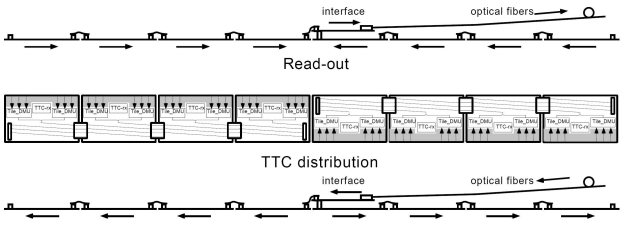

(a) Scheme of the 8 digitizer boards corresponding to a LB super-drawer.

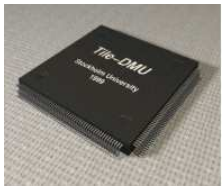

(b) TileDMU chip picture.

Figure 2.23: Components of the digitizer system.

The TileDMU is responsible for reformatting and reordering the digitized data and for sending them to the interface links. Each TileDMU manages 3 ADCs, and each digitizer board has 2 TileDMUs. Therefore there are 8 digitizer boards for LB super-drawers (up to 48 channels, only 45 are needed), and 6 for EB super-drawers (36 possible channels, only 32 are needed). Figure 2.23 shows a scheme of the digitizer boards in a LB super-drawer and a picture of the TileDMU chip.

2.5.4 Interface Links

Figure 2.24 shows a diagram of the interface links. There is one interface board per super-drawer and it provides two main functionalities:

- Receives the TTC information (two fibers) and sends it to digitizers equipped with the TTCrx chip (8 Low Voltage Differential Signaling - LVDS - signals).
- Receives the data (also LVDS) from the up to 8 digitizer boards in a super-drawer, deserializes them and sends them through an optical link to the input stage of the RODs.

The actual design of the interface links is based in S-Link protocol over HP G-Link chips as a physical layer. The implementation is an integrated G-Link Link Source Card (LSC) (640 Mbit/s) working at 16 bits in 40 MHz mode (chip HDMP1032). Dual channel readout is implemented to provide redundancy.

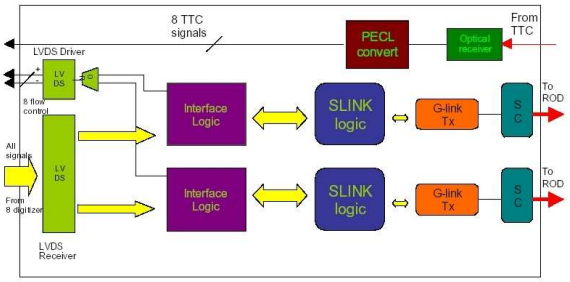

Figure 2.24: Diagram of the interface card. Note the redundant dual output to the ROD.

2.6 TileCal Back-End Electronics

The main element in the back-end electronics is the Read Out Driver (ROD) module. A total number of 38 RODs (32 + 6 spares) have been produced in the TileCal-Valencia laboratory during 2006. They will be placed in 4 ROD crates in the underground counting room USA15 corresponding to the 4 TileCal partitions for data acquisition (EBA, LBA, LBC and EBC). Each partition is managed by the so-called TTC crate which is equipped by standard TTC modules for the LHC experiments. Figure 2.25 shows schematically the DAQ structure for TileCal and the 4 ROD crates. In the following subsections, all back-end modules are described.

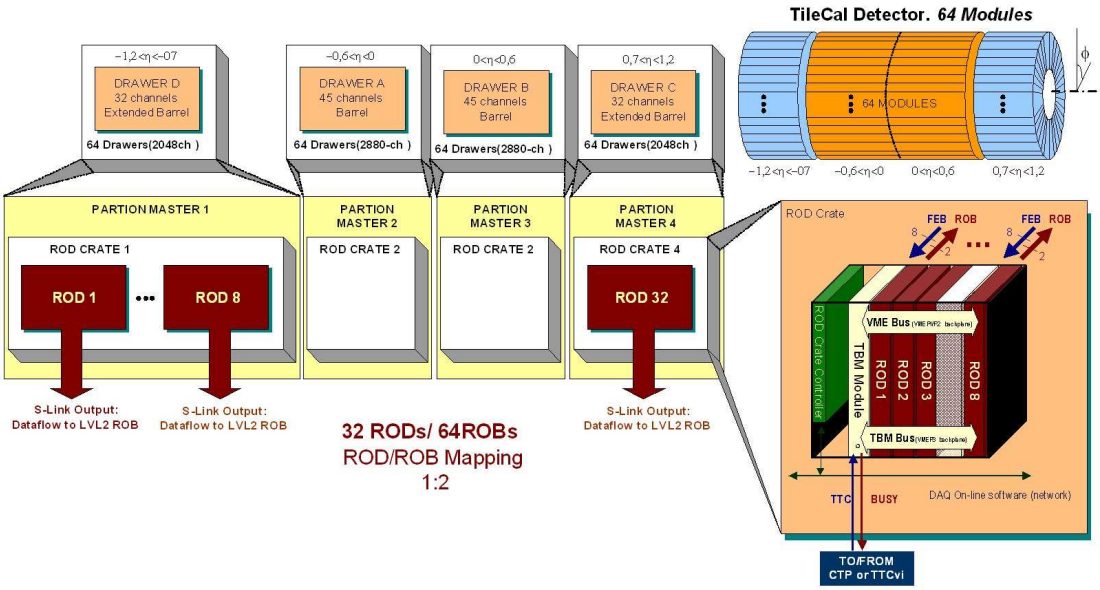

Figure 2.25: Scheme of the TileCal partitions and the corresponding ROD crates.

2.6.1 ROD Crate

The ROD crate is a standard ATLAS 9U crate with remote water cooling power supply. This crate has standard P1 and P2 VME64x backplanes and a custom P3 backplane which allow communication between the ROD Crate Controller (RCC), master module, and all the other slave VME modules in the crate: Trigger and Busy Module (TBM) and 8 ROD motherboards. Each ROD crate can hold up to 21 VME modules. It is planned to include 8 Optical Multiplexer Boards (OMBs) for each ROD crate in the final system setup. Each ROD motherboard is associated with a Transition Module (TM) at the back of the crate. A diagram of a ROD crate is shown in Figure 2.26.

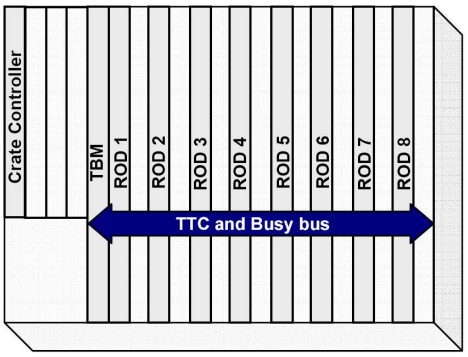

Figure 2.26: Scheme of a TileCal ROD crate.

2.6.1.1 ROD Crate Controller (RCC)

The RCC is a 6U VME module with a CPU for the initialization of the modules as well as monitoring and support of the VME access (for configuration and data transfer). The VP-110 crate controller from Concurrent Technologies [11] is the standard one accepted by the ATLAS collaboration. The next generation of crate controllers by Concurrent Technologies (VP-315 and VP-317) may also be used during the life of the experiment. A picture of the VP-110 is shown in Figure 2.29 (a).

2.6.1.2 Read Out Driver (ROD)

The ROD motherboard [12] is a 9U VME module which can read up to 8 optical fibers from the front-end electronics with the information of a single module each. It can have up to 4 mezzanine cards, called Processing Units (PUs), to process the data online before sending them to the Transition Module installed at the back of the VME crate. In the current setup, two DSP PUs are placed in the PU slots #1 and #3 to process the data. Figure 2.27 (a) shows a picture of a ROD module equipped with two DSP PUs. The ROD functionalities and components are described in Section 2.7.

2.6.1.3 Transition Module (TM)

The TM boards [13] are placed just behind each ROD module. The ROD module sends the data through the backplane P2 and P3 to the TM which transmits them via optical fibers using up to 4 S-Link mezzanine LSCs [14] to the Read Out System (ROS) computer (the next step in the readout chain). Serializer and deserializer chips are located in ROD and TM respectively to allow this functionality due to the limited number of pins in P2 and custom P3. Figure 2.27 (b) shows a picture of a TM equipped with two HOLA LSCs and Figure 2.28 shows the component diagram and data flow for the ROD and the TM.

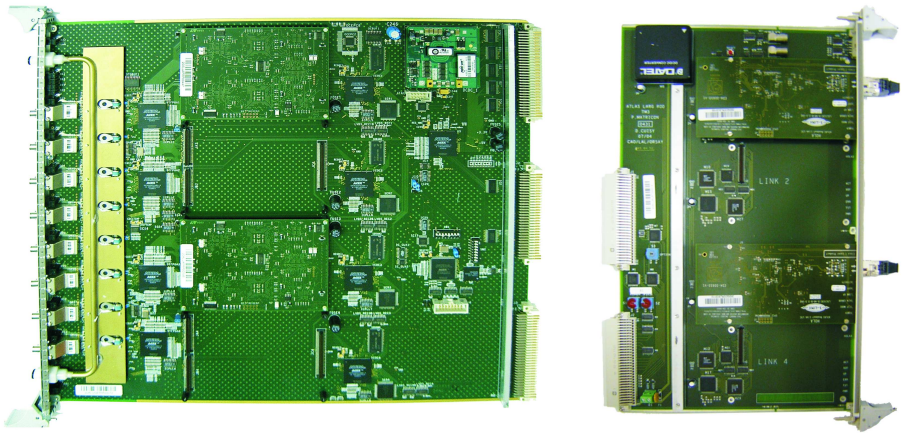

(a) ROD motherboard. (b) Transition Module

Figure 2.27: Read Out Driver and Transition Module pictures. Note that there are only 2 DSP PUs in the ROD motherboard and 2 HOLA LSCs in the Transition Module, as needed in the default operation mode.

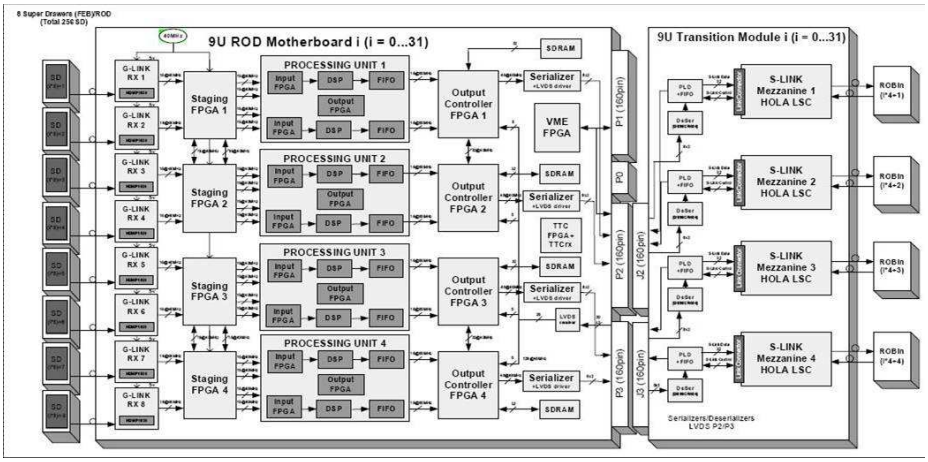

Figure 2.28: Read Out Driver and Transition Module scheme.

2.6.1.4 Trigger and Busy Module (TBM)

The TBM [15] is a 9U VME module which manages TTC and busy signals in the ROD crate. The TBM must be placed in slot #5 in the ROD crate and receives the TTC signals from the trigger system, does the optical to electrical conversion and distributes them to all the ROD modules in the crate through the P3 backplane.

Through the P3 backplane, the TBM also receives the busy signals from the 8 RODs in the crate. These signals are meant to stop the data reception when the ROD is processing previous data. The TBM produces a logical OR of the 8 ROD Busy signals to generate a Crate Busy signal. Figure 2.29 (b) shows a picture of this board.

2.6.1.5 Optical Multiplexer Board (OMB)

TileCal is a redundant acquisition system: two fibers carry the same data from the Interface Cards to the ROD (see Section 2.5.4). In such a radiation hard environment and in a long-lived experiment as ATLAS, this redundancy is mandatory in order to prevent the effect of the malfunctions in the front-end electronics due to radiation damage.

To exploit this redundancy, an Optical Multiplexer Board [16] is being designed by the DSDC group at the *Dpto. Ingeniería Electrónica, Universitat de València*. This 9U VME module will receive the two fibers carrying the same data, check possible errors in them and provide the correct one to the ROD as input. In another operation mode, this module will generate data so that it may also be used as ROD injector.

The 9U OMB is under development at the moment and its production is scheduled for 2007. Nevertheless, a 6U prototype (Figure 2.29 (c)) has been used as data injector to the ROD for production tests and software and firmware developments in laboratory setups until now.

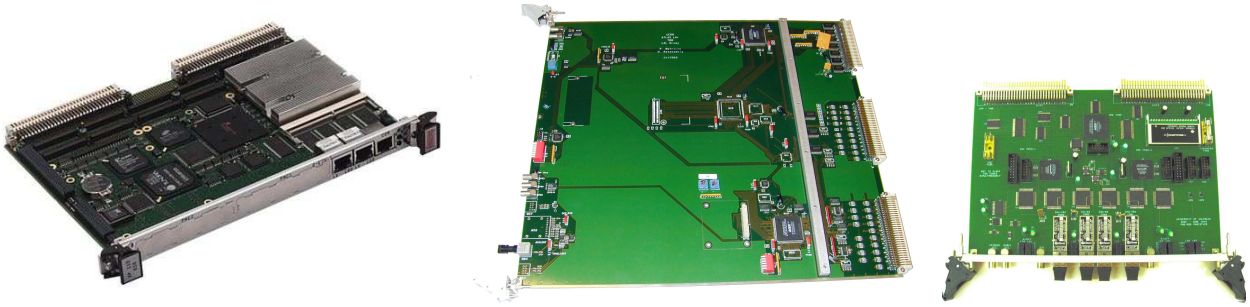

(a) ROD Crate Controller. (b) Trigger and Busy Module. (c) 6U OMB prototype.

Figure 2.29: ROD Crate Controller, Trigger and Busy Module and Optical Multiplexer Board pictures.

2.7 ROD Description

In the following subsections, the components of the ROD are described. The ROD main functionalities are:

- **Data processing:** raw data gathering from the first level de-randomizers at the L1A event rate of 100 kHz. The ROD provides energy, timing and pile-up estimation (χ^2) to the next trigger level by processing the data with the algorithms implemented in the PUs (see Chapter 3). Depending on the DAQ constraints (pile-up, high energy events, ...) there is also the possibility to send only raw data without processing.

- **Trigger:** TTC signals will be present (with a latency $\sim$2 μs after L1A) at each module, providing ROD L1ID (Level 1 Identifier), BCID (Bunch Crossing Identifier) and Ttype (Trigger type).

- **Error detection:** the ROD checks that the owner BCID and L1ID numbers match with the numbers received from the front-end. If a mismatch is detected, an error flag is set with some error code.

- **Data links:** at a L1A event rate of 100 kHz the ROD sends the data to the next step in the acquisition chain (ROBs) using the standard ATLAS Read Out Links (ROLs).

- **Busy generation:** the TBM provides a busy signal which stops the L1A generation, performing an OR operation with the ROD busy signals coming from all the RODs in a partition.

- **Local monitoring:** part of the data can be read through VME for monitoring tasks without introducing dead-time or additional latency.

2.7.1 Optical receivers and G-link chips

The ROD motherboard has up to 8 optical receivers (ORXs). These ORXs are mezzanine boards that receive the optical signals coming from the front-end electronics. Then 8 G-link chips (HDMP-1024) deserialize the incoming data and send them to the Staging Field Programmable Gate Arrays (FPGAs).

2.7.2 Staging FPGAs

Four Staging FPGAs (ACEX EP1k50) are used in the ROD motherboard. Each one receives deserialized data from two G-link chips. The main functionalities of this device are to route the external input data to the PU, monitor the G-link temperature, generate internal event data and send them to the PU for tests.

The Staging FPGA is responsible for receiving the incoming data into the ROD from two different G-link chips and route them to the PU. In the default operation mode, called Staging mode, the data coming from four G-links are sent to a single PU (using a bus between each pair of Staging FPGAs). There is also the possibility to work in the so-called Full Mode, where the data from two G-links are sent to a single PU.

2.7.3 Output Controller FPGAs

An ACEX EP1k100 is used as Output Controller (OC) FPGA [17]. There are 4 OCs in a ROD motherboard. The OC reads the data from the FIFOs of the Processing Units and sends them either to a SDRAM to read the data through the VME protocol or to a serializer chip to send the data to the TM.

2.7.4 VME FPGA

The VME interface is implemented in a FPGA ACEX EP1k100 [18]. The ROD module is considered as a VME slave module and can be accessed by the RCC. The data bus is D32 (32-bit data words) and the addressing is A32 (32-bit address words) for data transfer.

2.7.5 TTC Controller FPGA

The TTC FPGA [19] is an APEX EP1k30 and gets the LHC clock from the backplane via the TBM to distribute it to the ROD.

The TTC FPGA is responsible for providing the ROD with all the TTC signals and information for the different trigger operation modes. The TTC information sent by the TBM is received by the TTCrx chip [20] in the ROD and recovered by the TTC Controller FPGA, which distributes it to all PUs.

2.7.6 Processing Units (PUs)

Online data processing is done by the so-called Processing Units which are 120 mm $\times$ 85 mm mezzanine cards which are connected to the ROD motherboard via 3 connectors. Each ROD motherboard can hold up to 4 PU daughterboards.

2.7.6.1 DSP PU

The Digital Signal Processor (DSP) PU [21] is composed of two blocks, each one with an input FPGA Cyclone EP1C6, a TMS320C6414 DSP from Texas Instruments and an external output FIFO. The DSP PU also contains an output FPGA Cyclone EP1C6 used for the VME and TTC interface. A picture of this device and its layout

are shown in Figure 2.30. The input FPGAs and the DSPs can be programmed by uploading the corresponding code through the VME interface.

The main functions of the DSP PU are:

- Data flow management.
- Data formatting.
- TTC reception.
- Buffering and synchronization.
- Data processing with online algorithms.
- Online histogramming.
- Error detection, several checks can be performed like the presence of the start and the end of an event, the parity of each word, etc.

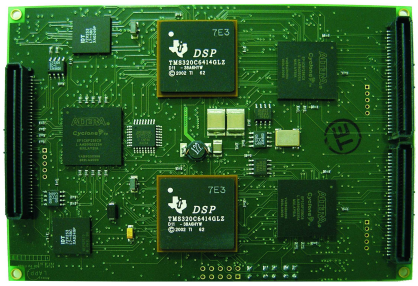

(a) ROD DSP PU picture. Note that the front-end input data come from right to left.

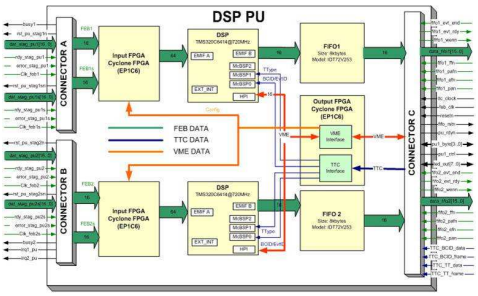

(b) ROD DSP PU scheme. Note the arrows according to the data flow.

Figure 2.30: ROD DSP PU.

Chapter 3

TileCal ROD DSP Online Algorithms

Taking advantage of its high computing power and processing speed, some algorithms are being implemented in the TileCal ROD DSP core in order to process the incoming front-end data. This way, the output from the algorithms will be available in the ROD data in order to contribute to the High Level Trigger decision. These algorithms are: Optimal Filtering, low p_{T} Muon Tagging (MTag) and Missing E_{T} algorithms. However, the limited output bandwidth and processing time available ($\sim$10 μs) will constrain the amount of algorithms in the DSP and their implementation.

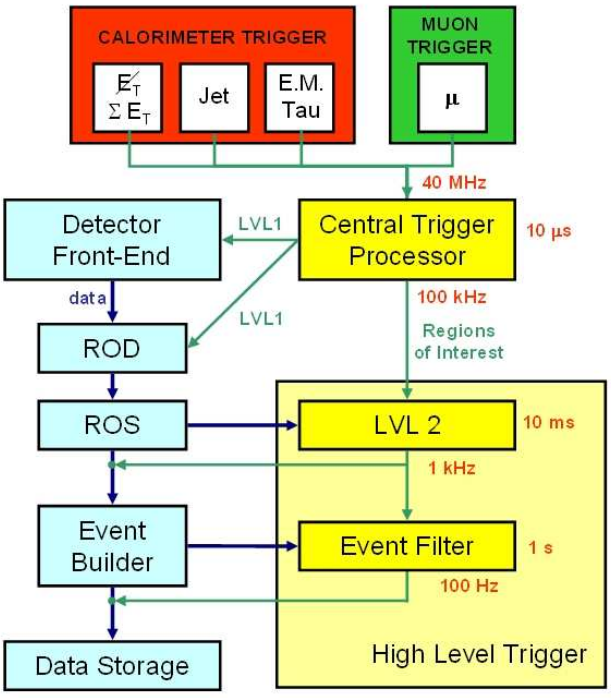

Figure 3.1: Diagram with the trigger (green) and data flow (blue) paths with all the elements involved. Note the latencies and rates for each trigger level.

Figure 3.1 shows a data flow diagram of the trigger system with timings and the role played by the ROD. The LVL1 trigger decision is taken with hardware information from calorimeters and muon chambers. When an event is selected, the L1A information is sent to the detector front-end (so that data from the appropriate bunch crossing are transmitted) and to the RODs (for synchronization with the incoming events).

All the raw data from events accepted by LVL1 are processed by the ROD with a maximum latency of 10 μs to avoid introducing dead time. The output data from the RODs are sent to the ROS, where they are available for the High Level Trigger (HLT).

LVL2 algorithms are applied to the data processed by the ROD using the regions of interest selected by LVL1 as starting point. Due to the limited LVL2 latency (10 ms) the algorithms used in this step should be fast in terms of CPU time consumption and data access speed. Section 6.2 describes in detail the algorithms used for HLT decision in the muon sector.

This chapter will discuss the main features of the ROD DSP, the methods which can be used to reconstruct the pulse shape after the digitization (Flat Filtering, Fit method and Optimal Filtering algorithms), the implementation of the MTag algorithm and the output ROD data format used during the cosmics runs in TileCal commissioning.

3.1 TMS320C6414-7E3 DSP Description

The TileCal ROD PUs use the TMS320C6414-7E3 DSP which is a fixed-point digital signal processor developed by Texas Instruments. This processor belongs to the TMS320C64x™ (C64x™) device family [22], the highest-performance fixed-point DSP generation in the TMS320C6000™ DSP platform.

The C64x™ devices are based on the very-long-instruction-word architecture, very convenient for multichannel and multifunction applications. Their core processor has 64 general-purpose registers of 32-bit word length and eight highly independent functional units - two multipliers for a 32-bit result and six arithmetic logic units - with VelociTI.2™ extensions. The C64x can produce four 16-bit multiply-accumulates (MACs) per cycle for a total of 2880 million MACs per second (MMACS), or eight 8-bit MACs per cycle for a total of 5760 MMACS.

In particular, the main features of the TMS320C6414-7E3 DSP are:

- 1.39-ns Instruction Cycle Time.
- 720-MHz Clock Rate.
- Eight 32-Bit Instructions/Cycle.
- 5760 million instruction per second.

3.2 Energy Reconstruction Algorithms

In the following subsections the algorithms developed by the TileCal collaboration for energy reconstruction from the digitizer samples are presented.

3.2.1 Flat Filtering

The Flat Filter (FF) energy reconstruction method is based on an approximation of the pulse area which is proportional to the energy deposited. This way, the area of the pulse A is estimated as:

$$A = C \max\left(\sum_{i=j}^{j+4}(s_i - p)\right) \qquad j = 1, 2, \ldots, (n-4) \tag{3.1}$$

where C represents the constant transforming the ADC counts into pC, n is the number of samples, s_i is the sample at time t_i and p is the value of the pedestal, which can be estimated as the first sample s_1.

It is one of the simplest and fastest methods. However, pulse time information is not provided by this method and the others give better results in terms of energy resolution. In addition, the usage of the maximal sum introduces a positive bias in channels without signal.

3.2.2 Fit Method

The Fit Method (FM) is based on fitting the pulse shape to the available samples of each event. The energy is reconstructed as the amplitude of the signal. The fit function $f(t)$ has 3 parameters:

$$f(t) = Ag(t - \tau) + p \tag{3.2}$$

where g is the normalized pulse shape function, τ represents the phase (peak position in time), A stands for the amplitude of the signal and p is a constant pedestal. Note that in ATLAS the phase will be fixed, thus the fit will in principle have only 2 free parameters (amplitude and pedestal).

The pulse shape used in FM is the following:

$$g(t) = B\left(\frac{t-\tau}{\lambda}\right)^{\mu} \exp\left[-\mu\left(\frac{t-\tau}{\lambda}\right)\right] + c \tag{3.3}$$

where B, μ, τ, λ and c are parameters of the function. Figure 3.2 shows the typical digitizer pulse shape, with the samples available for energy reconstruction.

FM is currently used as the default energy reconstruction method in TileCal offline reconstruction for simulated and real data.

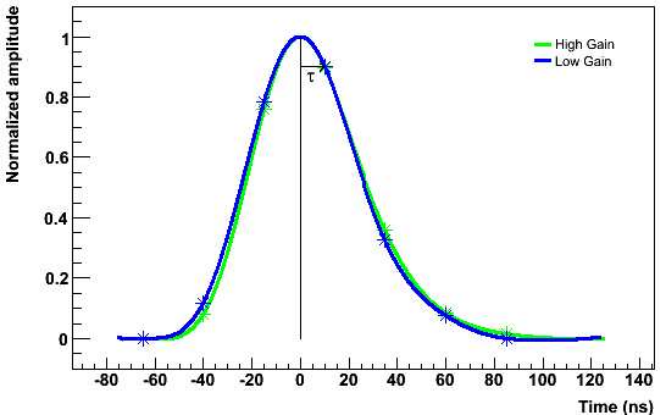

Figure 3.2: Normalized pulse shape for high and low gain. The 25 ns samples from the signal are shown with stars.

3.2.3 Optimal Filtering

The Optimal Filtering (OF) algorithm [23] reconstructs the amplitude of the pulse (which is proportional to the energy deposition) as a weighted sum of the digitized samples in such a way that the contribution of the noise is minimized.

The first version developed, known as OF1, also computes the time of the signal and a quality factor of the reconstruction. The equations used in this algorithm for amplitude, time and quality factor Q calculation are the following:

$$A = \sum_{i=1}^{n} a_i(s_i - p) \tag{3.4}$$

$$\tau = \frac{1}{A}\sum_{i=1}^{n} b_i(s_i - p) \tag{3.5}$$

$$Q = \frac{1}{A}\sum_{i=1}^{n} |Ag_i - s_i + p| \tag{3.6}$$

where A is the reconstructed amplitude of the signal, τ is the reconstructed time of the signal, n is the number of samples, s_i are the digital samples, p is the value of the pedestal, a_i are the weights for the amplitude, b_i are the weights for the time and g_i is the shape form factor for the sample i.

The pedestal is calculated as the average of the first and the last sample:

$$p = \frac{s_1 + s_n}{2} \tag{3.7}$$

The weights a_i and b_i used in the OF are calculated from the signal shape (obtained from charge injection calibration runs) and the noise autocorrelation function (obtained from pedestal runs) so that the sigma of

the energy and time distribution is minimized. As the weights are calculated from the pulse shapes, different values of τ will lead to different values for the weights.

The calculation of the pedestal in (3.7) may be an understimation, because the end of the signal pulses goes below the baseline, as shown in Figure 3.2. In consequence, further developments in the pedestal treatment were done and a new version of the algorithm, called OF2, was developed in which the pedestal value (together with amplitude and phase) is obtained as a linear combination of the pulse samples without previous pedestal substraction. The equations used in OF2 are the following:

$$A = \sum_{i=1}^{n} a_i s_i \tag{3.8}$$

$$\tau = \frac{1}{A} \sum_{i=1}^{n} b_i s_i \tag{3.9}$$

$$p = \sum_{i=1}^{n} c_i s_i \tag{3.10}$$

Note that the set of weights used for amplitude and phase calculation (a_i and b_i) in OF2 is not the same as in OF1 due to the different pedestal treatment.

A third version of the algorithm is also in use at the moment, which computes the amplitude and the pedestal of the pulse as in OF1 but making one iteration in order to apply the weights for the phase obtained in the previous iteration. This version is known as OF1i1 (OF1 with 1 iteration) and is meant to treat non-synchronized signals with unknown phase, like in the case of cosmic rays.

3.3 Low p_{T} Muon Tagging Algorithm

3.3.1 Muon Energy Loss in TileCal

The mean rate of energy loss [24] (or stopping power) for moderately relativistic charged particles is given by the Bethe-Bloch equation:

$$-\frac{\mathrm{d}E}{\mathrm{d}x} = Kz^2 \frac{Z}{A} \frac{1}{\beta^2} \left[\frac{1}{2} \ln \frac{2m_{\mathrm{e}} c^2 \beta^2 \gamma^2 T_{\max}}{I^2} - \beta^2 - \frac{\delta}{2} \right] \tag{3.11}$$

where K = 0.307 MeV cm^2
z is the charge of the incident particle
Z is the atomic number of absorber
A is the atomic mass of absorber (g mol^{-1})
β is the speed of the incident particle in c units
$m_{\mathrm{e}}c^2$ is the electron mass $\times c^2$
γ is the relativistic factor
I (eV) is the mean excitation energy of the target material
δ is the density effect correction to ionization energy loss

where $T_{\max}$ is the maximum kinetic energy for a particle with mass M, expressed by:

$$T_{\max} = \frac{2m_{\mathrm{e}}c^2\beta^2\gamma^2}{1 + 2\gamma m_{\mathrm{e}}/M + (m_{\mathrm{e}}/M)^2} \tag{3.12}$$

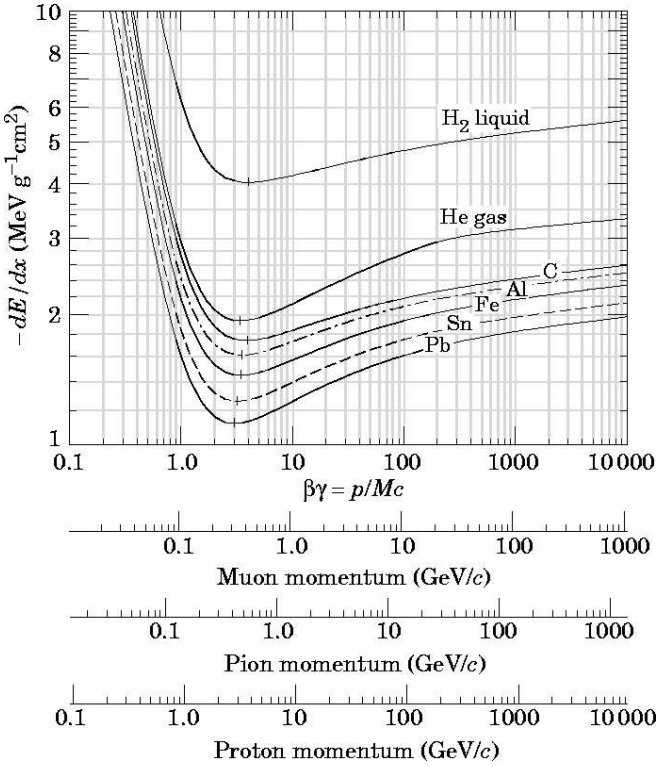

Figure 3.3: Average rate of energy loss for different particles in several materials.

Figure 3.3 shows the mean energy loss rate for several particles as a function of their momentum in different materials.

The critical energy is defined as the energy at which the bremsstrahlung loss rate and the ionization loss rate are equal. The critical energy for muons $E_{\mu c}$ is around ∼200 GeV. In the energy range from ∼1 GeV to ∼200 GeV muons behave like Minimum Ionizing Particles (MIPs) as their energy loss is close to the minimum (see Figure 3.3) and almost constant in the whole range (∼1.5 MeV g^{-1} cm^2). Taking into account this value,

the mean energy lost by muons going through TileCal will be ∼2.5 GeV.

3.3.2 Algorithm Description

The aim of this low p_{T} Muon Tagging algorithm is to exploit the TileCal capability for detecting muons in the low p_{T} range as a complement to the muon spectrometer, which is only efficient when $p_{\mathrm{T}} > 6$ GeV.

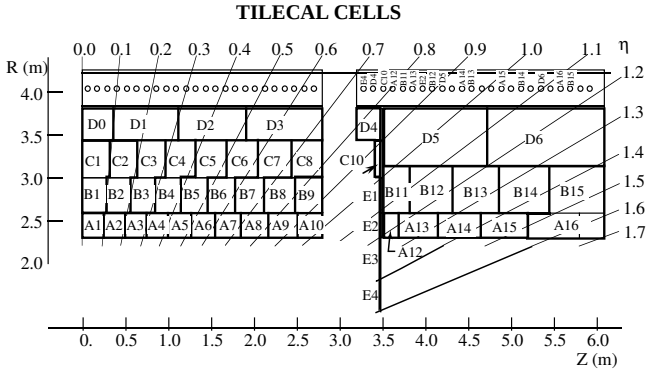

Figure 3.4: Diagram of the TileCal cells.

The basics of the algorithm are to search for muons taking into account the energy deposited in each layer of TileCal and taking advantage of its segmentation. Figure 3.4 shows the TileCal cell structure with 3 layers (A, BC and D cells) and with a projective geometry in η. In order to identify the muons, the typical energy deposition in each cell is delimited by a higher and a lower threshold:

$$thr_i^{\mathrm{low}} \leq E_i \leq thr_i^{\mathrm{high}} \qquad i = 1, 2, 3 \tag{3.13}$$

If this condition is fulfilled in each of the 3 layers with a projective pattern in η, the muon is tagged. In order to be efficient on events in which the muon loses a considerable fraction of its energy in one of the layers, muons are also tagged if (3.13) is fulfilled in two layers and in the third one the energy deposition is greater than the lower threshold.

The lower energy threshold is meant to cut electronic noise and minimum bias pile-up events. In this algorithm, all cells have the same lower energy threshold values, which is taken as 2σ of electronics noise distribution:

$$thr^{\mathrm{low}} = 150\,\mathrm{MeV} \tag{3.14}$$

Note that the probability that uncorrelated electronic noise flags a muon is the product of the probability of noise above the low energy threshold in the three calorimeter layers. With a 2σ threshold level, one can estimate the probability of fake muons due to electronic noise to be $\sim 1.2 \times 10^{-5}$.

The higher energy thresholds are meant to delimit the maximum muon energy deposition while eliminating hadronic showers and tails. These thresholds are determined for each individual cell as, depending on the pseudorapidity of its trajectory, the muon goes through different amount of material (iron and scintillating

Table 3.1: Energy thresholds for long barrel cells.

A cells	Threshold (GeV)	BC cells	Threshold (GeV)	D cells	Threshold (GeV)
A±1	1.35	BC±1	2.55	D0	1.59
A±2	0.96	BC±2	1.98	D±1	1.11
A±3	0.87	BC±3	1.77	D±2	1.05
A±4	0.75	BC±4	1.89	D±3	1.05
A±5	0.84	BC±5	1.86		
A±6	0.84	BC±6	1.80		
A±7	0.93	BC±7	1.89		
A±8	0.84	BC±8	1.86		
A±9	0.96	B±9	1.11		
A±8	0.90				

Table 3.2: Energy thresholds for extended barrel cells.

A cells	Threshold (GeV)	B cells	Threshold (GeV)	D cells	Threshold (GeV)
A±12	0.81	C±10	0.39	D±4	0.90
A±13	1.14	B±11	1.05	D±5	2.10
A±14	1.23	B±12	1.38	D±6	2.37
A±15	1.38	B±13	1.44		
A±16	1.68	B±14	1.50		
		B±15	1.68		

tiles), changing in consequence its energy deposition pattern in the TileCal cells. The values of the higher energy thresholds for all cells are in Tables 3.1 and 3.2, as used in [25].

The usage of this algorithm in the ROD DSP has some limitations. Each DSP processes only the information from 2 super-drawers sequentially, so in principle it will only be possible to look for muons in a single module. Also, with the TileCal geometry shown in Figure 3.4, some towers are split between long barrel and extended barrel. Hence, it is not possible to use this algorithm in these towers.

With this algorithm definition and its implementation in the ROD DSP, some problems can appear due to the effect of the ATLAS magnetic field in the muon trajectory and the non-ideal projective geometry of TileCal. In the first case, the magnetic field can bend the trajectory of the muon so that it goes through two TileCal modules, as shown in Figure 3.5. Then the muon would not be tagged at the DSP level. In the second case, the particle can deposit energy in more than one calorimeter tower, as shown in Figure 3.5, which can lead to a double tag of the same muon. A protection against tagging the same muon twice in two contiguous towers is implemented in the code.

The feasibility of a low p_T Muon Tagging Algorithm in the Tile Calorimeter has been proven extensively by the TileCal group in Pisa [26, 27, 28].

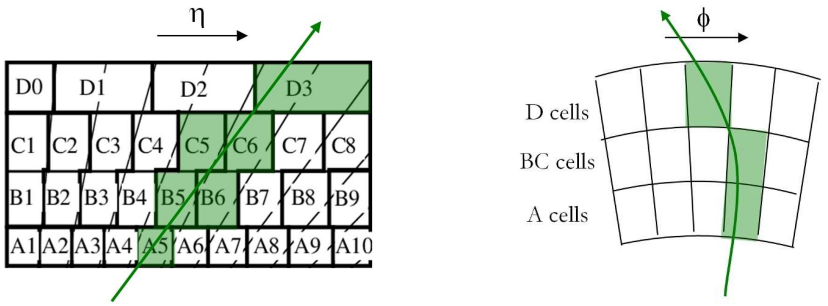

(a) Muon path going through several towers in η.

(b) Muon bent by the magnetic field going through several modules.

Figure 3.5: Example of muon trajectories which may lead to problems in the MTag algorithm.

3.3.3 Algorithm Implementation in the DSP core

All the code and binaries needed for DSP PU booting and operation are collected in the Tile_DSP package. This code has been developed using the Code Composer Studio™ software and it is currently written in C.

The structure of the Tile_DSP package is shown in Figure 3.6 and all the code is available in the TileCal-Valencia Concurrent Version System (CVS) repository, browsable from this address:

`http://evalu35.ific.uv.es/cgi-bin/viewcvs.cgi/detectors/Tile/`

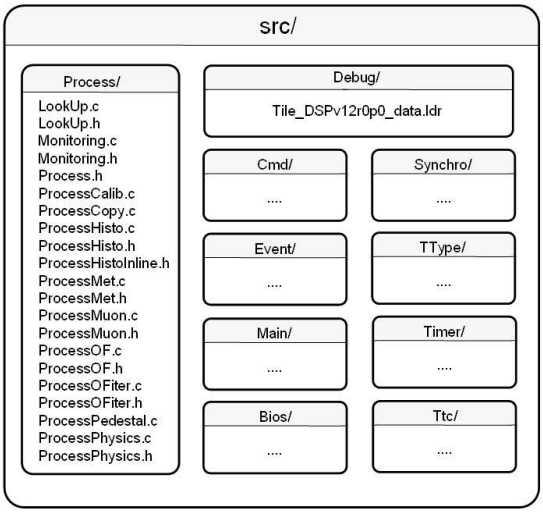

Figure 3.6: Directory structure of the Tile_DSP package.

In particular, the MTag algorithm is implemented in the ProcessMuon.c and ProcessMuon.h files. The MTag algorithm uses the energy previously reconstructed with Optimal Filtering, whose output is currently the amplitude of the photomultiplier signal expressed in ADC counts. The MTag algorithm computes the cell energy and applies the algorithm explained above. In order to avoid operations, the energy thresholds have

been expressed in ADC counts.

The conversion from ADC counts to MeV (or vice versa) is done using the following calibration constants, taking into account that the high gain is used to measure signals from 0 to 12 pC and the low gain is used to measure signals from 12 to 800 pC:

- For high gain:
  - A and BC cells:
$$\frac{1}{64} \times \frac{800.0}{1023.0} \frac{\mathrm{pC}}{\mathrm{ADC}} \times \frac{1000}{1.050} \frac{\mathrm{MeV}}{\mathrm{pC}} = 12 \frac{\mathrm{MeV}}{\mathrm{ADC}} \tag{3.15}$$
  - D cells:
$$\frac{1}{1.2} \times \frac{1}{64} \times \frac{800.0}{1023.0} \frac{\mathrm{pC}}{\mathrm{ADC}} \times \frac{1000}{1.050} \frac{\mathrm{MeV}}{\mathrm{pC}} = 10 \frac{\mathrm{MeV}}{\mathrm{ADC}} \tag{3.16}$$
- For low gain:
  - A and BC cells:
$$\frac{800.0}{1023.0} \frac{\mathrm{pC}}{\mathrm{ADC}} \times \frac{1000}{1.050} \frac{\mathrm{MeV}}{\mathrm{pC}} = 745 \frac{\mathrm{MeV}}{\mathrm{ADC}} \tag{3.17}$$
  - D cells:
$$\frac{1}{1.2} \times \frac{800.0}{1023.0} \frac{\mathrm{pC}}{\mathrm{ADC}} \times \frac{1000}{1.050} \frac{\mathrm{MeV}}{\mathrm{pC}} = 621 \frac{\mathrm{MeV}}{\mathrm{ADC}} \tag{3.18}$$

The 20% difference between D cells and the A and BC cells is due to a different high voltage equalization to improve the signal to noise ratio for a LVL1 muon trigger using those cells.

The functions used for the MTag implementation in the DSP are declared in the Process.h file and defined in the ProcessMuon.c file. All the energy thresholds applied are taken from the ProcessMuon.h file. These functions are the following:

- `void ECellsLB(int* G, int* E, INT32* E_A, INT32* E_BC, INT32* E_D):`

  In this function the energy of half a long barrel cells ($0 < |\eta| < 0.8$) is calculated as a sum of the corresponding channels (see Appendix B), taking as input the channel energy in ADC counts reconstructed in the DSP with Optimal Filtering. In order to achieve better precision in the DSP, the energy values calcualted by OF (and consequently the cell energy values obtained here) are scaled by a factor 16.

- `void ECellsEB(int* G, int* E, INT32* E_A, INT32* E_BC, INT32* E_D):`

  In this function the energy of one extended barrel cells ($1.1 < |\eta| < 1.5$) is calculated as a sum of the corresponding channels (see Appendix B), taking as input the channel energy in ADC counts reconstructed in the DSP with Optimal Filtering. In order to achieve better precision in the DSP, the energy values calcualted by OF (and consequently the cell energy values obtained here) are scaled by a factor 16.

- `void MTagLB(int* gain, int* data, UINT32* Muon):`

  In this function the MTag algorithm is applied to look for muons in half a barrel (LBA or LBC). The corresponding energy thresholds (in ADC counts and taking into account the scale factor used in the energy calculation) are applied to the cell energy calculated in the function ECellsLB above. The threshold values are implemented as a fast look up table. The function applies the condition (3.13) over all the cells in the D layer and in case it is fulfilled the cell is flagged as a "muon candidate". Then, the same condition is applied to the cells in the BC and A layers placed below the candidates found following a

projective pattern. Finally, the muon is tagged if condition (3.13) is true for the 3 layers (or for 2 layers and in the third one the energy deposition is larger than the lower threshold). As output of this function a word is added to the MTag-MET fragment (see Section 3.4.2.3).

- `void MTagEB(int* gain, int* data, UINT32* Muon):`

  In this function the MTag algorithm is applied to look for muons in an extended barrel (EBA or EBC). The corresponding energy thresholds (in ADC counts and taking into account the scale factor used in the energy calculation) are applied to the cell energy calculated in the function ECellsEB above. The threshold values are implemented as a fast look up table. The function applies the condition (3.13) over all the cells in the D layer and in case it is fulfilled the cell is flagged as a "muon candidate". Then, the same condition is applied to the cells in the B and A layers placed below the candidates found following a projective pattern. Finally, the muon is tagged if condition (3.13) is true for the 3 layers (or for 2 layers and in the third one the energy deposition is larger than the lower threshold). As output of this function a word is added to the MTag-MET fragment (see Section 3.4.2.3).

3.4 ROD Data Format Description

The structure of a full ATLAS event [29] is modular as shown in Figure 3.7. The event raw data contains one or more Sub-detector fragments, which contain one or more ROS fragments. A ROS fragment is also formed by one or more ROB fragments, which have one ROD fragment.

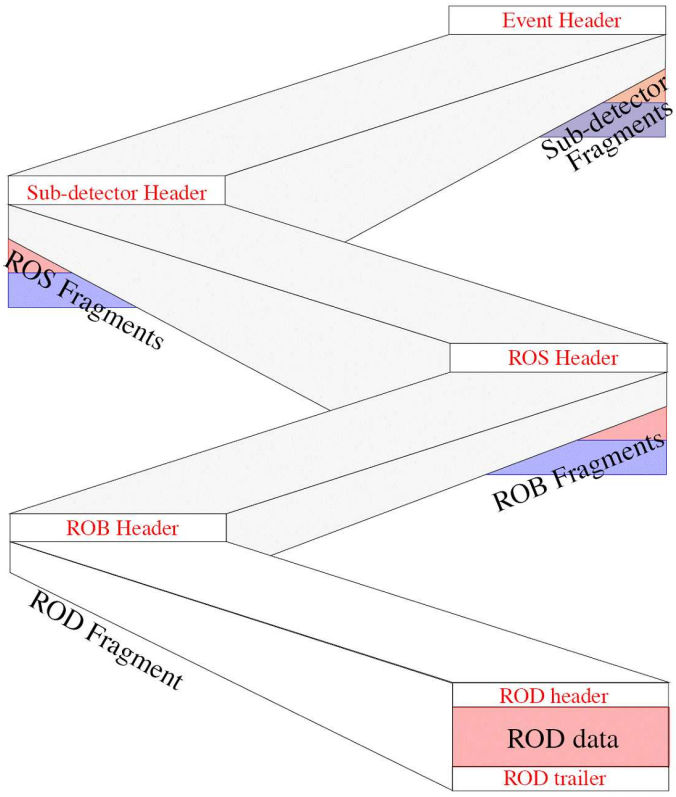

Figure 3.7: General event data format.

In the case of TileCal, 64 ROD fragments with the information from 4 modules each will cover the whole TileCal data. The ROD fragment data format is divided into 4 main blocks as Table 3.3 shows: Header, Data Elements, Status Elements and Trailer.

Table 3.3: ROD fragment data format in staging mode.

HEADER	Start of Header Marker
	Header size
	Format version number
	Source identifier
	Run number
	Extended Level 1 ID
	Bunch crossing ID
	Level 1 trigger type
	Detector event type
DATA ELEMENTS	Reco Fragment (type 0x2) #1
	Digitizer Fragment (type 0x0) #1
	Reco Fragment (type 0x2) #3
	Digitizer Fragment (type 0x0) #3
	MTag-MET Fragment (type 0x10) #1 #3
	Reco Fragment (type 0x2) #2
	Digitizer Fragment (type 0x0) #2
	Reco Fragment (type 0x2) #4
	Digitizer Fragment (type 0x0) #4
	MTag-MET Fragment (type 0x10) #2 #4
STATUS ELEMENTS	Status element 1
	...
	Status element n
TRAILER	Number of status elements
	Number of data elements
	Status Block Position

The Data elements block will contain an arbitrary number of different fragment types. This block is built by the DSPs. The DSP 1 builds part of the Header and the Data elements for 1 or 2 front-end boards (FEBs) depending on the working mode (full or staging). The DSP 2 builds the Data elements for 1 or 2 FEBs and the Status elements. Due to the ROD design, in staging mode the DSP 1 processes the data from ROD inputs #1 and #3 and the DSP 2 from ROD inputs #2 and #4. The first 2 words in the header and the whole trailer are built by the OC.

Table 3.3 shows the most general structure for the fragments in the Data elements for staging operation mode, as was used for cosmics runs (see Section 5.3). The output of the algorithms processed at the ROD DSP level is present in the ROD data format and available for LVL2. The fragments corresponding to the online algorithms (Reco and MTag-MET) may be present depending on the type of run and can be enabled/disabled at will. Similarly, Table 3.4 shows the ROD fragment structure for full operation mode.

Table 3.4: ROD fragment data format in full mode.

HEADER	Start of Header Marker
	Header size
	Format version number
	Source identifier
	Run number
	Extended Level 1 ID
	Bunch crossing ID
	Level 1 trigger type
	Detector event type
DATA ELEMENTS	Reco Fragment (type 0x2) #1
	Digitizer Fragment (type 0x0) #1
	MTag-MET Fragment (type 0x11) #1
	Reco Fragment (type 0x2) #2
	Digitizer Fragment (type 0x0) #2
	MTag-MET Fragment (type 0x11) #2
STATUS ELEMENTS	Status element 1
	...
	Status element n
TRAILER	Number of status elements
	Number of data elements
	Status Block Position

3.4.1 Header

The ROD header words are summarized below:

- **Start of Header Marker:** This marker indicates the start of a fragment header and is itself part of the header. Hence, it is the first word of a fragment. The value of this element will be unique for each type of fragment, but the structure will be identical. The Header Marker for the different fragment types are: Full Event fragment (0xaa1234aa), Sub-Detector fragment (0xbb1234bb), ROS fragment (0xcc1234cc), ROB fragment (0xdd1234dd) and ROD fragment (0xee1234ee).
- **Header size:** This element indicates the total size of the Header.
- **Format Version Number:** 32-bit integer number which gives the format version of the ROD fragment composed by the minor and major version number.
- **Source Identifier:** It consists of a sub-detector ID (detector partition) and Module ID.
- **Run Number:** 32-bit integer number which identifies uniquely the data run, including the type of run.
- **Extended Level 1 ID:** 32-bit word. It is formed by the 24-bit Level 1 ID and the 8-bit Event Counter Reset ID (ECRID) implemented in the ROD.
- **Bunch Crossing ID:** 12-bit word generated in the TTCrx.
- **Level 1 Trigger Type:** 8-bit word which contains the information sent by the LVL1 system about the event type. It is generated by the Central Trigger Processor (CTP). The remaining 24 bits are unused and set to zero.
- **Detector event type:** identifies the type of the event: a physics event (1), a laser event (2), a pedestal event (4) or a calibration event from the Charge Injection System (CIS) (8).

Table 3.5: ROD fragment header data format.

Start of Header Marker	0xee1234ee			
Header size	0x9			
Format version number	Major version number		Minor version number	
Source identifier	Reserved	Sub-detector ID	Module ID	
Run number	Run type	Sequence number within run type		
Extended Level 1 ID	ECRID	L1ID		
Bunch crossing ID	0x0000		0b	bb
Level 1 trigger type	0x000000			tt
Detector event type	Fragment Type Mask			TileEvent Type

3.4.2 Data Elements

The Data elements block will contain the physics data arranged in several fragments. Each of the fragments present in the Data elements contains a fragment header, a fragment size, a fragment identifier and the processed data. In TileCal, four types of fragment are currently being used, which are described in the following

subsections. The type of fragment is decoded together with the identification of the super-drawers whose data are contained in the fragment.

3.4.2.1 Digitizer Fragment (type 0x0)

The Digitizer fragment contains the raw data from one super-drawer, that is, the 10-bit samples taken each 25 ns in the digitizers from the PMT electronic pulses. Table 3.9 shows the Digitizer fragment data format for monogain physics runs and Table 3.10 for bigain calibration runs. The data words contain the digital sample information from 3 different channels and the word parity bit (P) as Table 3.8 shows.

The type of fragment and the super-drawer ID are stored in the fragment ID as shown in Table 3.6. The 4 bits reserved for the partition are set to 0x1 if the super-drawer belong to the LBC partion and 0x2 if belongs to the LBA partition. Similarly, super-drawers in the EBC and EBA partitions have a value of 0x3 and 0x4 in this field, respectively. The range for the super-drawer ID is from 0x00 (super-drawer #1) to 0x3f (super-drawer #64).

Table 3.6: Fragment ID format for types 0x0, 0x2 and 0x11.

empty	Frag type	Tile partition	super-drawer ID
bits 31:24	bits 23:16	bits 15:8	bits 7:0

The format of the TileDMU header is shown in Table 3.7. The information encoded in this word is the following:

Table 3.7: Format of the DMU header.

1	p	l	e	s	d	r	v	0	m	g	b
bit 31	bit 30	bits 29:26	bit 25	bit 24	bit 23	bit 22	bits 21:18	bit 17	bits 16:15	bits 14:12	bits 11:0

- **p:** Parity (odd).
- **l:** Derandomizer length (number of samples).
- **e:** Parity error. A parity error was detected from the memory in the last readout.
- **s:** SEstr Single Error Strobe received from the TTC.
- **d:** DEstr Double Error Strobe received from the TTC.
- **r:** Register parity. Parity from the registers in the chip.
- **v:** Variable parity. Parity from the variables in the chip.
- **m:** Mode. Indicates Normal mode (00), Calibration mode (01), Test mode (10) or Not used (11).
- **g:** High/low gain. Indicates high (1) or low (0) amplification from the 3-in-1 cards.
- **b:** Bunch Crossing.

Bits 17 and 31 are not used and set to 0 and 1 respectively.

Table 3.8: Digitizer fragment 32-bit data word format.

0 bit 31	P bit 30	Data channel 3 bits 29:20	Data channel 2 bits 19:10	Data channel 1 bits 9:0

As shown in Tables 3.9 and 3.10, 16 DMU blocks are present in the Digitizer fragment which corresponds to 48 channels. Although only 45 channels are present in long barrel super-drawers and 32 in extended barrel super-drawers, 16 DMU blocks are sent. The number of words in each block corresponds to the number of samples used to digitize the PMT pulses.

Table 3.9: Digitizer fragment for physics mode (1 gain).

Fragment header (0xff1234ff)
Fragment size (16×(n+2)+5)
Fragment ID
Header from **DMU1**
Data word, high/low gain **sample 1** from **DMU1**
Data word, high/low gain **sample 2** from **DMU1**
. . .
Data word, high/low gain **sample n** from **DMU1**
Trailer from **DMU1**: CRC word
Header from **DMU2**
Data word, high/low gain **sample 1** from **DMU2**
Data word, high/low gain **sample 2** from **DMU2**
. . .
Data word, high/low gain **sample n** from **DMU2**
Trailer from **DMU2**: CRC word
. . .
Header from **DMU16**
Data word, high/low gain **sample 1** from **DMU16**
Data word, high/low gain **sample 2** from **DMU16**
. . .
Data word, high/low gain **sample n** from **DMU16**
Trailer from **DMU16**: CRC word
DMU Chip mask word
Final Link CRC16

The last word in each DMU block contains the Cyclic Redundancy Check (CRC) value calculated in the front-

end for this piece of data.

The DMU Chip mask word is formed by 2 identical 16-bit halves. For long barrel modules its value is 0xffff (16 DMU chips present) and for extended barrel modules is 0x0fff (only 12 DMU chips present).

The Final Link CRC16 word is calculated over the whole fragment in the front-end. This quantity is calculated again inside the ROD and compared with the value received to verify the correct data transmission.

In calibration runs each DMU block contains the samples from both electronic chain gains separated by different headers.

Table 3.10: Digitizer fragment for calibration mode (2 gains).

Fragment header (0xff1234ff)
Fragment size ($16\times(2n+3)+5$)
Fragment ID
Header low gain from **DMU1**
Data word, low gain **sample 1** from **DMU1**
Data word, low gain **sample 2** from **DMU1**
...
Data word, low gain **sample n** from **DMU1**
Header high gain from **DMU1**
Data word, high gain **sample 1** from **DMU1**
Data word, high gain **sample 2** from **DMU1**
...
Data word, high gain **sample n** from **DMU1**
Trailer from **DMU1**: CRC word
...
Header low gain from **DMU16**
Data word, low gain **sample 1** from **DMU16**
Data word, low gain **sample 2** from **DMU16**
...
Data word, low gain **sample n** from **DMU16**
Header high gain from **DMU16**
Data word, high gain **sample 1** from **DMU16**
Data word, high gain **sample 2** from **DMU16**
...
Data word, high gain **sample n** from **DMU16**
Trailer from **DMU16**: CRC word
DMU Chip mask word
Final Link CRC16

3.4.2.2 Reco Fragment (type 0x2)

The Reco fragment contains the reconstructed energy, time and quality factor using the Optimal Filtering algorithm at the DSP level. Tables 3.11 and 3.12 show the Reco fragment data format for monogain physics runs and bigain calibration runs respectively. Table 3.13 shows the bit field of the words in these fragments. The fragment ID has the same format as in the digitizer fragment (Table 3.6).

Table 3.11: Reco fragment for monogain physics runs.

Fragment header (0xff1234ff)			
Fragment size (0x33)			
Fragment ID			
Gain	Energy ch1	Time ch1	Q factor ch1
Gain	Energy ch2	Time ch2	Q factor ch2
...			
Gain	Energy ch48	Time ch48	Q factor ch48

Table 3.12: Reco fragment for bigain calibration runs.

Fragment header (0xff1234ff)			
Fragment size (0x63)			
Fragment ID			
0	Energy ch1 low gain	Time ch1 low gain	Q factor ch1 low gain
0	Energy ch2 low gain	Time ch2 low gain	Q factor ch2 low gain
0	Energy ch3 low gain	Time ch3 low gain	Q factor ch3 low gain
1	Energy ch1 high gain	Time ch1 high gain	Q factor ch1 high gain
1	Energy ch2 high gain	Time ch2 high gain	Q factor ch2 high gain
1	Energy ch3 high gain	Time ch3 high gain	Q factor ch3 high gain
0	Energy ch4 low gain	Time ch4 low gain	Q factor ch4 low gain
...			
1	Energy ch48 high gain	Time ch48 high gain	Q factor ch48 high gain

Table 3.13: OF bit fields.

Gain	Energy (ADC counts)	Time (ns)	Q factor
bit 31	bits 30:16	bits 15:4	bits 3:0

3.4.2.3 MTag-MET Fragments (types 0x10 and 0x11)

The MTag-MET fragment contains the results of the Muon Tagging and Missing E_{T} algorithms processed at the DSPs. When the ROD is working in staging mode, the MTag-MET information will proceed from two adjacent super-drawers processed by the same DSP (see Table 3.15). This fragment is known as type 0x10 and the fragment ID encodes the identification of two super-drawers, as shown in Table 3.14.

Table 3.14: Fragment ID format for MTag-MET fragment type 0x10.

empty	Frag type	Tile partition	super-drawer #2 ID	super-drawer #1 ID
bits 31:24	bits 23:16	bits 15:12	bits 11:6	bits 5:0

Table 3.15: MTag-MET fragment in staging mode (type 0x10).

Fragment header (0xff1234ff)			
Fragment size (0x7)			
Fragment ID			
0xc	empty	N_μ found in super-drawer #1	8 bits for towers
0xc	empty	N_μ found in super-drawer #2	8 bits for towers
MET super-drawer #1			
MET super-drawer #2			

On the other hand, when the ROD is working in full mode, the MTag-MET fragment will contain information from one super-drawer (see Table 3.16). This fragment is known as type 0x11 and the fragment ID has the format shown in Table 3.6.

Table 3.16: MTag-MET fragment in full mode (type 0x11).

Fragment header (0xff1234ff)			
Fragment size (0x5)			
Fragment ID			
0xc	empty	N_μ found in super-drawer	8 bits for towers
MET super-drawer			

For LBA and LBC modules, as shown in Table 3.17, the 8 less significant bits contain the information about the towers where the muons are searched. If a muon is tagged, the corresponding bit is set to 1, otherwise to 0. The next 4 bits contain the total number of muons found in this super-drawer. There are 16 empty bits and the last 4 are set to 0xc just for easy visualization. The format for EBA and EBC, shown in Table 3.18, is similar but with information from only 4 towers. The MET word format is not defined yet.

Table 3.17: MTag bit fields for the long barrel.

0xc	empty	N_μ found	8 bits for LB towers
bits 31:28	bits 27:12	bits 11:8	bits 7:0

Table 3.18: MTag bit fields for the extended barrel.

0xc	empty	N_μ found	4 bits for EB towers
bits 31:28	bits 27:12	bits 11:8	bits 7:0

3.4.3 Status Elements

The Status elements are 32-bit integers. The first Status element will be divided into two 2-byte fields labeled Generic and Specific, as Table 3.19 shows. The values and error conditions indicated by the Generic field are the same for all fragments, while the values and error conditions indicated by the Specific field have meanings specific to the fragment. A non-zero value of this element indicates that the event fragment is corrupted. The information conveyed by the status element only refers to the fragment of which it is an element.

Table 3.19: Status element bit fields.

Specific	Generic
bits 31:16	bits 15:0

3.4.4 Trailer

The Trailer marks the end of the ROD fragment. It contains the following 32-bit integers:

- **Number of status elements:** indicates the number of 32-bit words in the status block. A value of zero indicates that there are no Status elements and therefore there are no known errors associated to the ROD fragment.
- **Number of data elements:** indicates the number of 32-bit words in the data block.
- **Status block position:** defines the relative order of the Data and Status elements. A value of zero indicates that the status block precedes the data block and a value of one indicates that the status block follows the data block.

Chapter 4

Muon Tagging Algorithm Offline Performance

4.1 Muon production at LHC

The rate of muons arriving to the muon spectrometer in ATLAS has been extensively studied due to its implications not only in the muon system, but also in the trigger and calorimeter systems.

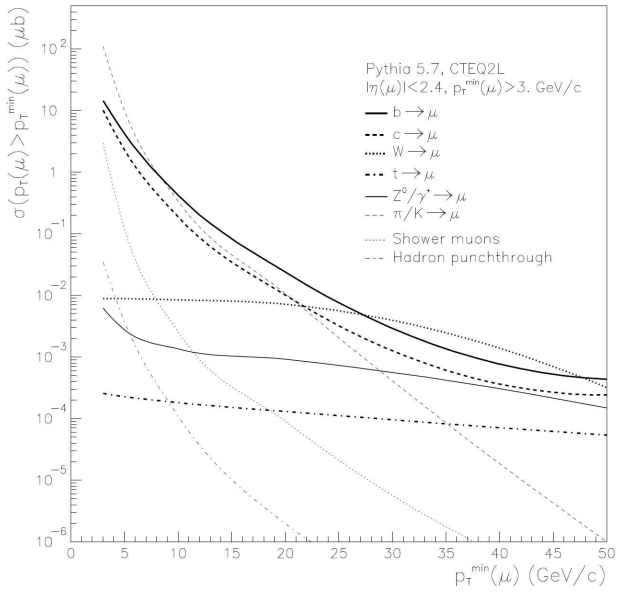

Figure 4.1: Integrated cross section for inclusive muon production at LHC as a function of the p_{T} threshold in the pseudorapidity range $|\eta| < 2.4$.

The muon flux arriving to the spectrometer has several sources (semi-leptonic decays of heavy particles, Drell-Yan production, hadron decays, etc.) and the muon energy varies over a large interval from a few GeV

(B-physics) to a few TeV (new physics). Figure 4.1 shows the integrated cross section for muon production at LHC. The muon rate is dominated by π/K decays up to $p_{\mathrm{T}} \simeq 8$ GeV and by $\mathrm{b\overline{b}}$ decays from 8 GeV to 30 GeV, with sizeable contributions by W decays at larger p_{T} values. Hadron punch-through and shower leakage from the calorimeters are negligible.

In particular, di-muon rates in ATLAS have been estimated through PYTHIA simulations [27]. Figure 4.2 shows the expected integral production rate at low luminosity for $\mathrm{b\overline{b}}$, $\mathrm{c\overline{c}}$ and π/K with one muon which can be triggered by LVL1 (with p_{T}>6 GeV and $|\eta| < 2.4$) as a function of the transverse momentum of the second muon with $|\eta| < 1.4$ (TileCal coverage). As shown in the figure, the dominant process is the $\mathrm{b\overline{b}}$ for a p_{T} range of the second muon above 5 GeV.

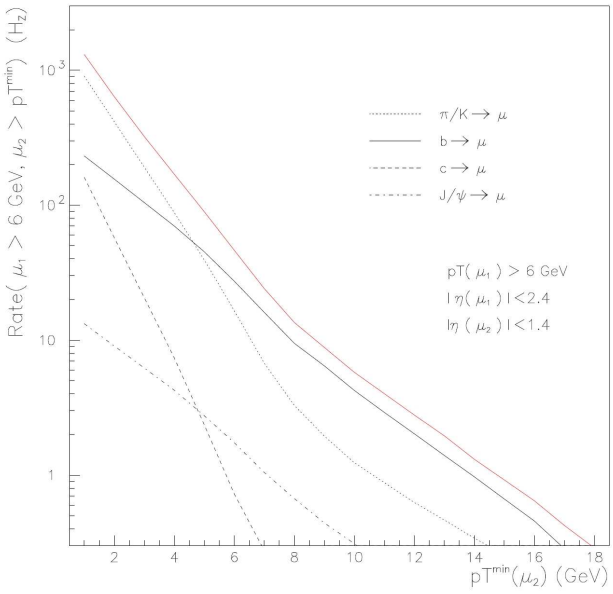

Figure 4.2: Expected di-muon production rates at LHC at low luminosity ($L = 10^{33}$ cm^{-1}s^{-2}), with the contributions from the various channels and the total rate from [27]. The pseudorapidity range for the first muon is $|\eta(\mu_1)| \leq 2.4$ and $|\eta(\mu_2)| \leq 1.4$ for the second muon, corresponding to the coverage of the muon spectrometer and TileCal, respectively.

Previous studies on the performance of the algorithm [27] show that the estimated rate for the MTag algorithm used at LVL2 is 860 Hz, with only 200 Hz due to fake tags. As the total rate is compatible with the total LVL2 rate (1 kHz), the implementation and usage of this algorithm at LVL2 is feasible.

However, the timing required at LVL2 for a low p_{T} muon tagging algorithm which makes use of the calculation of the cell energies in the whole TileCal is 30 ms [30], when the total latency available is only 10 ms. In consequence, the implementation of the algorithm at the ROD level may save CPU time at LVL2 so that its usage were possible at ATLAS.

4.2 Monte Carlo Data Analysis

The performance of the Muon Tagging algorithm described in Section 3.3 has been extensively tested using simulated data with several Monte Carlo samples containing single muons and some other B-physics processes.

In first place, the acceptance cone to successfully tag muons is defined from single muon data. The single muon sample is also used to compute the algorithm efficiencies. With $b\overline{b}$ sample (the dominant process at LHC) the fraction of fakes and efficiencies are studied. Finally a B-physics sample with a dedicated channel is also used to furthermore study the efficiency of the algorithm.

All the data used in this section were simulated in the ATLAS Data Challenges project and reconstructed using the Athena framework, through the use of ROOT[1] [31] files. These ROOT files were analyzed offline with the same implementation of the algorithm as used online in the DSP, but taking as input the cell energy reconstructed offline using the Fit method instead of the online calculation in the DSP using the Optimal Filtering algorithm.

4.2.1 Acceptance cone definition

Figure 4.3 shows the energy deposition per cell in TileCal for a typical single muon event. For each of the three layers of the calorimeter, the energy deposition is important only in one cell per layer (or two cells at most), with noise fluctuations in the rest of the cells. The cells with significative energy deposition in each layer are aligned in η and ϕ following the track of the muon.

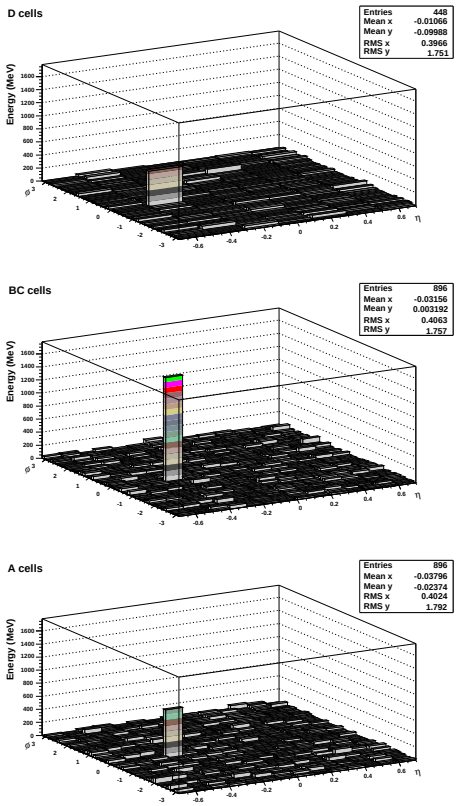

Figure 4.3: Cell energy deposition for a single muon Monte Carlo event as a function of η and ϕ for TileCal layer A (bottom), BC (middle) and D (top).

[1]ROOT is an object-oriented data analysis framework developed at CERN as a replacement for PAW (which is based in FORTRAN).

In order to objectively define whether a muon tagged by the algorithm actually corresponds to a muon generated in the Monte Carlo, an acceptance cone around the tagged muon is defined. Information on the particles involved in the simulation (type of particle, momentum, η and ϕ coordinates, etc.) is available in the Truth section of the reconstructed ROOT file. This way, when a muon is tagged we say that is a successful tag if in the simulation a muon has been generated inside the acceptance cone. Otherwise we have a fake tag.

The dimensions of the cone are obtained from single muon data using the distributions of the difference between the coordinates of the generated and tagged muons for both η and ϕ. As the ϕ coordinate is affected by the solenoid magnetic field, the following correction, expressed in module units ($2\pi/64 = 0.098$ rad), must be applied [25]:

$$\phi = \phi_{\text{gen}} \pm \frac{5.45}{p_{\text{T}}} \mp 0.49 \tag{4.1}$$

In our case, a sample with more than 15 000 tagged muons with several momentum values from 3 to 30 GeV was used. Figure 4.4 shows the distributions of the difference between the generated muon coordinates and the tagged muon coordinates. In both η and ϕ, the distributions are Gaussian-like and centered close to zero. The dimensions of the acceptance cone have been set to be 4σ of the distributions shown in Figure 4.4. With the results obtained, $\sigma_\eta = 0.04$ and $\sigma_\phi = 0.03$, we define a cone of $\Delta\eta \times \Delta\phi = 0.16 \times 0.12$.

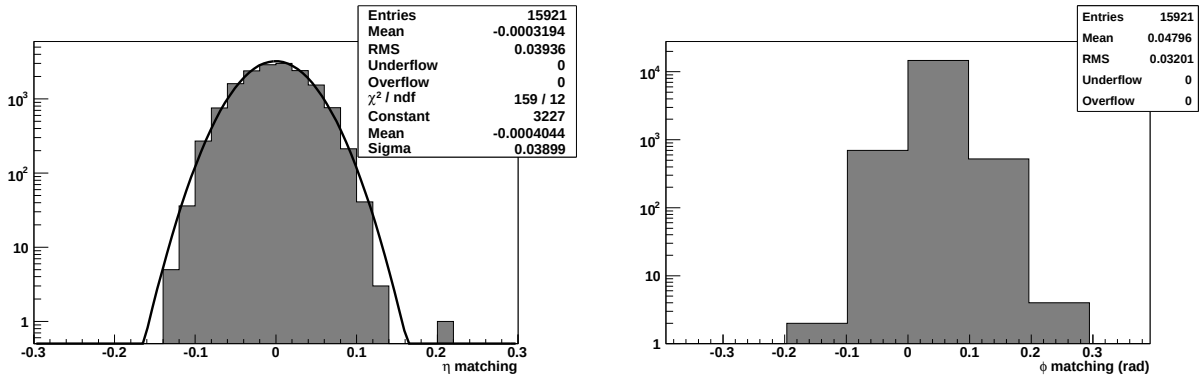

(a) Residuals distribution in η.

(b) Residuals distribution in ϕ.

Figure 4.4: Distribution of residuals (difference between the coordinates of the tagged and generated muons).

4.2.2 Results for single muon events

Figure 4.5 shows the η and ϕ distributions for the generated muons and the muons successfully tagged offline in the case of single muon Monte Carlo data. The binning on the histograms is set to be one tower ($\Delta\eta = 0.1$) and one module ($\Delta\phi = 2\pi/64$), respectively. The distributions for the generated muons are uniform in both coordinates.

For the tagged muons, the η distribution has big gaps at $0.8 < |\eta| < 1.1$ corresponding to the physical gap between TileCal LB and EB where the tower cells data are not processed by the same DSP and the MTag algorithm cannot be applied. This gap is also the cause of the smaller number of muons tagged in the $0.7 < |\eta| < 0.8$ tower. At low values of η a decrease in the number of muons tagged is observed due to larger spread

in the muon energy deposition caused by large sampling iron/scintillator ratio variation. The ϕ distribution for the tagged muons is uniform, as expected.

Thus, the μ-tagging efficiency ϵ is defined as the fraction of the generated muons N_{gen} which have been successfully tagged N_{tag}:

$$\epsilon = \frac{N_{\text{tag}}}{N_{\text{gen}}} \tag{4.2}$$

Similarly, the fraction of fakes f is defined as the fraction of the tagged muons which do not correspond to actual muons in the simulation:

$$f = \frac{N_{\text{mistag}}}{N_{\text{tag}} + N_{\text{mistag}}} \tag{4.3}$$

In the above expressions N_{tag} is the number of tagged muons with an associated muon at generation level and N_{mistag} is the number of tagged muons without an associated muon.

In all cases, the error bars have been calculated using binomial statistics with the following expression:

$$\sigma(\epsilon) = \frac{1}{N_{\text{gen}}}\sqrt{N_{\text{tag}}\left(1 - \frac{N_{\text{tag}}}{N_{\text{gen}}}\right)} \tag{4.4}$$

Figure 4.6 shows the efficiency as a function of η and ϕ averaged over p_{T}. The efficiency is low for values of η close to the origin and directly zero in the LB-EB gap. In the region $0.4 < |\eta| < 0.7$ the efficiency is larger than 90%. The efficiency is uniform as a function of ϕ with values around 75%. Note that for the averaged values in Figure 4.6 (b), the muons generated in the region $0.8 < |\eta| < 1.1$ have not been considered, as the muon tagging algorithm cannot be applied there.

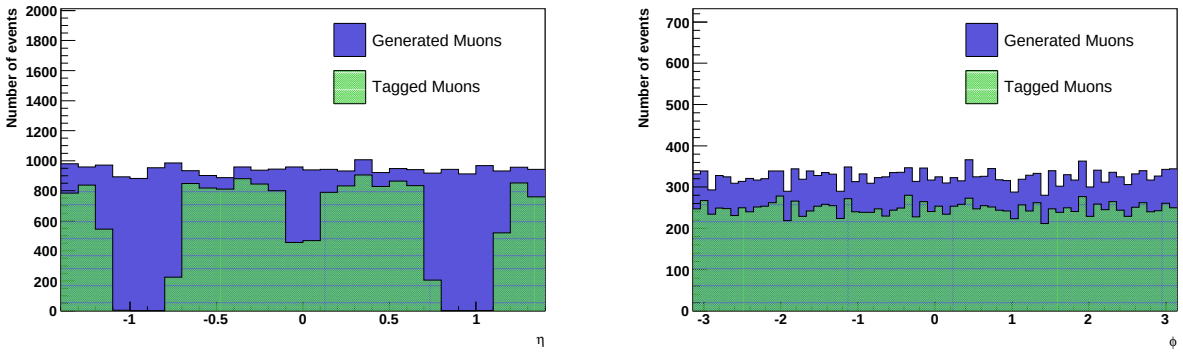

(a) η Distribution.

(b) ϕ Distribution.

Figure 4.5: Distributions of η and ϕ coordinates for single muon events. In blue, the distributions for all the generated muons and in green for the muons successfully tagged.

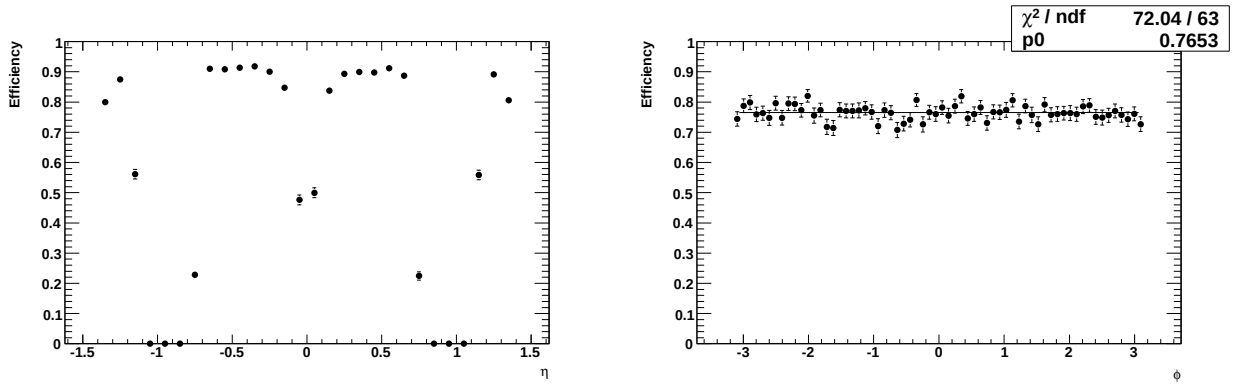

(a) Efficiency as a function of η.

(b) Efficiency as a function of ϕ. Towers in the LB-EB gap are removed from the average.

Figure 4.6: Efficiencies as a function of the η and ϕ coordinates for single muon events averaged over p_{T}.

4.2.3 Results for $\mathrm{b\overline{b}} \rightarrow \mu(6)\mathrm{X}$ events

The first set of Monte Carlo data to be studied as a part of the physics processes was the inclusive channel $\mathrm{b\overline{b}} \rightarrow \mu(6)\mathrm{X}$, in which a $\mathrm{b\overline{b}}$ pair is created in the pp collision and with at least one muon with $p_{\mathrm{T}} > 6$ GeV present in the final state. These final state muons come from semileptonic decays of B hadrons. This is the dominant source of inclusive muon production at LHC over the whole p_{T} range as seen in Figures 4.1 and 4.2. The sample used contained 40 000 events and, as in the previous case, the Monte Carlo Truth information was used to verify the muons tagged by the MTag algorithm.

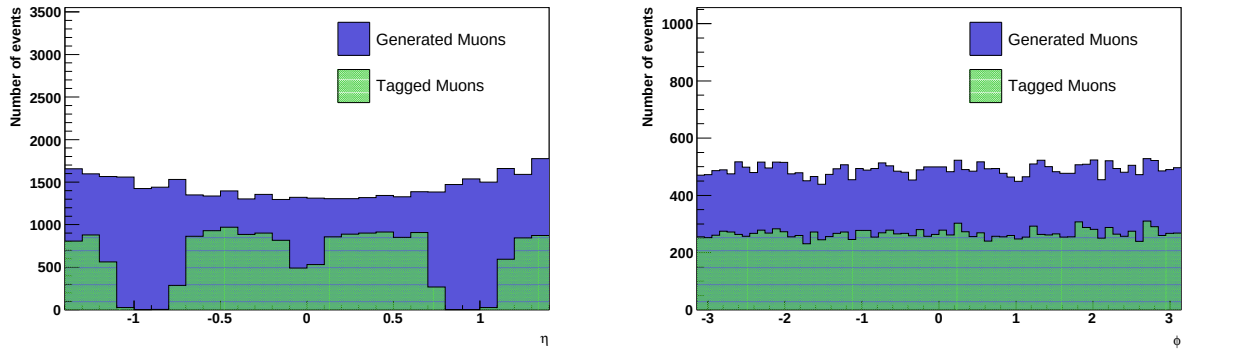

(a) η Distribution.

(b) ϕ Distribution.

Figure 4.7: Number of events as a function of η and ϕ for $\mathrm{b\overline{b}} \rightarrow \mu(6)\mathrm{X}$ events. In blue, the distributions for all the generated muons and in green for the muons successfully tagged.

Figure 4.7 shows the distribution in η and ϕ for the generated muons and the muons successfully tagged. In this case, at high values of η more muons are present due to the kinematics of the process. Regarding the

tagged muons, we have the same behaviour as seen for the single muon sample: a uniform distribution in ϕ, no tags in the LB-EB gap region and less muons tagged in the $|\eta| \sim 0$ region.

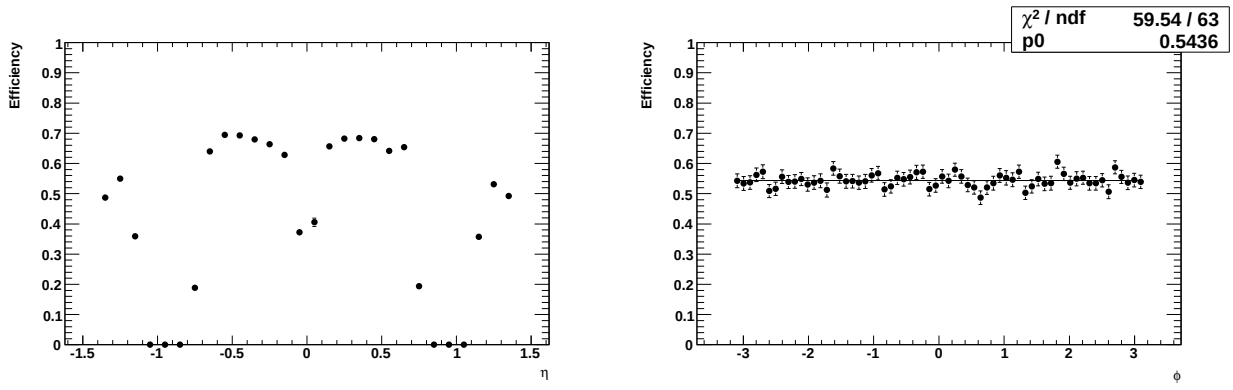

(a) Efficiency as a function of η.

(b) Efficiency as a function of ϕ. Towers in the LB-EB gap are removed from the average.

Figure 4.8: Efficiencies as a function of the η and ϕ coordinates for $\mathrm{b\overline{b}} \rightarrow \mu(6)\mathrm{X}$ events.

The values of the efficiency as a function of η are shown in Figure 4.8 (a). The same qualitative behaviour is observed as for the single muon sample. The efficiency as a function of the ϕ coordinate, averaged on η and p_{T}, is shown in Figure 4.8 (b). The plot shows a uniform distribution with efficiency values around 55%.

The reason of this low efficiency for this sample as compared to the single muons is the different p_{T} spectrum for the muons to be tagged. The tag efficiency as a function of p_{T} (averaged over η and ϕ) is shown in Figure 4.9. At low p_{T} values the efficency decreases considerably with an acceptable 40% at 2 GeV but very poor at 1 GeV. As discussed in Section 3.3.1, the mean energy loss by muons with p_{T} of 1 GeV to 200 GeV is $\sim$2.5 GeV, so most of the muons with $p_{\mathrm{T}} < 2$ GeV are actually stopped in TileCal. However, in the 3 GeV $< p_{\mathrm{T}} <$ 15 GeV range the efficiencies obtained are almost constant around 75-80%, that is, consistent with the results obtained with the single muon sample.

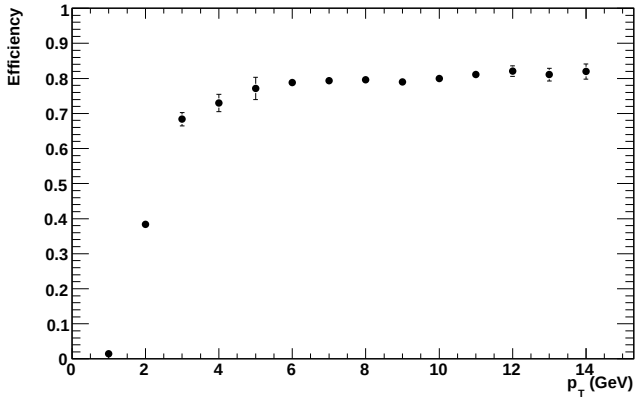

Figure 4.9: Efficiency as a function of p_{T} for $\mathrm{b\overline{b}} \rightarrow \mu(6)\mathrm{X}$ events.

The values obtained for the fraction of fakes have also been studied for this sample. Figure 4.10 shows the fraction of fakes as a function of the η and ϕ coordinates. On average, the fraction of fakes are at the $\sim$5% level, with slightly higher values for the Extended Barrel towers.

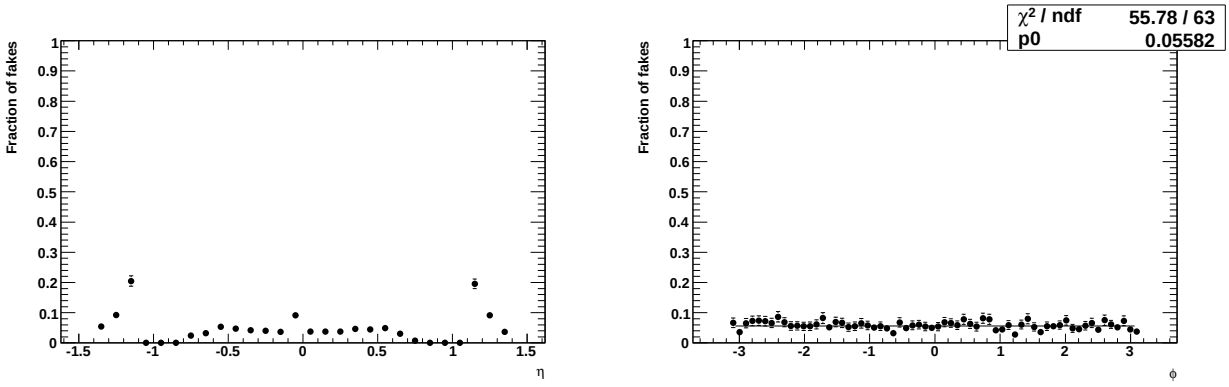

(a) Fraction of fakes as a function of η.

(b) Fraction of fakes as a function of ϕ.

Figure 4.10: Fraction of fakes as a function of the η and ϕ coordinates for $b\overline{b} \rightarrow \mu(6)X$ events.

4.2.4 Results for $B_s^0 \rightarrow J/\psi(\mu\mu)\phi$ events

A sample of 30 000 events of the $B_s^0 \rightarrow J/\psi(\mu 6 \mu 3)\phi(KK)$ decay channel, used in B-physics, has been processed using the MTag algorithm. In this channel the J/ψ particle decays to 2 muons, one with $p_T > 6$ GeV and the other with $p_T > 3$ GeV. The results obtained for the distribution in η and ϕ for the muons generated and successfully tagged are shown in Figure 4.11.

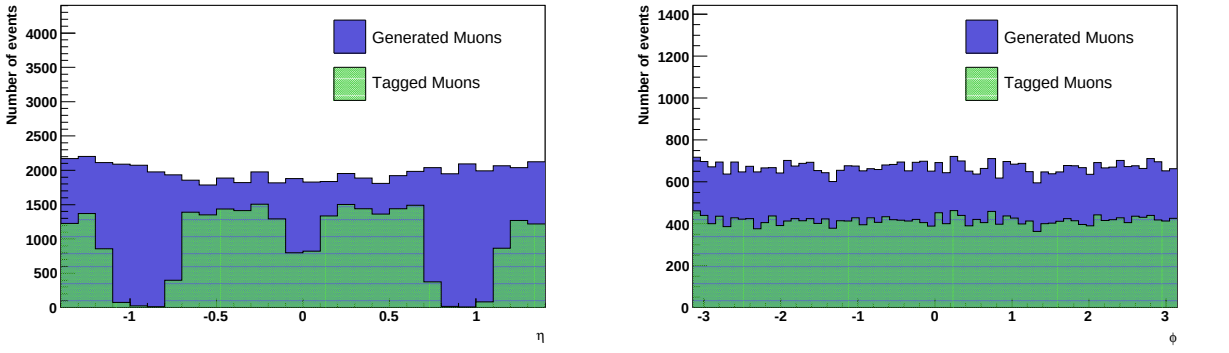

(a) η Distribution.

(b) ϕ Distribution.

Figure 4.11: Distributions of η and ϕ coordinates for $B_s^0 \rightarrow J/\psi(\mu\mu)\phi$ events. In blue, the distributions for all the generated muons and in green for the muons successfully tagged.

Figure 4.12 shows the efficiencies as a function of η and ϕ. The distributions and the average values obtained are very similar to those obtained for the $b\overline{b} \rightarrow \mu(6)X$ sample, with an efficiency above 70% in the barrel and an average value of ∼60%.

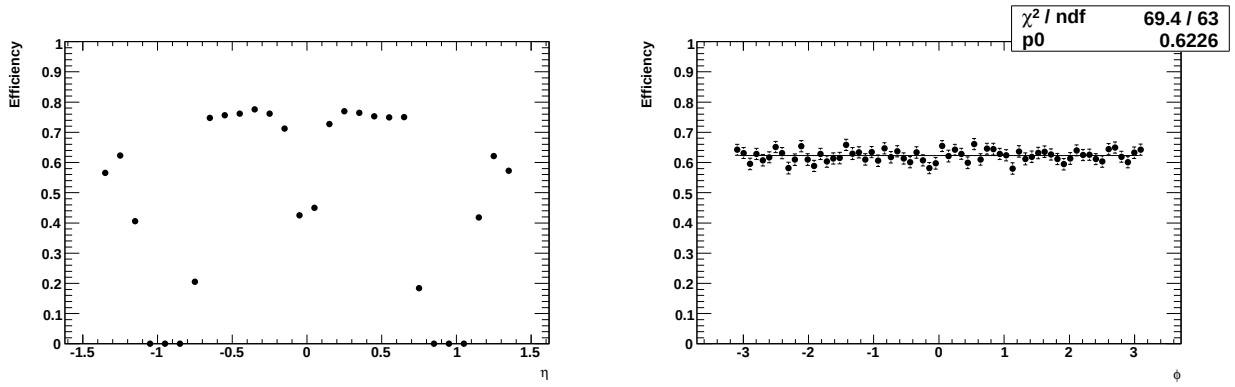

(a) Efficiency as a function of η.

(b) Efficiency as a function of ϕ. Towers in the LB-EB gap are removed from the average.

Figure 4.12: Efficiencies as a function of the η and ϕ coordinates for $B_s^0 \rightarrow J/\psi(\mu\mu)\phi$ events.

The values of the efficiency as a function of the p_T are shown in Figure 4.13. Similarly to the results obtained for $b\overline{b} \rightarrow \mu(6)X$, a 75-80% efficiency is observed in the 3 GeV $< p_T <$ 15 GeV region, with much smaller efficiencies for muon momentum values below 2 GeV.

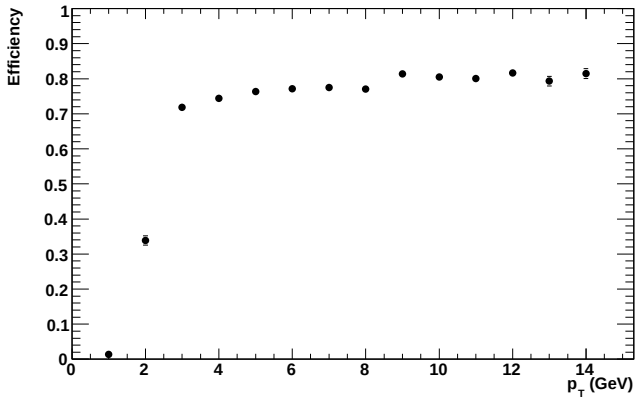

Figure 4.13: Efficiency as a function of p_T for $B_s^0 \rightarrow J/\psi(\mu\mu)\phi$ events.

The distributions obtained for the fraction of fakes are shown in Figure 4.14 with a 6% average value and with slightly higher values in the EB towers.

Another interesting study to perform is to compare the efficiency and fraction of fakes as a funtion of the lower threshold applied in the MTag algorithm. When increasing this threshold, less noise events are tagged as muons and, in consequence, the fraction of fakes decreases. However, muon events with low energy deposition would not give a positive tag, decreasing the algorithm efficiency as well.

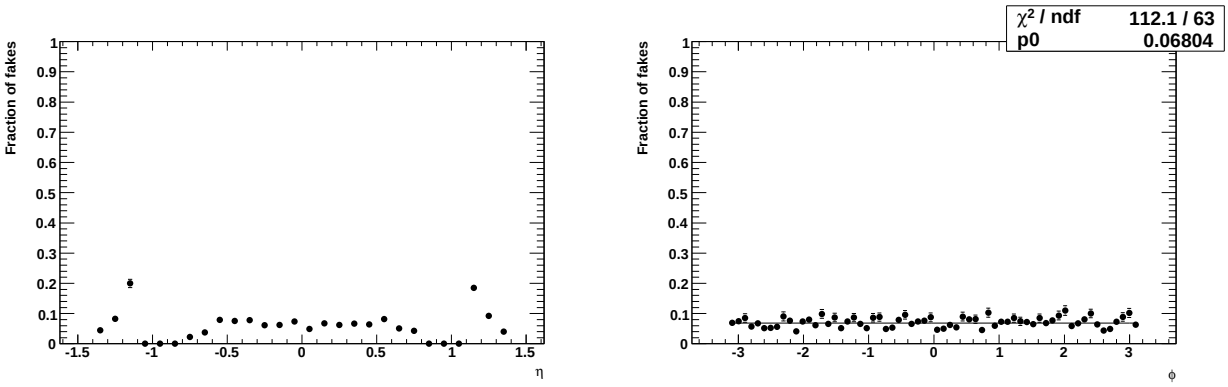

(a) Fraction of fakes as a function of η.

(b) Fraction of fakes as a function of ϕ.

Figure 4.14: Fraction of fakes as a function of the η and ϕ coordinates for $B_s^0 \rightarrow J/\psi(\mu\mu)\phi$ events.

Figure 4.15 shows the values of the MTag efficiency as a function of the fraction of fakes for the $B_s^0 \rightarrow J/\psi(\mu\mu)\phi$ sample by varying the lower threshold from 60 to 450 MeV. When the fraction of fakes is reduced below 4% the efficiency decreases to ∼40% (for a 390 MeV lower threshold value) and, on the contrary, when the average efficiency is above 80%, the fraction of fakes increases to ∼8% (when using a lower threshold value of 90 MeV).

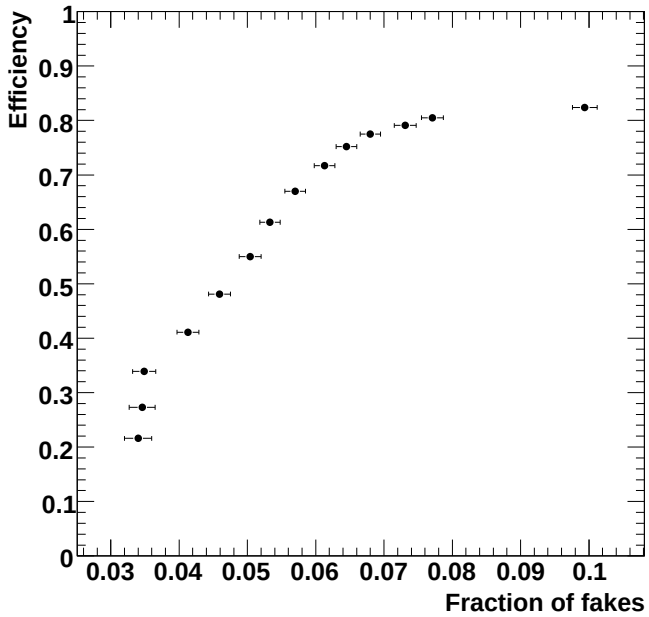

Figure 4.15: Efficiency as a function of the fraction of fakes for $B_s^0 \rightarrow J/\psi(\mu\mu)\phi$ events obtained by varying the lower energy threshold for the cell energy deposition from 60 to 450 MeV in steps of 30 MeV.

From this data, one can conclude that the default lower threshold used for the offline performance studies with Monte Carlo data (150 MeV) is a good compromise to obtain high efficiencies and low fraction of fakes in the final results.

As a conclusion of these results obtained with Monte Carlo data, the MTag algorithm has proved to be very useful in the $p_{\mathrm{T}} \geq 3$ GeV region, with good efficiency and low fraction of fakes. Furthermore, the infomation provided by this algorithm will cover with high efficiency a momentum range where the Muon Spectrometer is not efficient ($p_{\mathrm{T}} \leq 6$ GeV). In consequence, the MTag algorithm will tag muons which cannot be triggered at LVL1, and this feature can be used to enhance the performance of the ATLAS experiment in channels which involve low p_{T} muons.

For instance, in the $\mathrm{B_s^0} \rightarrow \mathrm{J}/\psi(\mu\mu)\phi$ channel used here and also in the $\mathrm{B_d^0} \rightarrow \mathrm{J}/\psi\,\mathrm{K_s^0}$ channel one of the muons in the $\mathrm{J}/\psi \rightarrow \mu\mu$ decay has high momentum ($p_{\mathrm{T}} \geq 6$ GeV) and will be triggered by LVL1 trigger. The second muon, which has lower momentum may not be reconstructed and the characteristic di-muon signature from the J/ψ would not be seen. The MTag algorithm used in the ROD will be applied to all the events selected by LVL1. These low p_{T} muons will be tagged and the information sent to LVL2 for triggering this type of events.

Chapter 5

Muon Tagging Algorithm Online Performance

Apart from the offline performance of the MTag algorithm studied with Monte Carlo data, it is essential to test the behaviour of the algorithm once implemented in the DSP core. This chapter is devoted to the performance in laboratory tests with injected data and in the TileCal commissioning, where the first ATLAS real data have been taken using cosmic muons. This way, the algorithm can be tested in an environment with final front-end and back-end electronics, integrated in the full TDAQ software and working in real conditions during the acquisition of physics cosmics run data.

5.1 TileCal Installation and Commissioning

During 2005 and 2006, TileCal has been fully assembled in the underground experimental hall UX15 (see Figure 5.1). The main objectives of the commissioning phase of the experiment are the integration of all the hardware and software elements and the test of the whole system in a setup close to the final one.

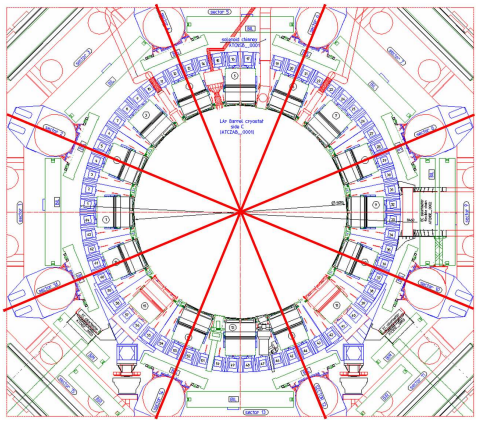

Figure 5.1: Scheme of TileCal in UX15. Sector division and module disposition and numbering are shown.

A series of correlated operations must be performed in order to make the calorimeter fully operational in terms of services (power and trigger cabling, cooling, read out and trigger fibers), low and high voltage, control and monitoring systems, calibration systems, etc. Alignment and timing between the different detector systems also take place in this phase of the experiment, as well as the demonstration of the performance levels in terms of noise and physics signals.

As for the RODs, in the final configuration 32 ROD modules (with their corresponding TMs) will be installed in USA15 (ATLAS electronics cavern) to read out the data coming from the TileCal modules. These modules will be installed in 4 separate ROD crates, each one meant to read data from one of the 4 DAQ partitions (LBA, LBC, EBA and EBC). Figure 5.2 shows a scheme of the 4 ROD crates together with the 4 crates in which the TTC modules will be placed. By summer 2006, 3 of the crates were already equipped with RODs.

At software level, the RODs were integrated in the general ATLAS framework for data acquisition and online tasks: TDAQ (Trigger and Data Acquisition). This framework is responsible for the experiment control, including run control, configuration of the trigger and data acquisition and the management of the data taking partitions. TDAQ also includes an online monitoring infrastructure and an Interactive Graphical User Interface (IGUI) for control and configuration of the system. Specific IGUI panels and ROD Crate DAQ (RCD) applications have been developed to configure and control the RODs and related modules [32].

Before the installation and integration of the RODs, another data acquisition system called MobiDAQ was used. The idea behind this system was to have a mobile DAQ system for the simultaneous readout of more than one super-drawer, for tests either in surface or in the pit. MobiDAQ was based on the use of ROD emulators (RCCs equipped with ODIN cards), and its main limitation was that it could only read out up to 8 super-drawers at a time, clearly insufficient for TileCal commissioning.

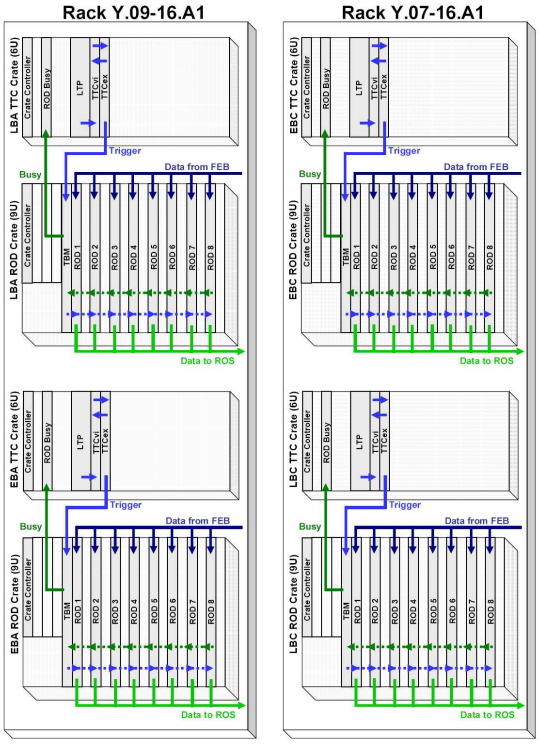

Figure 5.2: Scheme of the 2 racks which hold the ROD and TTC crates in USA15. Note the 4 ROD crates with their modules and the communication lines.

In order to have the modules and their electronics commissioned, tests which involve data acquisition are performed in all the super-drawers using the RODs. Furthermore, several DAQ runs are taken using the RODs for module certification. The following types of runs are used:

- **Pedestals:** The aim of these runs is to study the noise per channel and the coherence between channels.
- **CIS mono:** Here the response to pulses of injected charge is studied in terms of stability of response and noise.
- **CIS scan:** In this case a wide range of pulse heights are injected, making possible to find stuck bits in the ADC and the count/pC calibration constants.
- **LED:** Light is applied to the PMTs to study its functionality and check the laser fibers and the timing.
- **Physics:** A fifth run type, not related with module validation, is reserved for runs taken for cosmics with proper trigger configuration.

All the information about the runs taken in the TileCal commissioning is stored in an electronic logbook, which can be browsed in this address:

`http://pcata007.cern.ch/elog/`

During commissioning, a program of cosmic rays data acquisition has been planned for TileCal standalone running and in combination with other ATLAS subdetectors (LAr and muon spectrometer). In the standalone runs, the trigger was given by TileCal itself without any scintillator, using custom coincidence boards which take as input the analog sum of the trigger tower adders (Section 2.5.2) from 12 super-drawers. These trigger boards have two operation modes: single tower trigger and back-to-back tower trigger. In the single tower mode, a trigger is sent if the total energy deposited in a tower is greater than a given threshold. In the back-to-back mode, a trigger is sent only if the energy deposited in a tower and in its geometrically opposite is larger than a configurable threshold, selecting events where the particles pass close to the interaction point. Figure 5.3 shows graphically an example of a back-to-back tower trigger event.

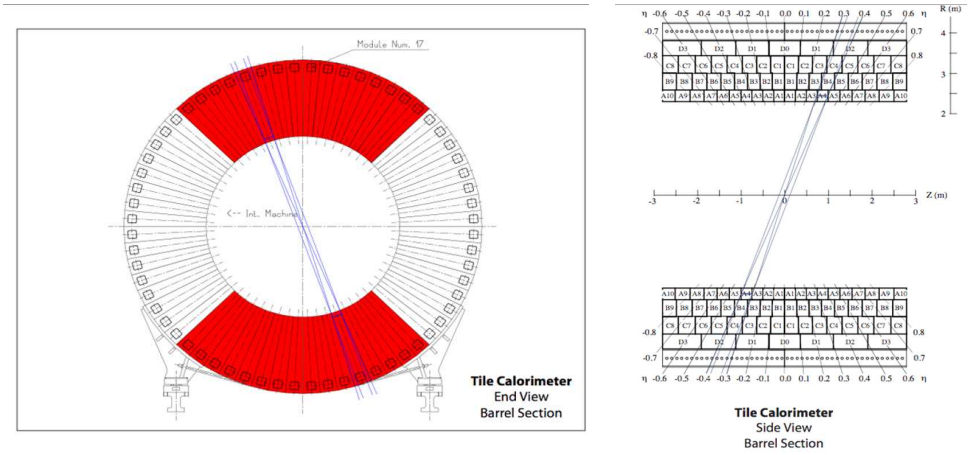

(a) View in the xy plane.

(b) View in the yz plane.

Figure 5.3: Back-to-back cosmic event in TileCal.

Simulations show that the expected trigger rate in TileCal is ∼1 Hz [33]. However, the complete picture is quite difficult, as the rate of cosmic muons entering the ATLAS cavern is much bigger and they have a wide spectrum in energy and incident angle. For instance, Figure 5.4 shows the tracks of the muons entering the ATLAS cavern in 0.01 seconds using a Geant3 simulation. Even worse, the muons can be scattered inside the detectors or in the rock above, making the analysis even more difficult [33].

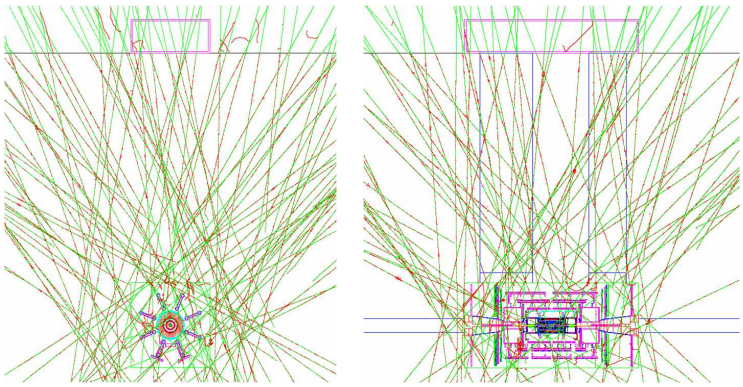

(a) Two-dimensional xy view. (b) Two-dimensional yz view.

Figure 5.4: Simulation of the cosmic muons entering the ATLAS cavern during a time interval of 0.01 s.

5.2 Performance tests and algorithm validation

5.2.1 ROD laboratory setup

In order to test the MTag algorithm performance inside the ROD DSPs in a controlled environment, a setup with a fully functional system was used in the TileCal-Valencia group laboratory at CERN. One production ROD, together with its TM and a TBM were placed in a 9U crate controlled by a RCC. A 6U OMB prototype working in injection mode was used as data source. Dedicated software applications were written to select specific events to be injected to the ROD. This way, one can inject known data to the ROD and check their processing in the DSP.

The trigger signals were configured using a TTCvi module [34] and a NIM crate equipped with dual timer modules. Specific PCI readout cards (FILAR [35] and ROBIN [36]) placed in a computer were used to store the data transmitted from the system.

5.2.2 Results from injected data

From the files recorded in June 2005 cosmics data taking period, run 1109 (taken with a single tower trigger) was selected for these tests due to its high statistics (60 000 events) and good behaviour in terms of noise. Raw digitizer data from all the events in the run for selected modules were injected with the OMB to the ROD and processed using the OF1i1 energy reconstruction and MTag algorithms online in the DSP. The following subsections show the results obtained in this study.

5.2.2.1 Energy deposition

As a first test, the energy deposition for the online tagged muons was studied. Figures 5.5 to 5.8 show the distribution of the total energy in the 3 cells in the tower where the muon has been tagged for 4 modules. The distributions are shown for the MTag algorithm running online in the DSP and compared to the results obtained offline with the same data. In consequence, the differences between what we will refer to as online and offline are the limitations that the DSP introduces in terms of processing (as the DSP is a fixed point processor). Note also that the energy reconstruction method used online is the OF1 algorithm with 1 iteration while for the offline case is the Fit method.

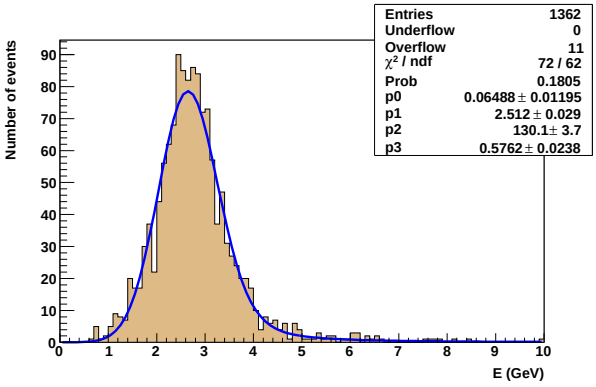

(a) Energy deposited by the offline tagged muons in module LBA13.

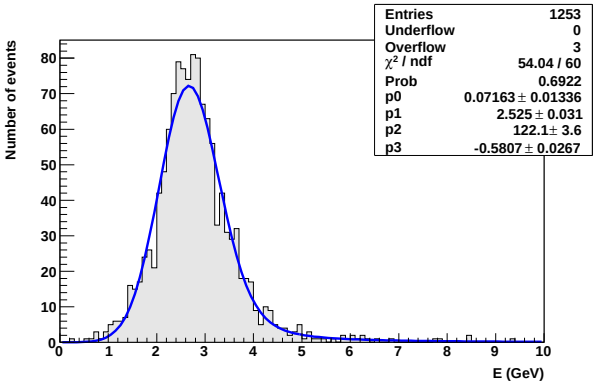

(b) Energy deposited by the online tagged muons in module LBA13.

Figure 5.5: Energy deposited by the offline and online tagged muons. All results are fitted to a Landau-Gaussian convoluted distribution and correspond to module LBA13 in run 1109.

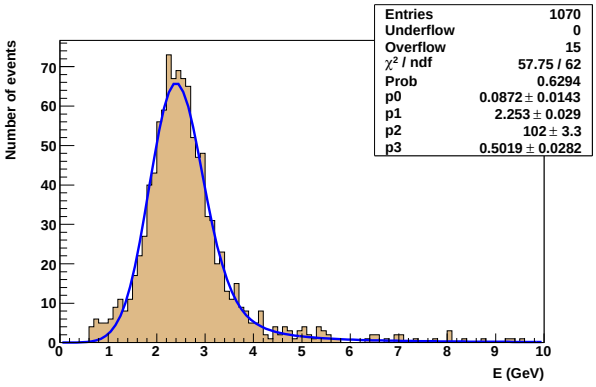

(a) Energy deposited by the offline tagged muons in module LBA14.

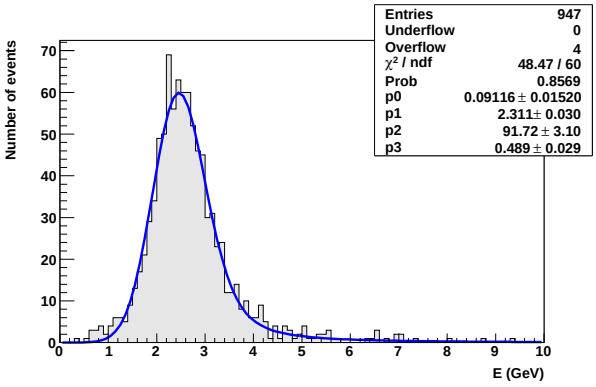

(b) Energy deposited by the online tagged muons in module LBA14.

Figure 5.6: Energy deposited by the offline and online tagged muons. All results are fitted to a Landau-Gaussian convoluted distribution and correspond to module LBA14 in run 1109.

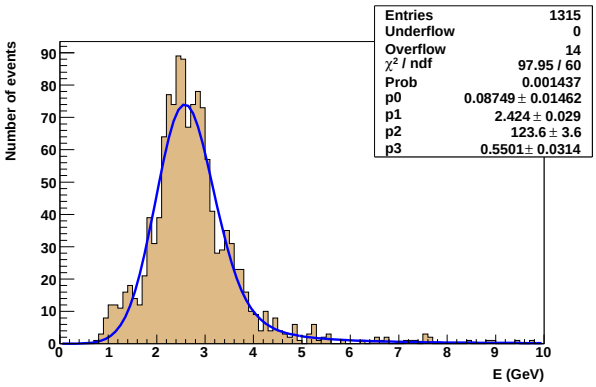

(a) Energy deposited by the muons tagged offline in module LBC14.

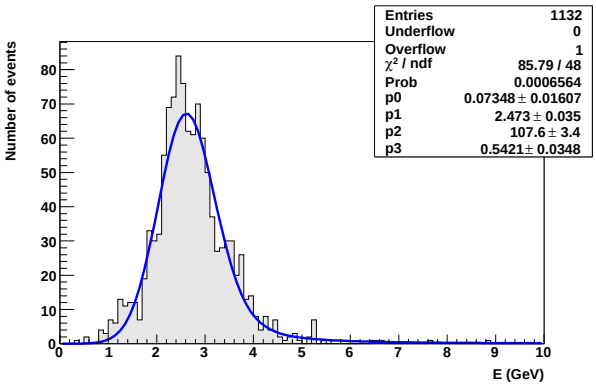

(b) Energy deposited by the muons tagged online in module LBC14.

Figure 5.7: Energy deposited by the offline and online tagged muons. All results are fitted to a Landau-Gaussian convoluted distribution and correspond to module LBC14 in run 1109.

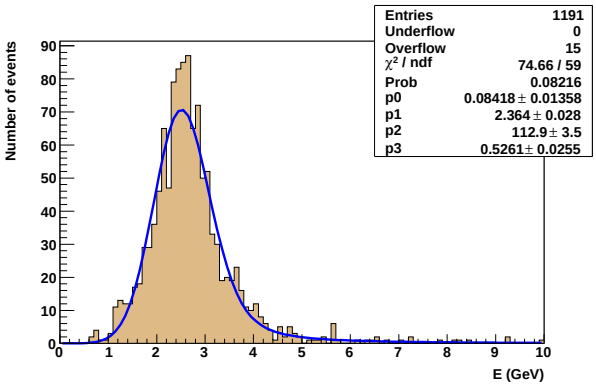

(a) Energy deposited by the muons tagged offline in module LBC46.

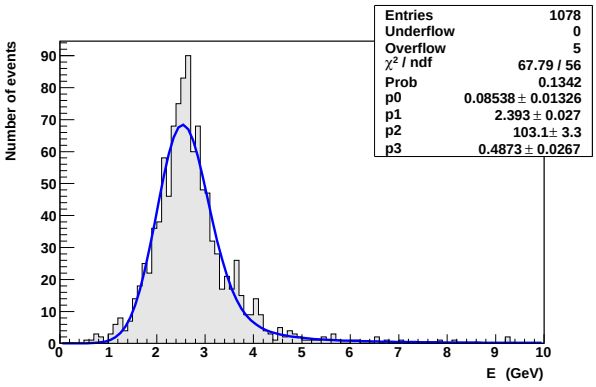

(b) Energy deposited by the muons tagged online in module LBC46.

Figure 5.8: Energy deposited by the offline and online tagged muons. All results are fitted to a Landau-Gaussian convoluted distribution and correspond to module LBC46 in run 1109.

All cases have a Landau-like distribution as expected from real muons coming through the calorimeter. Data were fitted to a Landau-Gaussian convoluted function (see Appendix C), with a ∼2.5 GeV most probable value for the distributions obtained, without major differences between the online and offline results.

5.2.2.2 Online-offline performance comparison

The next step is to compare the total number of muons which have been tagged with the MTag algorithm running online inside the DSP and offline with the same data. Figure 5.9 shows the total of muons tagged as a function of the tower energy for both the online and offline analysis. The distributions are very similar, with slightly more muons tagged in the offline case. Table 5.1 summarizes the number of online and offline muons tagged with the MTag algorithm and for the different modules. Also shown are the cases where the muon was tagged with both methods. The muons tagged online were confirmed by an offline tag in a 90-95% of the cases. Moreover, about 80% of the offline tags were also obtained online.

Then, although the energy reconstruction methods used for online and offline are different, the MTag algorithm performance is satisfactory and almost all the muons tagged in the DSP correspond to an offline tagged muon and most of the muons found offline are also tagged online.

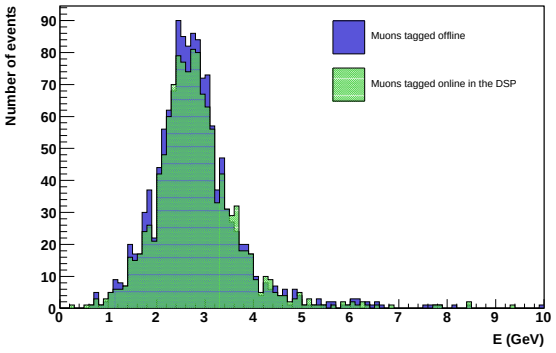

(a) Energy deposited by the offline (blue) and online tagged muons in the ROD DSP (green) in module LBA13.

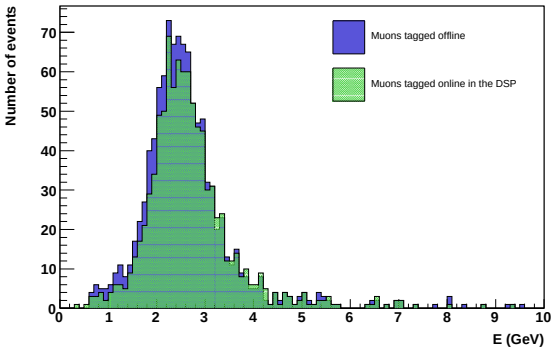

(b) Energy deposited by the offline (blue) and online tagged muons in the ROD DSP (green) in module LBA14.

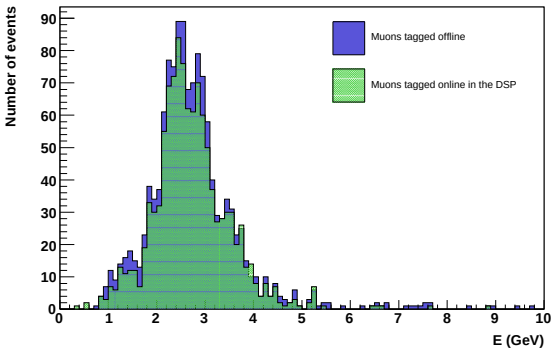

(c) Energy deposited by the offline (blue) and online tagged muons in the ROD DSP (green) in module LBC14.

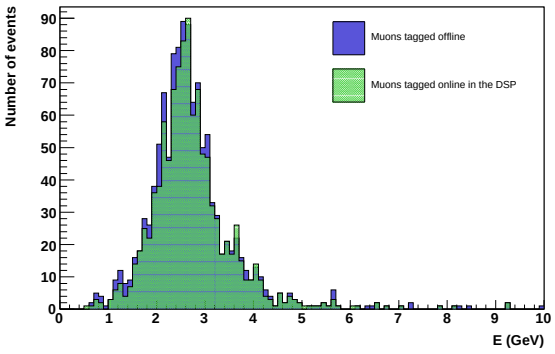

(d) Energy deposited by the offline (blue) and online tagged muons in the ROD DSP (green) in module LBC46.

Figure 5.9: Comparison of the offline and online energy distribution results in run 1109.

These results validate the online performance of the MTag algorithm in the DSP, as muons are actually tagged with a Landau distribution in energy and they represent almost the same total as offline. In addition,

the small differences seen are compatible to small changes in the values of the reconstructed energy due to the fact that different methods were employed for this calculation.

Table 5.1: Comparison between the number of offline and online tagged muons for the injected run 1109. A low energy threshold of 150 MeV has been used for both the offline and online algorithms.

Modules	Nb Events	N_μ offline	N_μ online	N_μ coincidence	N_μ coincidence / N_μ offline	N_μ coincidence / N_μ online
LBA13	63517	1362	1253	1166	86%	93%
LBA14	63513	1070	947	901	84%	95%
LBC14	63517	1315	1132	1041	79%	92%
LBC46	63517	1191	1078	979	82%	91%

5.3 Performance in Commissioning'06 Cosmics Runs

During July and August 2006, a new series of cosmics runs have been taken with the TileCal detector in standalone mode. By that time, The MTag DSP code was ready and its performance validated with injected data. Hence, all the data which were taken during this period used OF1i1 for online energy reconstruction and its output used by the MTag algorithm for online muon tagging in the DSP. Table 5.2 shows a brief summary of the cosmics runs taken with the online MTag at the ROD DSPs.

Table 5.2: Summary of the TileCal standalone cosmics runs taken during July and August 2006 using online muon tagging at the ROD DSPs.

Run Nb	Trigger type	Events	Date	TileCal modules
60922	single tower	3181	25-July-06	LBA45 - LBA52, LBC13, LBC15 - LBC20
60955	single tower	2737	26-July-06	LBA45 - LBA52, LBC13, LBC15 - LBC20
60962	single tower	600	27-July-06	LBA45 - LBA52, LBC13, LBC15 - LBC20
60964	single tower	1526	27-July-06	LBA45 - LBA52, LBC13, LBC15 - LBC20
61000	single tower	2720	1-August-06	LBA45 - LBA52, LBC13, LBC15 - LBC20
61077	single tower	1036	7-August-06	LBA45 - LBA52, LBC13, LBC15 - LBC20
61139	single tower	1702	10-August-06	LBA45 - LBA52, LBC13 - LBC20
61144	single tower	2035	11-August-06	LBA45 - LBA52, LBC13 - LBC20
61145	single tower	7129	12-August-06	LBA45 - LBA52, LBC13 - LBC20

Figure 5.10 shows the multiplicity of tagged muons, the energy deposited by these muons and the total muons tagged as a function of the η and ϕ coordinates with the MTag running online in the DSPs. All results correspond to run 61000.

Figures 5.11 to 5.13 show the energy distributions for the online tagged muons in the ROD DSPs using the 0F1i1 algorithm for energy reconstruction. The results are compared with the distributions obtained with the offline MTag algorithm using the Fit method as the energy reconstruction algorithm and for different runs.

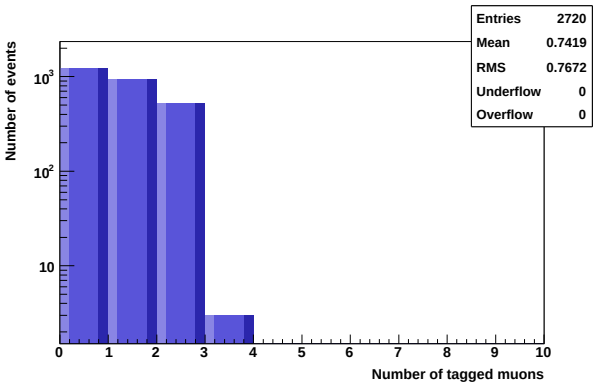

(a) Multiplicity of tagged muons.

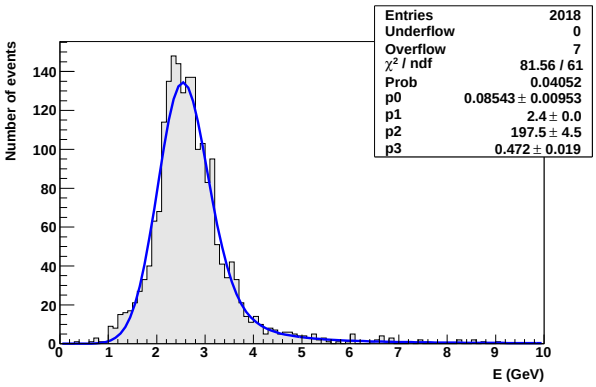

(b) Energy deposited by the tagged muons.

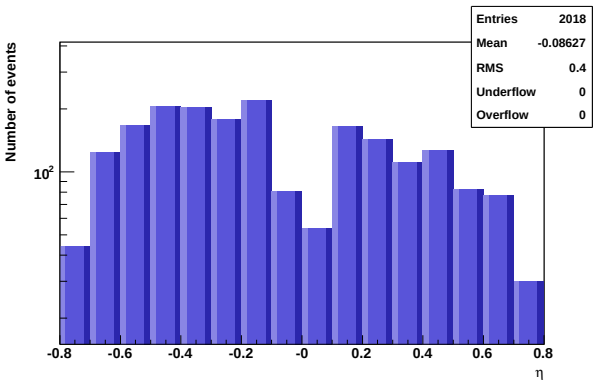

(c) Tagged muons as a function of η.

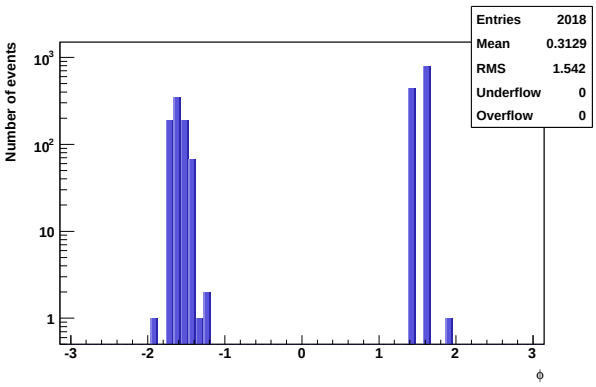

(d) Tagged muons as a function of ϕ.

Figure 5.10: Online results for run 61000.

As shown in these figures, the online results do not agree completely with the offline results. The reason for this is that the weights used in the DSP for the OF1i1 algorithm were calculated for a phase interval of -15 ns $< \tau <$ 15 ns, a cut has been applied so that only muons tagged with phase in this range are considered. Once this cut has been applied to the phase value obtained for OF1i1 for the cells in the outermost layer, comparisons between the online and offline performance of the MTag algorithm can be made.

The results obtained for the total offline and online tagged muons with and without the cut above are summarized in tables 5.3 and 5.4, respectively. In both cases, the muons tagged online are confirmed by an offline tag in more than 90% of the cases. However, without the cut only ∼70% of the offline tagged muons are also tagged online. Applying the $|\tau| <$ 15 ns cut, this percentage is improved to ∼85%.

In order to understand these discrepancies between the online and offline results, the values of the reconstructed energy with the Fit and OF1i1 algorithms have been compared. Figure 5.14 shows the energy obtained with OF1i1 as a function of the energy obtained with the Fit method for all channels of all modules in run 61000. Without the cut in phase (Figure 5.14 (a)), points with huge discrepancies between the energies with Fit and OF1i1 are present. Once the cut is applied (Figure 5.14 (b)) the situation improves and the points are mostly scattered along a line close to the diagonal $E_{\mathrm{FIT}} = E_{\mathrm{OF1i1}}$.

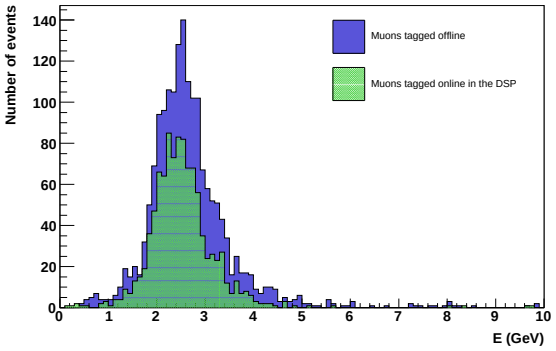

(a) Run 60922.

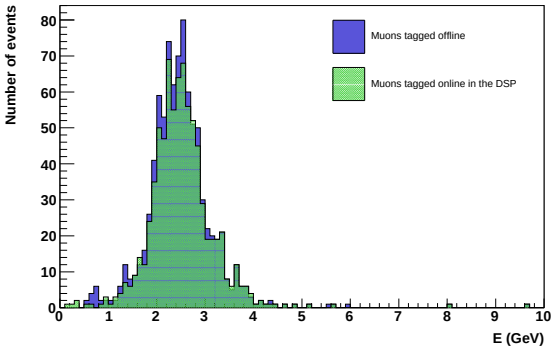

(b) Run 60922 with the cut $|\tau| < 15$ ns applied.

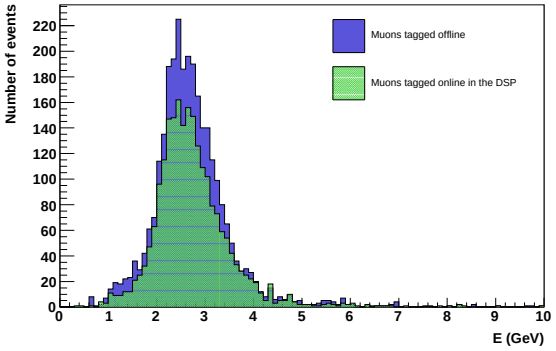

(c) Run 60955.

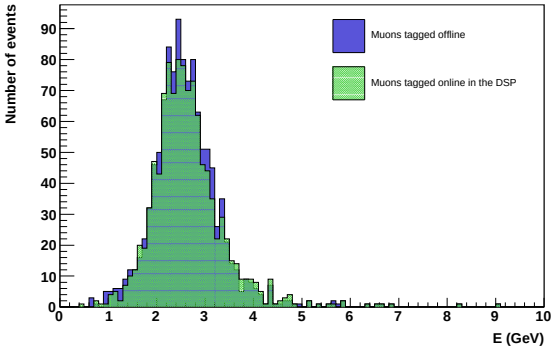

(d) Run 60955 with the cut $|\tau| < 15$ ns applied.

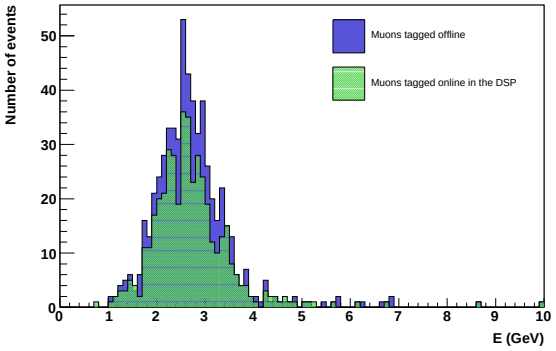

(e) Run 60962.

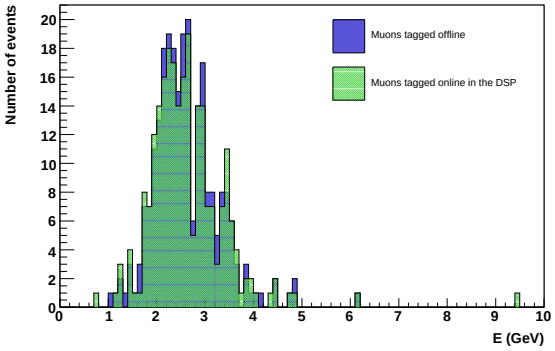

(f) Run 60962 with the cut $|\tau| < 15$ ns applied.

Figure 5.11: Comparison of the offline (blue) and online (green) energy distribution results for all the modules used in cosmics runs 60922, 60955 and 60962.

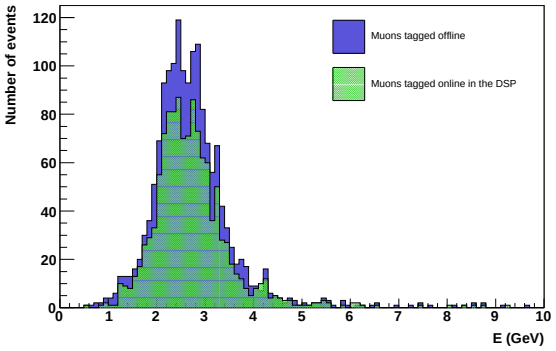

(a) Run 60964.

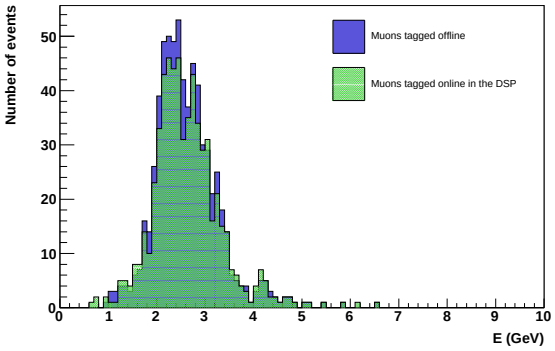

(b) Run 60964 with the cut $|\tau| < 15$ ns applied.

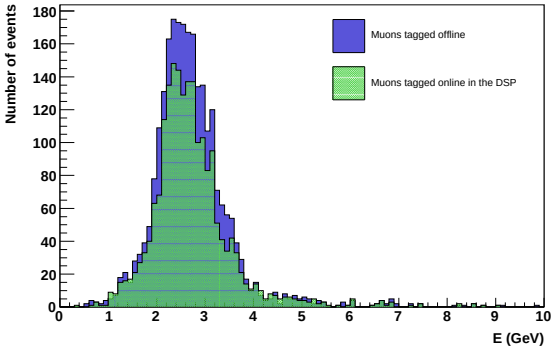

(c) Run 61000.

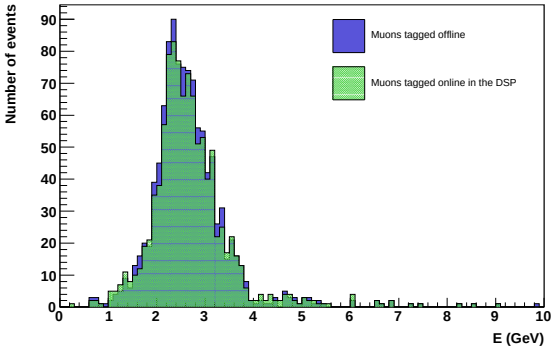

(d) Run 61000 with the cut $|\tau| < 15$ ns applied.

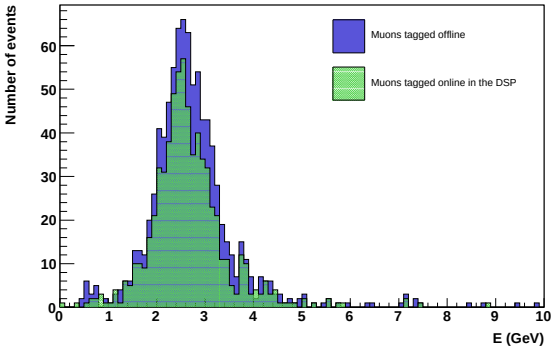

(e) Run 61077.

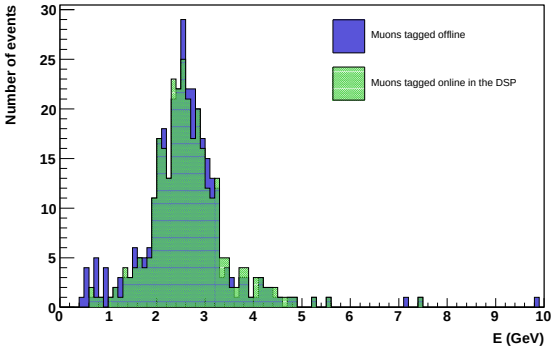

(f) Run 61077 with the cut $|\tau| < 15$ ns applied.

Figure 5.12: Comparison of the offline (blue) and online (green) energy distribution results for all the modules used in cosmics runs 60964, 61000 and 61077.

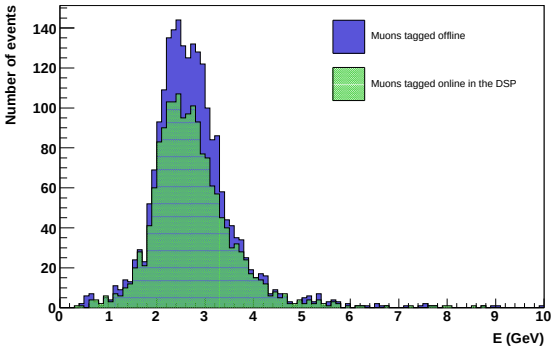

(a) Run 61139.

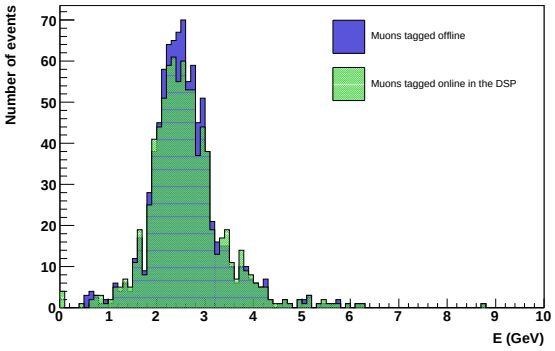

(b) Run 61139 with the cut $|\tau| < 15$ ns applied.

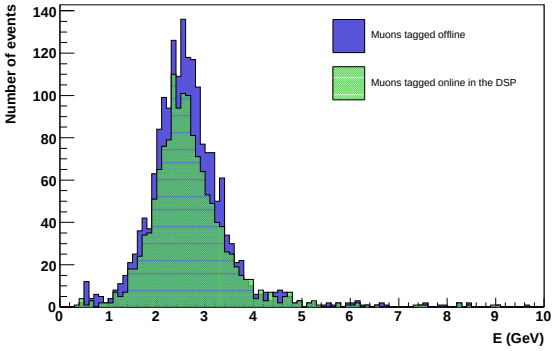

(c) Run 61144.

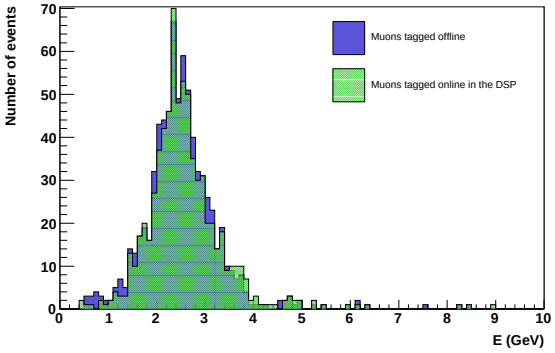

(d) Run 61144 with the cut $|\tau| < 15$ ns applied.

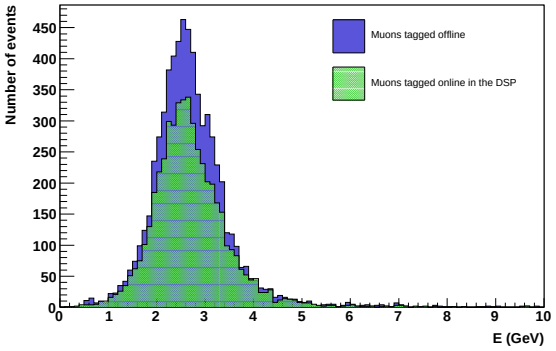

(e) Run 61145.

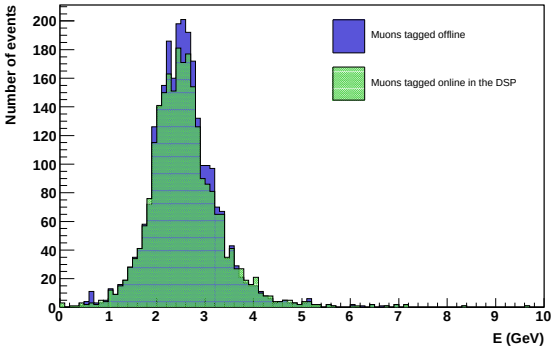

(f) Run 61145 with the cut $|\tau| < 15$ ns applied.

Figure 5.13: Comparison of the offline (blue) and online (green) energy distribution results for all the modules used in cosmics runs 61139, 61144 and 61145.

Table 5.3: Comparison between offline and online results. A low energy threshold of 150 MeV has been used for both offline and online algorithms.

Run Nb	Nb Events	N_μ offline	N_μ online	N_μ coincidence	N_μ coincidence / N_μ offline	N_μ coincidence / N_μ online
60922	3181	1758	1019	981	56%	96%
60955	2737	2927	2245	2053	70%	91%
60962	600	594	439	416	70%	95%
60964	1526	1635	1227	1145	70%	93%
61000	2720	2532	2018	1824	72%	90%
61077	1036	900	679	614	68%	90%
61139	1702	2197	1695	1519	69%	90%
61144	2035	1842	1417	1273	69%	90%
61145	7129	6560	5008	4555	69%	91%

Table 5.4: Comparison between offline and online results selecting events with $|\tau| < 15$ ns. A low energy threshold of 150 MeV has been used for both offline and online algorithms.

Run Nb	Nb Events	N_μ offline	N_μ online	N_μ coincidence	N_μ coincidence / N_μ offline	N_μ coincidence / N_μ online
60922	3181	878	793	761	86%	96%
60955	2737	1164	1090	1007	86%	92%
60962	600	254	243	223	85%	96%
60964	1526	679	618	580	87%	94%
61000	2720	1097	1049	953	83%	91%
61077	1036	341	313	283	85%	90%
61139	1702	909	857	773	85%	90%
61144	2035	753	712	639	85%	90%
61145	7129	2662	2499	2290	86%	92%

Nevertheless, the online energies with OF1i1 are systematically smaller than with the Fit method. Recent studies show that this shift between the OF1i1 and Fit energies is due to the pedestal treatment and current developments in the DSP online energy reconstruction code are focused on this issue.

Summing up, even though the energy taken as input by the MTag algorithm is not fully correct, the algorithm has been used in TileCal commissioning cosmics runs and is successfully working online in the DSP: almost all the muons (90-95%) tagged online in the DSP are also confirmed offline and, when using the correct weights for OF1i1 energy reconstruction, most of the offline tagged muons ($\sim$85%) tagged offline are also tagged in the DSP.

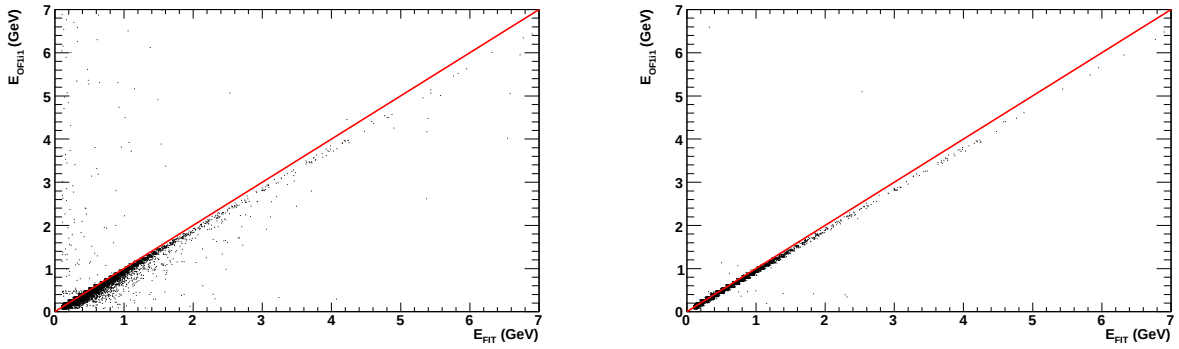

(a) Correlation between the reconstructed energy values with OF1i1 and Fit.

(b) Correlation between the reconstructed energy values with OF1i1 and Fit with the cut $|\tau| < 15$ ns applied.

Figure 5.14: Comparison of the energy reconstruction with the OF1i1 and Fit algorithms for run 61000.

5.4 DSP Processing Time Measurements

The processing time used in the DSP is a very important property, as only a 10 μs latency is available at LVL1 in order to work at a maximum rate of 100 kHz without introducing dead time. However, this maximum rate will not be achieved during the first years of LHC operation (the expected rate for this period is ∼40 kHz) and the rate in cosmics acquisition in the commissioning is ∼1 Hz.

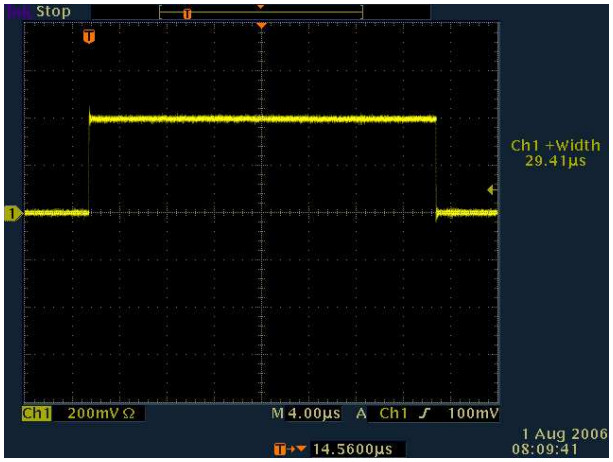

Figure 5.15: DSP proccessing time measurement running OF1 1 iteration and MTag in staging mode.

The DSP processing time has been measured in the TileCal-Valencia laboratory at CERN. For this, the DSP code has been adapted so that when the processing of the data starts a particular test point pin in the PU mezzanine board (GPIO 11) is set to 1. Once the event is processed, the pin is set back to 0. The width of the resulting pulse, which can be obtained with an oscilloscope, is the measurement of the processing time in the DSP.

Measurements have been taken for all ROD processing modes (staging and full mode) and all online algorithms already implemented (OF and MTag) injecting data with the OMB. The injected data were taken from past commissioning runs, selecting events where a muon was acquired.

Figure 5.15 shows the pulse for the DSP working in staging mode (2 super-drawers per DSP) and applying the OF1i1 and MTag algorithms. Table 5.5 shows the timing measurements for all the cases. Copy Mode means that the raw data are simply transmitted with no online algorithms applied on them, used as a reference of the minimum time needed in the DSP for data transmission. From these measurements, one can conclude that the time used by the MTag algorithm is $\sim$1.1 μs in full mode and $\sim$2.2 μs in staging mode.

Table 5.5: DSP proccessing time results.

	Timing	
	Full mode (μs)	**Staging mode (μs)**
Copy Mode	3.1	3.4
OF1 no iter	8.8	-
OF1 no iter and MTag	10.0	-
OF1 1 iter	13.1	27.1
OF1 1 iter and MTag	14.2	29.4

Globally these times are not close to the 10 μs limit set by LVL1. However, the current implementation of the DSP code is in C and a great improvement in terms of speed is expected in the pass to assembler. Furthermore, the OF algorithm currently implemented for the commissioning makes use of iterations to find the proper phase of the signals as the trigger is not synchronized with the cosmic muon. In the final ATLAS environment, the timing will be fixed by the LHC clock and no iteration will be needed for a correct energy reconstruction, with the consequent time saving.

Summing up, the processing time results obtained with the current implementation of the DSP code are very encouraging as the MTag algorithm turned out to be a fast algorithm when running in the DSP. With the pass to assembler it is feasible to achieve a total processing time of 10 μs for ATLAS operation.

Chapter 6

Implementation in the Athena framework

6.1 The Athena framework

Offline computing covers all processing from storing raw data up to the final analysis, as well as Monte Carlo generation, detector simulation and event display. Athena [37] is the general framework for the ATLAS offline software, based upon the Gaudi architecture. The Athena code is based on the C++ language and uses all of its object oriented features.

Athena can be seen as a skeleton which provides most of the common functionalities and into which the developers can insert their own code. This way, the software developed in Athena can use many useful background classes (physical units manipulation, geometry entities, etc.), using prepared services for things such as loop over events. Figure 6.1 shows the main Athena components and their relationships.

ATLAS software is organized into a hierarchical structure of projects and packages. All packages are stored in an official CVS repository, which enables efficient sharing of source code among the members of a distributed development team. Each package has a Tag number which distinguishes between different versions. A project consists of a complete collection of tagged packages and it is identified with a release number.

A Configuration Management Tool (CMT) [38] is used to manage, build (compile and link) and run ATLAS software. The information needed to build or run a package is grouped in a single requirements file, from which CMT sets automatically the configuration parameters required to operate the packages.

The Athena framework distinguishes between data objects and algorithm objects very strictly. A quantity-like entities (hits, points, tracks, digits, raw channels, etc.) should be implemented by deriving their class from the DataObject base class. On the other hand anything like a procedure should be designed as a child class of the Algorithm base class.

6.1.1 Algorithms

The principal functionality of an algorithm is to take input data, manipulate them and produce new output data. All data objects are kept in the common StoreGate (see Section 6.1.3). All algorithms are able to save or

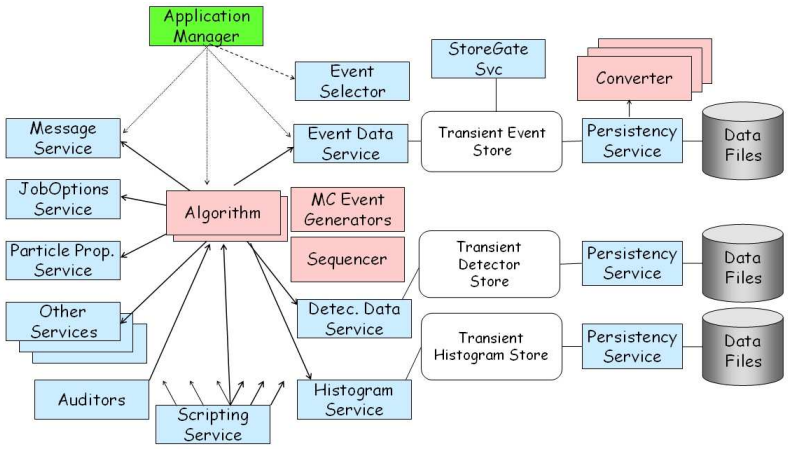

Figure 6.1: Athena architecture object diagram.

retrieve any data object from there via the StoreGate Service.

The interface of the Algorithms (inherited from the Algorithm class) provides connection to Athena common services. Three methods (initialize, execute and finalize) have to be implemented in each algorithm, in addition to the constructor and destructor.

Algorithms are required to be configurable, so that certain parameters can be initialized when the algorithm is called. These parameters, known as properties, are specified with JopOptions files, which are conventional pyhton scripts used to control the configuration of algorithms and other applications at run-time.

6.1.1.1 Tools and AlgTools

Often some of the processing is delegated by Algorithms to AlgTools. In the Athena framework, a Tool is an encapsulated piece of code which needs to be executed only when special events occur. AlgTools inherit from the AlgTool base class to guarantee compatibility with Algorithms and grant a set of basic services and functions.

6.1.2 Services

The main services that algorithm objects use in Athena are the following:

- **Event Data Service:** provides storing and retrieving all event related data, whose lifetime is one simple event only.
- **Detector Data Service:** stores information about detector, such as its geometrical and environment parameters.
- **Histogram Service and Ntuple Service:** histograms and ntuples made by these services have lifetime longer than a simple event, and typically collect some parameters through all events. Ntuples cannot be kept only in memory, data are accumulated and written to disk continuously during the execution of a job.

- **Message Service:** provides reporting about progress and other communication with the outside world.

6.1.3 Data Store

The Transient Data Store (TDS) is the main channel of communication among different Athena modules. The ATLAS implementation of the TDS is called StoreGate. Each algorithm can create Data Objects and save them into the StoreGate. Any algorithm is able to retrieve data from the StoreGate, no matter if they were generated by another algorithm (a transient source) or a file or database (persistent sources). Several different transient stores build up the entire TDS (e.g. the Transient Event Store, the Transient Detector Store, the Transient Histogram Store, the Transient Ntuple Store, etc.).

The TDS also manages conversion of Data Objects from/to their persistent form (e.g. reading from/saving to a file) via the persistency services. The structure of the entire TDS and its integration into the Athena framework are shown in Figure 6.1.

6.1.4 Running Athena

An Athena job starts by creating an instance of the Application Manager component. The Application Manager initializes a minimal set of basic and essential services and then gives the control to specialized service called the Event Loop Manager. The Event Loop Manager firstly initializes all top algorithms (specified via the JobOption Service), executes them in the physical-event loop, and finalizes them at the end. This is done by invoking the special methods mentioned above. The top algorithms are executed unconditionally in the order they have been declared. The top algorithms invoke execution of another components (such as AlgTools) according to the hierarchical structure of the software.

6.2 Muon Trigger Algorithms Status

The Trigger Vertical Muon Slice [39] is the full integrated chain of Trigger/DAQ running from the ATLAS muon spectrometer data and is composed by three trigger levels: a hardware implemented LVL1 and a software implemented High Level Trigger (HLT) composed by LVL2 and EF (see Section 2.4.5 for details).

The HLT Event Selection Software (HLTSSW) that runs on dedicated farms is common to LVL2 and EF. The HLTSSW is composed by four components: the Steering, the Data Manager, the Event Data Model and the HLT Algorithms.

As LVL2 algorithms run on full granularity data on RoI detected by LVL1, only 1-2% of the full event size is actually used. The total latency time at LVL2 is 10 ms and the rate is reduced from ∼75 kHz (LVL1 output) to 1 kHz. Hence, one of the key points in LVL2 algorithm implementation is to avoid lengthy calculations (such as non-linear fits) and time-consuming operations (such as alignment or geometry). The algorithms used in LVL2 for the muon sector (as shown in Figure 6.3) are the following:

- **muFast:** is the first algorithm to run at LVL2 and reconstructs the pattern in the RPC chamber which fired the LVL1 trigger (momentum and trajectory).
- **muComb:** is the next algorithm to run at LVL2. This algorithm combines the Inner Detector tracking measurements with the Muon Spectrometer measurements by matching E_{T}, ϕ and η of the two trajectories.

- **muTile:** this algorithm has a similar concept as the one explained in this report, but uses the channel energy obtained offline. The main limitation of this algorithm is its processing time, which at present is 30 ms, well above the maximum 10 ms at LVL2.

- **TrigDiMuon or TrigJPsi:** is a specific algorithm for di-muon trigger from the J/ψ decay.

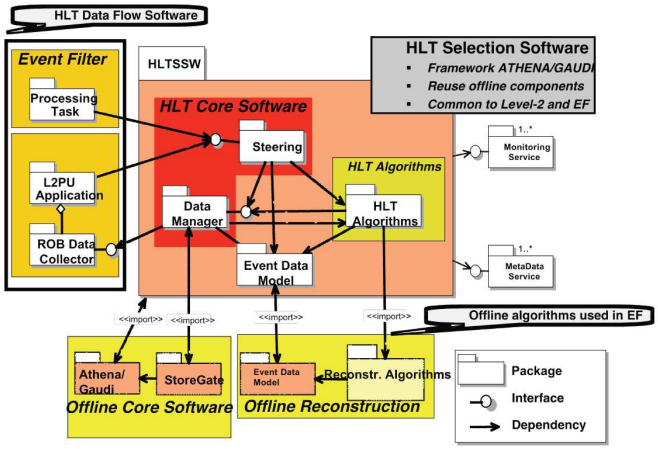

Figure 6.2: HLT scheme.

After LVL2, EF accesses and reconstructs the full event with a latency of 1-2 s. Two offline packages have been adapted to work in the HLT framework: MOORE (Muon Object Oriented REconstruction), which performs track reconstuction in the Muon Spectrometer, and MuId (Muon Identification), which extrapolates the track to the interaction point (MuId Standalone) and combines the information from the muon and inner detectors (MuId Combined). In order to use these packages for HLT, explicit dependencies from Athena have been avoided merging the code in a single online package called TrigMOORE.

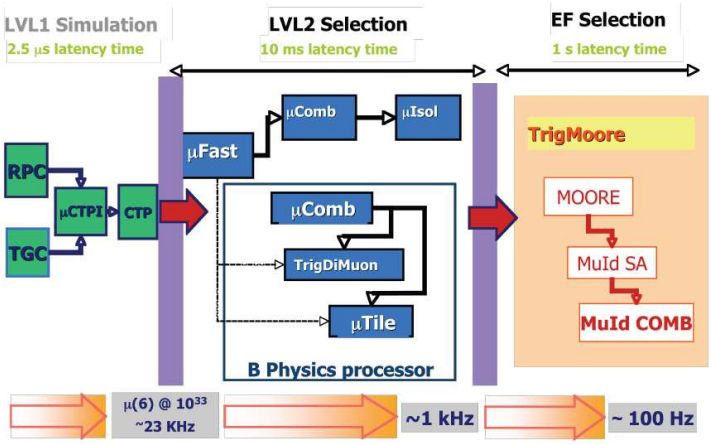

Figure 6.3: Muon trigger algorithms scheme.

6.3 MTag-MET Offline Code

This section is devoted to the description of all the code related with the decoding of the MTag-MET fragment present in the ROD output data as a separated fragment, as commented in Section 3.4.2.3, and the use of this information inside the Athena framework. The packages which have been updated to handle this new piece of information in the ROD data format are described in the following subsections. All the code is available in the ATLAS CVS repository which is browsable in the following web page:

`http://atlas-sw.cern.ch/cgi-bin/viewcvs-atlas.cgi/offline/`

6.3.1 TileEvent package

The file structure of this package is shown in Figure 6.4. This package provides event data model classes for TileCal reconstruction. All classes in TileEvent package can be split in two categories: classes for raw data and classes for reconstructed objects. The raw data classes are:

- **TileDigits:** contains a vector of digital samples from the PMT pulses, known in the Athena environment as "digits".
- **TileRawChannel:** contains the result of the application of the reconstruction algorithms explained in Section 3.2 to TileDigits. These objects contain amplitude, time, quality and pedestal estimation for a given channel.
- **TileBeamElements:** is a class similar to TileDigits, but with information from extra detectors (beam chambers and beam counters at the test beam setups, special coincidence trigger boards at the commissioning, etc.).
- **TileTTL1:** is a class similar to TileDigits but with the information used in LVL1 trigger, i.e., the output pulse from the analog trigger tower adders described in Section 2.5.2.

In the three first cases, the information is stored in the StoreGate in such a way that in each container (TileDigitsContainer, TileRawChannelContainer, etc.) has 256 collections (with the information from one super-drawer) which has 48 raw data objects (one per channel).

In this package the following Reco classes are also defined:

- **TileCell:** contains the result of the reconstruction with the total energy deposited in a cell and calibrated with the electromagnetic scale. Normally TileCells are stored together with LArCells in the CaloCellContainer.
- **TileMu:** contains the results of the TileLookForMuAlg algorithm in the TileMuId package, an algorithm specifically implemented for offline uses.

A new class called TileL2 has been added to the previous ones to store the MTag and MET information calculated online at the ROD level. There is one instance of this class per super-drawer and it is stored in a specific TileL2Container without using collections.

The TileL2 class, defined in the TileL2.cxx and TileL2.h files, has the following member variables:

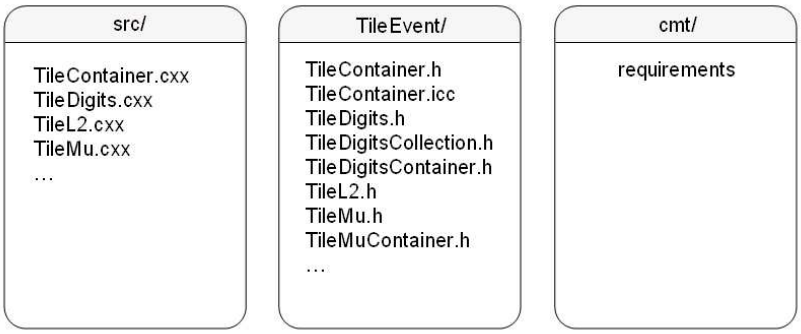

Figure 6.4: Directory structure of the TileEvent package.

- `int m_ID`: fragment ID of the super-drawer.
- `vector<u_int> m_val`: value of the 32-bit MTag word.
- `vector<double> m_eta`: η coordinate of the muons found.
- `double m_phi`: ϕ coordinate of the muons found. Note that as a TileL2 object contains information from one super-drawer, the value of ϕ is the same for all the muons tagged in the object. In consequence it is not needed to use a vector for this coordinate.
- `vector<u_int> m_Et`: total transverse energy in the super-drawer.

Similarly to the TileCell and TileTTL1 case, a TileL2Container is defined in the TileContainer.h file as a generic TileContainer which stores TileL2 objects:

```
typedef TileContainer<TileL2> TileL2Container
```

6.3.2 TileByteStream package

In the Athena environment *ByteStream* refers to the raw data information inside nested headers and trailers, as described in Section 3.4. This information should be unpacked by interpreting the headers to know what type of data is contained in the ByteStream. The file structure of this package is shown in Figure 6.5.

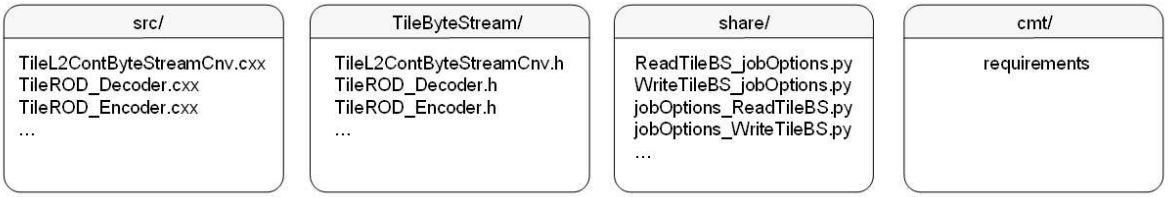

Figure 6.5: Directory structure of the TileByteStream package.

This package contains the TileROD_Decoder, which provides conversion between ByteStream (raw data) and either TileRawChannels or TileCells. The following methods have been added to the TileROD_Decoder class in order to decode the MTag-MET information in the ROD data format:

- `void unpack_frag10(uint32_t version, const uint32_t* p, TileL2Container & v)`: decodes MTag-MET fragment in staging mode (fragment type 0x10, as described in Section 3.4.2.3), filling TileL2 objects and putting them in a TileL2Container.
- `void unpack_frag11(uint32_t version, const uint32_t* p, TileL2Container & v)`: very similar to the previous one, this method decodes MTag-MET fragment in full mode (fragment type 0x11, as described in Section 3.4.2.3), filling also TileL2 objects and putting them in a TileL2Container.
- `void fillCollectionL2(const ROBData * rob, TileL2Container & v)`: this method fills a TileL2Container with TileL2 objects by calling the `unpack_frag10` and `unpack_frag11` methods.
- `StatusCode convert(const RawEvent* re, TileL2Container* L2Cnt)`: searches the ROB fragments in the event for MTag-MET fragments in the ByteStream and fills the TileL2Container by calling the method `fillCollectionL2`.

A new ByteStream Converter class named TileL2ContByteStreamCnv has also been created, which takes care of the creation of the TileL2Container and the decoding by calling the methods above.

With this approach, the MTag-MET fragment is decoded and the output present in the StoreGate for other algorithms, such as TileMuRODToNtuple (see below), without unpacking the whole ByteStream information and without constructing TileDigit or TileRawChannel objects.

6.3.3 TileMuId package

The file structure of this package is shown in Figure 6.6. This package was meant to provide the TileMu information to the StoreGate so that it was available for other algorithms and for storing it in an ntuple. In a similar way, the following algorithms have been added for the LVL2 information computed in the RODs:

- **TileDecodeL2 algorithm:** in previous versions of the ROD DSP code the MTag information was available in the raw data as an extra word at the end of the digitizer fragment. This algorithm was used for decoding this information when it was still present in the TileDigitsCollection and puts it in TileL2Container to be available for other algorithms.
- **TileMuRODToNtuple algorithm:** retrieves TileL2 objects from TileL2Container and stores the information in a directory in the output ntuple. A new directory is created in the ROOT file called *TileMuRODTag* with the following variables inside:
  - `Int_t NMuons`: total number of muons found in the event (in all the super-drawers).
  - `Float_t EtaMuons[50]`: η coordinate of the muons found. Only the first `NMuons` elements of this vector are actually filled in each event.
  - `Float_t PhiMuons[50]`: ϕ coordinate of the muons found. As in the previous case, only the first `NMuons` elements of this vector are actually filled in each event.

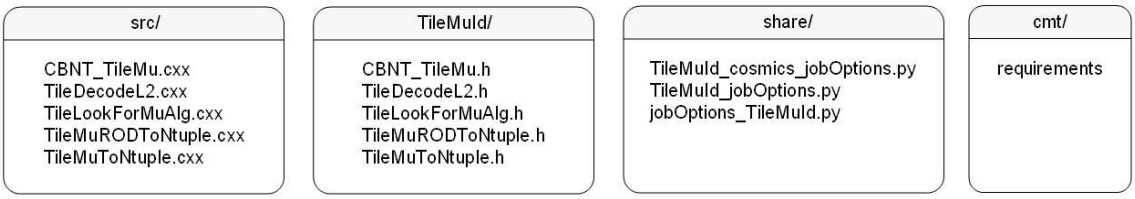

Figure 6.6: Directory structure of the TileMuId package.

6.3.4 Overall Status and Future plans

With the developments inside Athena presented in the previous subsections, full MTag-MET raw data fragment decoding is available and ready to use for data reconstruction. In fact, the cosmics commissioning data presented in Chapter 5 were decoded using the new methods in the TileByteStream package and saved to the standard ntuple using the TileMuRODToNtuple algorithm.

The next steps to be taken in the offline developments related with the ROD DSP MTag and MET algorithms will be, on one hand, to test this MTag-MET decoding by adding new encoding capabilities. The idea is to encode simulated data to ByteStream and decode it again to verify that these decoded data matches with the original simulated data.

On the other hand, a new trigger algorithm will be implemented in order to use the TileL2 objects in StoreGate TileL2Container at LVL2 so that new secondary Regions of Interest could be opened. This new LVL2 algorithms to be implemented will have the advantage that no processing time would be needed for loops over channels or energy calculations as these operations have been previously done in the ROD DSPs. In consequence, a good performance in terms of timing is expected for this algorithm, being very convenient for contributing to the final decision at LVL2.

Conclusions

In this research report, the development of a low p_{T} muon tagging algorithm for LVL2 trigger (MTag) in the Hadronic Tile Calorimeter of the ATLAS experiment has been presented. With this algorithm muons are tagged on the flight using their characteristic pattern in the energy deposition in the calorimeter cells, delimited by an upper and a lower threshold. This algorithm will be especially useful for triggering low p_{T} muons, as the ATLAS muon spectrometer trigger efficiency in this energy range is very poor. Furthermore, previous studies show that its implementation at LVL2 is possible as the algorithm tag rate obtained taking into account the inclusive muon production at LHC is expected to be ∼860 Hz, compatible with the 1 kHz LVL2 maximum rate.

As an example, the efficiency of several B-physics channels like the $\mathrm{B_s^0} \rightarrow \mathrm{J}/\psi\mathrm{K_s^0}$ and $\mathrm{B_s^0} \rightarrow \mathrm{J}/\psi\phi$ could be improved with this algorithm, as both muons from the $\mathrm{J}/\psi \rightarrow \mu\mu$ decay would be tagged (one with high momentum by the Muon Spectrometer at LVL1 and the other with lower p_{T} by this MTag algorithm at LVL2).

The feasibility of the algorithm has been proved using Monte Carlo samples of single muons and different B-physics channels, quantifying the results in terms of μ-tagging efficiencies and fake rates. Efficiency values of ∼75-80% are obtained in the $p_{\mathrm{T}} > 2$ GeV range for physics processes. The fraction of fake tags observed is ∼6%.

This algorithm has been implemented in the ROD DSPs, so that it is applied to all the events accepted by LVL1 trigger with no time cost at LVL2. It takes as input the energy previously reconstructed with Optimal Filtering and uses a look up table to apply the corresponding thresholds. The MTag algorithm is currently coded in C, with a processing time in the DSP of ∼1 μs per super-drawer.

The output of the MTag algorithm is available in the ROD data format for LVL2 trigger in dedicated fragments where the MTag and MET information is packed. For this purpose, two new fragment types (0x10 and 0x11) have been created for the two DSP operation modes (staging and full mode, respectively).

The creation of new fragments require a new decoding in the general ATLAS offline sotfware, Athena. New algorithms and methods have been provided inside the Athena framework to unpack the information in these fragments and make it accessible for offline analysis and further trigger studies.

The online performance of the algorithm is being studied by comparing the results obtained for the muon identification online and offline using first ATLAS physics real data: standalone TileCal cosmic rays runs acquired in July and August 2006 during the commissioning of the detector.

The next steps of this work will be to provide proper LVL2 algorithms to the LVL2 trigger and study their performance in terms of latency at LVL2.

Appendix A

List of Acronyms

ADC: Analog to Digital Converter
ALICE: A Large Ion Collider Experiment
ALEPH: Apparatus for LEP Physics at CERN (LEP Experiment)
ALU: Arithmetic Logic Unit
ASIC: Application Specific Integrated Circuit
ATLAS: A Toroidal LHC ApparatuS
BCID: Bunch Crossing Identifier
BT: Barrel Toroid (ATLAS Magnet System)
CERN: *Conseil Européen pour la Recherche Nucléaire*
CIS: Charge Injection System
CKM: Cabibbo-Kobayashi-Maskawa
CMS: Compact Muon Solenoid
CMT: Configuration Management Tool
CNGS: CERN Neutrinos to Gran Sasso
CPU: Central Processing Unit
CRC: Cyclic Redundancy Check
CS: Central Solenoid (ATLAS Magnet System)
CVS: Concurrent Version System
CSC: Cathode Strip Chamber (ATLAS Muon Spectrometer)
CSIC: *Consejo Superior de Investigaciones Científicas*
DAQ: Data AcQuisition
DELPHI: DEtector with Lepton, Photon and Hadron Identification (LEP Experiment)
DMU: Data Management Unit
DONUT: Direct Observation of the NU Tau (FNAL Experiment)
DSDC: *Diseño de Sistemas Digitales y Comunicaciones*
DSP: Digital Signal Processor

EB: Extended Barrel
ECRID: Event ID Counter Reset
ECT: End-Cap Toroid (ATLAS Magnet System)
EF: Event Filter
EMEC: ElectroMagnetic End-cap (ATLAS Electromagnetic Calorimeter)
EWSB: ElectroWeak Symmetry Breaking
FCAL: Forward Calorimeter (ATLAS Hadronic Calorimeter)
FCNC: Flavour Changing Neutral Current
FEB: Front End Board
FF: Flat Filtering
FIFO: First Input First Output memory
FILAR: Four Input Links for ATLAS Read-out
FM: Fit Method
FNAL: Fermi National Accelerator Laboratory
FPGA: Field Programmable Gate Array
HEC: Hadronic End-cap Calorimeter (ATLAS Hadronic Calorimeter)
HLT: High Level Trigger
HLTSSW: High Level Trigger Event Selection Software
HOLA: High-speed Optical Link for ATLAS
HV: High Voltage
ID: Identifier
IFIC: *Instituto de Física Corpuscular*
IGUI: Interactive Graphical User Interface
ISOLDE: Isotope Separation OnLine Device
ITC: Intermediate Tile Calorimeter
L1A: Level 1 Accept
L1ID: Level 1 Identifier
LAr: Liquid Argon (ATLAS Electromagnetic Calorimeter)
LB: Long Barrel
LHC: Large Hadron Collider
LHCb: Large Hadron Collider beauty
LEP: Large Electron Positron collider
LSC: Link Source Card
LTP: Local Trigger Processor
LVDS: Low Voltage Differential Signaling
LVL1: Level 1
LVL2: Level 2
MAC: Multiply-accumulate
MDT: Monitored Drift Tube (ATLAS Muon Spectrometer)
MET: Missing Transverse Energy (E_T)

MIP: Minimum Ionizing Particle
MIPS: Million Instructions Per Second
NIM: Nuclear Instrumentation Module
OC: Output Controller
ODIN: Optical Dual G-LINK
OF: Optimal Filtering
OMB: Optical Multiplexer Board
OPAL: Omni-Purpose Apparatus at LEP (LEP Experiment)
ORX: Optical Receiver
PLL: Phase-Locked Loop
PMT: PhotoMultiplier Tube
PU: Processing Unit
QCD: Quantum ChromoDynamics
ROB: Read Out Buffer
ROD: Read Out Driver
RoI: Region of Interest
ROL: Read Out Link
ROS: Read Out System
RCC: ROD Crate Controller
RPC: Resistive Plate Chamber (ATLAS Muon Spectrometer)
SCT: SemiConductor Tracker
SDRAM: Synchronous Dynamic Random Access Memory
SLAC: Stanford Linear Accelerator Center
SLC: Stanford Linear Collider
SM: Standard Model
SPS: Super Proton Synchrotron
TBM: Trigger and Busy Module
TDAQ: Trigger and Data Acquisition
TDS: Transient Data Store
TGC: Thin Gap Chamber (ATLAS Muon Spectrometer)
TileCal: Tile Calorimeter (ATLAS Hadronic Calorimeter)
TM: Transition Module
TRT: Transition Radiation Tracker
TTC: Trigger and Timing Control
TTCrx: TTC Receiver
TTCvi: TTC VMEbus Interface
Ttype: Trigger type
UV: *Universitat de València*
VME: Versa Modula Europa bus
VLIW: Very Long Instruction Word

WLS: WaveLength Shifter

WWW: World Wide Web

Appendix B

Cell-Channel Mapping

The sum of the readout channel energies in ADC counts to obtain the cell energy values is currently made online in the MTag algorithm at the DSP. Figure B.1 shows a diagram of the TileCal cells in one wedge, with the corresponding PMTs for each cell.

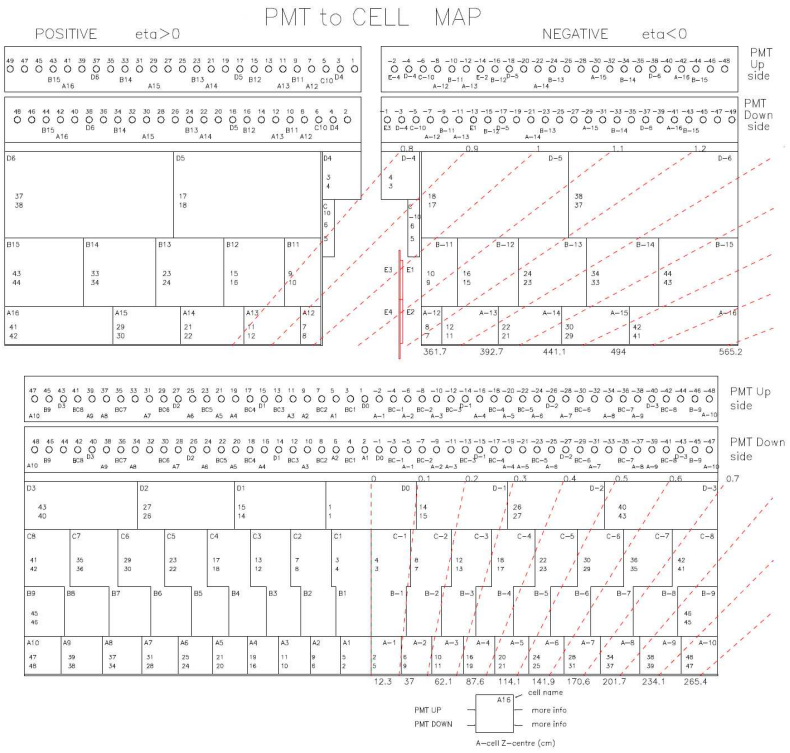

Figure B.1: TileCal Cell-PMT layout.

B.1 Cells-PMT Mapping

Tables B.1 and B.2 show the correspondence between the TileCal cells and the PMT positions sorted by the η-projective towers for the long barrel and the extended barrel respectively. All cells are read out by 2 PMTs, one on the left side of the super-drawer and the other on the right side, devoted in the tables as L and R.

Table B.1: PMT cells map for Long Barrel trigger towers.

η	**PMTs by cell**	**PMT Positions**
0.0 - 0.1	A1R A1L BC1R BC1L D0R	5 2 3 4 1
0.1 - 0.2	A2R A2L BC2R BC2L D1L	9 6 7 8 14
0.2 - 0.3	A3R A3L BC3R BC3L D1R	11 10 13 12 15
0.3 - 0.4	A4R A4L BC4R BC4L D2L	19 16 17 18 26
0.4 - 0.5	A5R A5L BC5R BC5L D2R	21 20 23 22 27
0.5 - 0.6	A6R A6L BC6R BC6L D3L	25 24 29 30 40
0.6 - 0.7	A7R A7L BC7R BC7L D3R	31 28 35 36 43
0.7 - 0.8	A8R A8L BC8R BC8L	37 34 41 42
0.8 - 0.9	A9R A9L B9R B9L	39 38 45 46
0.9 - 1.0	A10R A10L	47 48

Table B.2: PMT cells map for Extended Barrel trigger towers.

η	**PMTs by cell**	**PMT Positions**
0.8 - 0.9	D4R D4L	3 4
0.9 - 1.0	C10R C10L D5R	5 6 17
1.0 - 1.1	B11R B11L D5L	9 10 18
1.1 - 1.2	A12R A12L B12R B12L D6R	7 8 15 16 37
1.2 - 1.3	A13R A13L B13R B13L D6L	11 12 23 24 38
1.3 - 1.4	A14R A14L B14R B14L	21 22 33 34
1.4 - 1.6	A15R A15L B15R B15L A16R A16L	29 30 43 44 41 42

B.2 Channels-PMT Mapping

Tables B.3 and B.4 show the correspondence between the TileCal PMTs placed in the super-drawers and the readout channels for the long barrel and the extended barrel respectively. Note the 3 empty channels (45 from 48 channels are used) in the long barrel and the 16 empty channels (32 from 48 channels are used) in the extended barrel.

Table B.3: Channel-PMT Mapping for Long Barrel.

Channels	PMTs	Channels	PMTs	Channels	PMTs	Channels	PMTs
0	1	12	13	24	27	36	39
1	2	13	14	25	26	37	38
2	3	14	15	26	25	38	37
3	4	15	16	27	30	39	42
4	5	16	17	28	29	40	41
5	6	17	18	29	28	41	40
6	7	18	19	30	–	42	45
7	8	19	20	31	–	43	–
8	9	20	21	32	31	44	43
9	10	21	22	33	36	45	48
10	11	22	23	34	35	46	47
11	12	23	24	35	34	47	46

Table B.4: Channel-PMT Mapping for Extended Barrel.

Channels	PMTs	Channels	PMTs	Channels	PMTs	Channels	PMTs
0	1	12	13	24	–	36	44
1	2	13	14	25	–	37	38
2	3	14	15	26	–	38	37
3	4	15	16	27	–	39	43
4	5	16	17	28	–	40	42
5	6	17	18	29	–	41	41
6	7	18	–	30	33	42	–
7	8	19	–	31	29	43	–
8	9	20	21	32	30	44	–
9	10	21	22	33	–	45	–
10	11	22	23	34	–	46	–
11	12	23	24	35	34	47	–

Appendix C

Gaussian-Landau Convolution Fit

The convolution function is given by:

$$f(\Delta, x) = \frac{1}{\sqrt{2\pi}\sigma} \int_{-\infty}^{+\infty} \mathrm{d}\Delta' \exp\left(-\frac{(\Delta - \Delta')^2}{2\sigma^2}\right) f_{\mathrm{L}}(\Delta', x) \tag{C.1}$$

where Δ is the mean value of the Gaussian function, Δ' is the integration variable, σ is the Gaussian standard deviation and $f_{\mathrm{L}}(\Delta, x)$ is the Landau density function given by:

$$f_{\mathrm{L}}(\Delta, x) = \frac{\phi(\lambda)}{\xi} \tag{C.2}$$

$$\phi(\lambda) = \frac{1}{\pi} \int_{0}^{+\infty} \mathrm{d}u \sin(\pi u) \exp(\lambda u + u \ln u) \tag{C.3}$$

where $\lambda = (\Delta - \Delta_{\mathrm{mp}})/\xi$, Δ_{mp} and Δ_{mean} are the most probable value and the mean value of the Landau distribution respectively.

In the fits performed in Chapter 5, the fit parameters shown stand for:

- **p0:** ξ parameter for the Landau distribution.
- **p1:** Δ_{mp}.
- **p2:** Normalization constant (integral from $-\infty$ to $+\infty$).
- **p3:** σ parameter of the Gaussian distribution.

Appendix D

ATLAS Coordinate System

The ATLAS Coordinate System, shown in Figure D.1, is a right-handed system with the x-axis pointing to the center of the LHC ring, the z-axis following the beam direction and the y-axis going upwards. In Point 1, positive z points towards Point 8 with a slope of -1.23%.

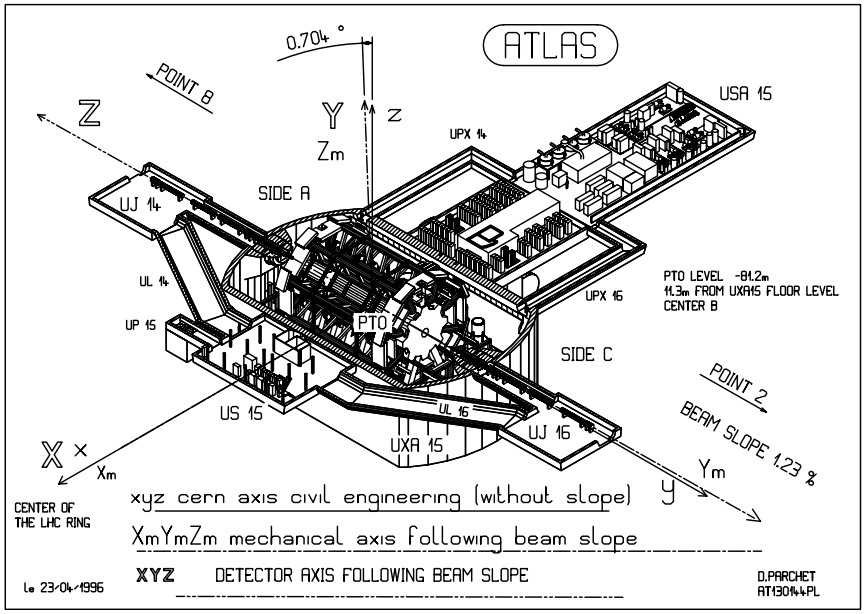

Figure D.1: Scheme of the ATLAS coordinate system.

The transverse momentum p_{T} is defined as the momentum perpendicular to the LHC beam axis. The azimuthal angle $\phi = 0$ corresponds to the positive x-axis and ϕ increases clock-wise looking into the positive z direction. The polar angle θ is measured from the positive z axis. Pseudorapidity, η, is defined by

$$\eta = -\log\left(\tan\frac{\theta}{2}\right) \tag{D.1}$$

Figure D.2 shows the relation between both angular variables graphically.

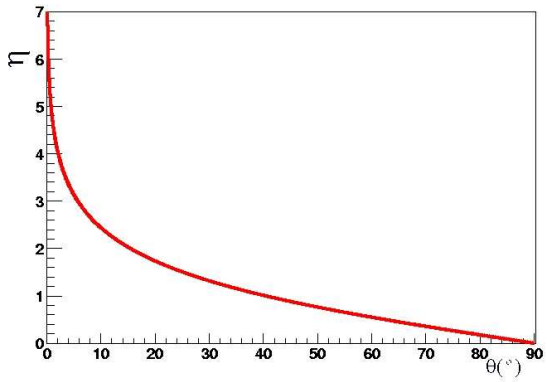

Figure D.2: Pseudorapidity η as a function of the angle θ (in degrees).

Acknowledgments

Quiero agradecer, en primer lugar, a todos los miembros del grupo su ayuda, colaboración y buen hacer. Gracias a todos ellos y a su esfuerzo hoy el ROD está funcionando sin problemas en el CERN y sin ellos no hubiese sido posible este trabajo.

En especial, quiero agradecer a mis tutores, Emilio y Juan, su apoyo constante desde el primer día hasta hoy y el haberme brindado la oportunidad de estar aquí, formando parte de un trabajo que tanto me gusta y permitirme poner mi granito de arena en este gran proyecto.

También quiero agradecer a Toni, quien me embarcó en lo que hoy es mi Trabajo de Investigación, el entusiasmo que siempre ha mostrado en este trabajo, sus ánimos y toda la confianza que depositó en mi desde el primer momento.

Ha sido muy importante para mi toda la colaboración con Sasha Solodkov, a quien estoy profundamente agradecida por guiarme paso a paso en Athena y todos los conocimientos que he adquirido a su lado. Agradecer a Belén todo lo que he aprendido junto a ella y todos los buenos momentos compartidos dentro y fuera de trabajo y a Luís toda la ayuda que he encontrado siempre en él. También quiero expresar aquí mi gratitud por toda la ayuda recibida a Giulio Usai, James Catmore y Maria Smizanska.

También agradecer a mis amigos y compañeros Paco, Carlos, Jose, Neus, Marta, Merche, Loli, Marian, Mª Jose y Rosana todos los buenos momentos que hemos pasado juntos, haciendo los malos días mucho más llevaderos y todas las veces que me han demostrado que puedo contar con ellos.

Aprovecho aquí para agradecer a mis padres todo el apoyo, cariño y fuerza que me han dado siempre y a mis hermanos, Rocío y Rafa, de los que estoy muy orgullosa. A todos ellos va dedicada esta tesina.

Por último pero no menos importante, quiero agradecer a Ximo su apoyo incondicional y constante, que me ha empujado tantas veces a seguir adelante (anem) y hacia quien siento una inmensa admiración y respeto.

Bibliography

[1] ATLAS Collaboration. *ATLAS detector and physics performance: Technical Design Report*, volume 2. 1999. CERN-LHCC-99-015.

[2] CKMfitter Group (J. Charles *et al.*). CP Violation and the CKM Matrix: Assessing the Impact of the Asymmetric B Factories. 2005. Eur. Phys. J. C41, 1-131.

[3] The LHC Study Group. *The Large Hadron Collider*. 1995. CERN/AC/95-05 (LHC).

[4] ATLAS Collaboration. *ATLAS Inner Detector: Technical Design Report*, volume 1. 1997. CERN-LHCC-97-016.

[5] ATLAS Collaboration. *ATLAS Calorimeter Performance: Technical Design Report*. 1996. CERN-LHCC-96-040.

[6] ATLAS Collaboration. *ATLAS Liquid Argon Calorimeter: Technical Design Report*. 1996. CERN-LHCC-96-041.

[7] ATLAS Collaboration. *ATLAS Tile Calorimeter: Technical Design Report*. 1996. CERN-LHCC-96-042.

[8] ATLAS Collaboration. *ATLAS Muon Spectrometer: Technical Design Report*. 1997. CERN-LHCC-97-022.

[9] ATLAS Collaboration. *ATLAS Magnet System: Technical Design Report, 1*. 1997. CERN-LHCC-97-018.

[10] ATLAS Collaboration. *ATLAS Level-1 Trigger: Technical Design Report*. 1998. CERN-LHCC-98-014.

[11] *VP 110/01x - 933 MHz or 800 MHz Intel Pentium III Processor - Low Power based VME board*. `http://www.gocct.com/sheets/pdf/vme/vp11001x_0305.pdf`.

[12] J. Castelo *et al.* TileCal ROD Hardware and Software Requirements. 2005. ATLAS Internal Note ATL-TILECAL-2005-003.

[13] P. Matricon. A 9U Transition Module for the ROD Demonstrator. 2004. ATLAS EDMS document ATL-AL-EN-0053.

[14] A. Ruiz and E. van der Bij. HOLA High-speed Optical Link for ATLAS. 2002. ATLAS EDMS document 330901.

[15] P. Matricon. The Trigger and Busy Module of the ATLAS LARG ROD System. 2004. ATLAS EDMS document ATL-AL-EN-0054.

[16] V. González *et al.* Data acquisition in TileCal/ATLAS experiment. Design of the Optical Multiplexer Board Prototype. IEEE Nuclear Science Symposium Conference Record, November 2005.

[17] D. La Marra. OC (Output Controller) FPGA of the LArgRod board Description. 2004. ATLAS EDMS document ATL-AL-EN-0056.

[18] A. Blondel, D. La Marra, A. Léger, I. Riu, and A. Straessner. VME and BUSY FPGA for the ROD motherboard. 2003. ATLAS EDMS document ATL-AL-EN-0060.

[19] B. Laforge and G. Perrot. TTC System Implementation for ATLAS Liquid Argon Detectors (V.2.2.2). April 2004. ATL-ELEC-2004-003.

[20] J. Christiansen, A. Marchioro, P. Moreira, and T. Toifl. *TTCrx Reference Manual*, 2003. `http://ttc.web.cern.ch/TTC/TTCrx_manual3.8.pdf`.

[21] J. Prast. The ATLAS Liquid Argon Calorimeters Read Out Driver (ROD). The TMS320C6414 DSP Mezzanine board. 2005. ATLAS EDMS document ATL-AL-CD-0009.

[22] *TMS320C6414, TMS320C6415, TMS320C6416 Fixed-Point Digital Signal Processors (Rev. N)*. 2005. Texas Instruments Datasheet.

[23] E. Fullana *et al.* Optimal Filtering in the ATLAS Hadronic Tile Calorimeter. 2005. ATLAS Internal Note ATL-TILECAL-2005-001.

[24] Particle Data Group. Particle physics booklet, July 2004.

[25] A. Dotti. Studio di un algoritmo per l'identificazione di muoni a basso impulso trasverso usando il calorimetro adronico dell'esperimento ATLAS ad LHC. Master's thesis, Università degli Studi di Pisa, 2002.

[26] G. Usai. Feasibility study of a level two low p_{T} di-muon trigger based on Tile Calorimeter. January 2003. ATL-DAQ-2003-017.

[27] G. Usai. *Identification and triggering of soft muons in the Atlas detector*. PhD thesis, Università degli Studi di Pisa, June 2004.

[28] G. Usai. Trigger of a low p_{T} muons with the ATLAS hadronic calorimeter. 2004. Nuclear Instruments and Methods in Physics Research.

[29] C. Bee *et al.* The raw event format in the ATLAS Trigger DAQ. 2005. ATLAS EDMS document ATL-D-ES-0019.

[30] G. Usai. Soft muon tagging with Tile & calorimeter muon isolation: Prospects for the HLT. Talk at the Muon HLT Review Meeting (CERN), July 2006.

[31] R. Brun, F. Rademakers, P. Canal, I. Antcheva, and D. Buskulic. *ROOT. User's Guide 5.12*, July 2006.

[32] J. Poveda *et al.* Production and Commissioning Performance Tests of the Read-Out Driver Boards for the Hadronic Tile Calorimeter of the ATLAS Detector at the LHC. IEEE Nuclear Science Symposium Conference Record, November 2005.

[33] M. Boonekamp *et al.* Cosmic Ray, Beam-Halo and Beam-Gas Rate Studies for ATLAS Commissioning. February 2004. ATL-GEN-2004-001.

[34] P. Farthouat and P. Gällnö. TTC-VMEbus INTERFACE TTCvi-MkII. 2002. ATLAS EDMS document 110746.

[35] E. van der Bij, W. Iwanski, and M. Joos. FILAR. Quad HOLA S-LINK to 64-bit/66 MHz PCI Interface. Users Guide. 2005. ATLAS EDMS document ATL-DQ-ES-0067.

[36] ROBIN Production Readiness Review: Design Document. 2005. ATLAS EDMS document ATL-DQ-ES-0067.

[37] *Athena. The ATLAS Common Framework. Developer Guide*, February 2004.

[38] C. Arnault. *CMT. Configuration Management Tool*, 2005. `http://www.cmtsite.org/CMTDoc.pdf`.

[39] A. Sidoti *et al.* The ATLAS Trigger Muon "Vertical Slice". Tata Institute of Fundamental Research, 2006.